Satellite-derived NO_x emissions over East Asia

Ding, Jieying

DOI
10.4233/uuid:3d0d456d-c6a9-4781-9a18-6cb041a4fd03

Publication date
2018

Document Version
Final published version

Citation (APA)
Ding, J. (2018). *Satellite-derived NO$_x$ emissions over East Asia*. [Dissertation (TU Delft), Delft University of Technology]. https://doi.org/10.4233/uuid:3d0d456d-c6a9-4781-9a18-6cb041a4fd03

Satellite-derived NO_x emissions over East Asia

Satellite-derived NO_x emissions over East Asia

Proefschrift

ter verkrijging van de graad van doctor
aan de Technische Universiteit Delft,
op gezag van de Rector Magnificus Prof. dr. ir. T. H. J. J. van der Hagen,
voorzitter van het College voor Promoties,
in het openbaar te verdedigen op vrijdag 26 januari 2018 om 15:00 uur

door

Jieying DING

Master of Science in Earth and Environment
Universiteit Wageningen, Nederland
geboren in Nanjing, China.

This dissertation has been approved by the

promotor: Prof. dr. P. F. Levelt
copromotor: Prof. dr. R. J. van der A

Composition of the doctoral committee:

Rector Magnificus,	chairperson
Prof. dr. P. F. Levelt,	promotor
Prof. dr. R. J. van der A,	copromotor

Independent members:

Prof. dr. ir. R. F. Hanssen,	Delft University of Technology
Prof. dr. ir. H. W. J. Russchenberg,	Delft University of Technology
Prof. dr. ir. G. Janssens-Maenhout,	Ghent University, Belgium
Prof. dr. G. de Leeuw,	Finnish Meteorological Institute, Finland
Dr. T. Stavrakou,	Royal Belgian Institute for Space Aeronomy

Keywords: NO_x emissions, satellite observations, East Asia

Printed by: Ipskamp Printing, The Netherlands

ISBN: 978-94-6366-006-8
NUR: 956

An electronic version of this dissertation is available at
http://repository.tudelft.nl/.

Life is limited and knowledge is infinite.
Do not chase after infinite knowledge in your limited life.

Zhuangzi (369 – 286 BC)

吾生也有涯，而知也无涯。以有涯随无涯，殆已!

庄子

Contents

Summary **xi**

Samenvatting **xv**

1 Introduction **1**
1.1 Atmospheric constitution and structure 1
1.2 Air pollution 3
1.2.1 Nitrogen oxides (NO_x) 3
1.2.2 The role of NO_x in the troposphere 4
1.3 The impact of NO_x on environment and human health 6
1.4 High emissions in East Asia 7
1.5 NO_x emissions estimated with the bottom-up approach 10
1.6 NO_x emission estimates from satellite measurements 13
1.6.1 Satellite observations 13
1.7 Emission estimates from space 15
1.7.1 DECSO 17
1.8 Research objectives and thesis overview 19

2 NO_x emissions estimates during the 2014 Youth Olympic Games in Nanjing **23**
2.1 Introduction 25
2.2 Methods 28
2.2.1 Emission estimates 28
2.2.2 Satellite observations 30
2.2.3 Ground-based observations 32
2.3 Improvements of DECSO 32
2.3.1 Model improvement 32
2.3.2 Quality control of satellite data 35
2.4 Emission analysis for the Nanjing Youth Olympic Games 38
2.5 Discussion and conclusions 44

3 Space-based NO_x emission estimates over remote regions improved in DECSO **47**
3.1 Introduction 48
3.2 Emission estimates with the DECSO algorithm 50

3.3 Improvement of DECSO 52
3.3.1 Observation and representativeness error calculation . . 52
3.3.2 Emission update constraint 54
3.3.3 Logarithm of emission 57
3.3.4 The threshold of the sensitivity matrix and the effect of biogenic NO_x emissions 58
3.4 Results 60
3.4.1 Seasonal cycle analysis 60
3.4.2 Ship track emissions near the Chinese coast 63
3.5 Discussions and conclusions 65

4 Maritime NO_x emissions over Chinese seas derived from satellite observations 71
4.1 Introduction 72
4.2 Emission estimates 73
4.3 Results 74
4.3.1 Seasonal cycle 75
4.3.2 Trend analysis 75
4.3.3 Contribution of shipping emissions to NO_2 air pollution 77
4.4 Discussion 78
4.5 Conclusions 80

5 Intercomparison of NO_x emission inventories over East Asia 83
5.1 Introduction 85
5.2 Emission inventories 88
5.2.1 Bottom-up inventories 88
5.2.2 Satellite-derived inventories 90
5.3 Intercomparison of NO_x emissions 93
5.3.1 Temporal evaluation 93
5.3.2 Spatial distribution 98
5.4 Discussion 103
5.4.1 Temporal analyses 103
5.4.2 Spatial analyses 104
5.4.3 Differences in the bottom-up emissions 104
5.4.4 Differences in the satellite-derived emissions 105
5.5 Conclusions and recommendations 107

6 Conclusions and outlook 109
6.1 The sensitivity of DECSO on the CTM and satellite observations 110
6.2 Improvements in the application of the extended Kalman filter in DECSO 111

6.3 Application of improved DECSO: long record of maritime emissions 113
6.4 Validation of emission estimates from satellite observations . . 114
6.5 Outlook 115

Appendix **117**

References **119**

Acknowledgements **138**

Curriculum Vitæ **141**

List of Publications **145**

Summary

Nitrogen oxides (NO + NO_2 = NO_x) are important air pollutants and play a crucial role in climate change by catalysing the formation of tropospheric ozone and forming secondary nitrate aerosols. NO_x emissions are important for chemical transport models (CTMs) to simulate and forecast air quality. Emission information also helps policymakers to mitigate air pollution. In this thesis, we have focused on providing better NO_x emission estimates with the DECSO (Daily Emission estimates Constrained by Satellite Observations) inversion algorithm applied to satellite observations. In DECSO, simulations of NO_2 concentration from a CTM have been combined with satellite observations to give the 'best' estimate of emissions based on an extended Kalman filter. We used satellite observations from OMI and GOME-2, which have a high spatial resolution (up to 24 km $\times$ 13 km) and global coverage on a daily basis.

To improve the DECSO algorithm able to better detect NO_x emissions on a small spatial scale and from weak sources over remote areas, we have further developed the DECSO algorithm focusing on three aspects: using a better chemical transport model, setting a quality control for satellite observations, and the treatment of error covariances in the Kalman filter. The improvements of DECSO have been verified by two case studies: (1) emission changes during the Nanjing Youth Olympic Games event and (2) detection of shipping emissions. A comprehensive intercomparison of nine NO_x emission inventories over East Asia has been studied to validate the NO_x emissions estimated from satellite observations.

In Chapter two, we replaced the outdated CHIMERE 2006 model with the new version CHIMERE v2013 in DECSO. An OmF (Observation minus Forecast) criterion has been added to filter out outlying observations due to high aerosol concentrations. With these improvements, DECSO was updated to DECSO version 3b (DECSO v3b). The Nanjing Youth Olympic Games (YOG) event has been selected as a case study to demonstrate the improvements since the local government enforced very strict air quality regulations during this event. Satellite observations from OMI showed a decrease of 32 % of the NO_2 column concentrations during the YOG event as compared to the averaged value over the last ten years. The results of DECSO v3b showed that NO_x emissions decreased by at least 25 % during the YOG event. The algorithm also detected an emission reduction of 10 % during the Chinese Spring Festival. This study demonstrated the capacity of the DECSO algorithm to capture changes in NO_x emissions on a monthly scale.

We have further developed DECSO v3b to DECSO v5 by improving the application of the Kalman filter to better detect low NO_x emissions over remote areas. We improved the characterisation of the error covariance of the sensitivity of NO_2 column observations to gridded NO_x emissions. The resulting background noise of emission estimates has been decreased by a factor of 10. We also added an emission update constraint to replace the OmF filter criterion. This improvement avoids unrealistic day-to-day fluctuation of emissions and increases the emission update speed by using more satellite observations. We calculated the NO_x emission over East Asia with DECSO v5 for a period of 10 years. We showed the importance of biogenic emissions, which drive the seasonal cycle of NO_x emissions, especially over rural areas. In addition, the improved algorithm is able to better capture the seasonality of NO_x emissions and for the first time it reveals ship tracks near the Chinese coasts that are otherwise hidden by the outflow of NO_2 from the Chinese mainland. The precision of monthly emissions derived by DECSO v5 for each grid cell is about 20 %. The emissions derived by DECSO v5 are in good agreement with other inventories like MIX.

We have presented maritime NO_x emissions derived with DECSO v5 applied to OMI observations over Chinese coast areas in Chapter 4. It is the first time that the monthly NO_x emissions derived from satellite observations over Chinese seas have been shown for a 10-year period (2007 to 2016). The trend analysis showed that the maritime emissions have a continuous increase rate of about 20 % per year until 2012 and slow down to about 3 % per year afterwards. This reflects that no effective regulations on NO_x emissions have been implemented for ships in China. The seasonal cycle of maritime emissions has regional variations but all regions show lower emissions during winter. The satellite-derived spatial distribution and the magnitude of maritime emissions over Chinese seas are in good agreement with bottom-up studies based on the Automatic Identification System of ships.

We tried to validate NO_x emission estimates over East Asia in chapter 5 by comparing nine emission inventories of NO_x including four satellite-derived NO_x inventories and the following bottom-up inventories for East Asia: REAS (Regional Emission inventory in ASia), MEIC (Multi- resolution Emission Inventory for China), CAPSS (Clean Air Policy Support System) and EDGAR (Emissions Database for Global Atmospheric Research). Two of the satellite-derived inventories were estimated by using the DECSO v5 applied to observations from OMI or from GOME-2. The other two were derived with the EnKF algorithm, which is based on an ensemble Kalman filter applied to observations of multiple species using either the chemical transport model CHASER or MIROC-chem. The intercomparison showed good agreement in total NO_x emissions over mainland China with an average bias of about 20 % for yearly emissions. All the inventories show the typical emission reduction of 10 % during the Chinese Spring Festival and a peak in December. Biases in NO_x emis-

sions and uncertainties in temporal variability become larger when the spatial scale decreases. Satellite-derived approaches using OMI show a summer peak due to strong emissions from soil and biomass burning in this season. Using observations from multiple instruments is recommended for the satellite-derived approach.

The work presented in this thesis showed that NO_x emissions derived from satellite observations can be of the same quality as bottom-up inventories. However, the emissions are available soon after observation and the temporal variability of NO_x emissions is better derived from the satellite approach. We only applied DECSO over East Asia in the thesis. In the future, we will apply DECSO v5 to other regions, for example, Europe, India, and the Middle East. Satellite-derived NO_x emissions can be further improved when better satellite observations with higher temporal (hourly observations) and spatial resolution (7 km $\times$ 3.5 km) become available.

Samenvatting

Stikstofoxiden (NO + NO_2 = NO_x) zijn belangrijke luchtverontreinigende stoffen en spelen een cruciale rol in klimaatverandering door de vorming van secundaire nitraat-aërosolen en door als katalysator op te treden bij de vorming van troposferisch ozon. Gegevens over de uitstoot van NO_x zijn belangrijk voor chemische transportmodellen (CTMs) om de luchtkwaliteit te simuleren en te voorspellen. Informatie over de uitstoot helpt ook beleidsmakers om luchtvervuiling in te perken. In dit proefschrift richten we ons op het bepalen van betere schattingen van de uitstoot van NO_x met het inversiealgoritme DECSO (Daily Emission estimates Constrained by Satellite Observations) toegepast op satellietwaarnemingen. In DECSO zijn simulaties van een CTM voor NO_2-concentraties gecombineerd met satellietwaarnemingen om de 'beste' schatting van de uitstoot te bepalen met behulp van een extended Kalman filter. We gebruiken satellietwaarnemingen van OMI en GOME-2, die dagelijks metingen met een hoge ruimtelijke resolutie (tot aan 24 km $\times$ 13 km) en wereldwijde dekking verrichten.

Om met het DECSO-algoritme beter de uitstoot van NO_x te detecteren op een kleine ruimtelijke schaal en van zwakke bronnen in afgelegen gebieden, hebben we het DECSO-algoritme verder ontwikkeld door ons op drie aspecten te richten: het gebruik van een beter chemisch transportmodel, het instellen van een kwaliteitscontrole op satellietobservaties, en de behandeling van fouten covarianties in het Kalman-filter. De verbeteringen van DECSO zijn geverifieerd door twee casestudies: (1) de reductie van de uitstoot van NO_x tijdens de Olympische Jeugdspelen in Nanjing en (2) de detectie van de uitstoot door scheepvaart. Een uitgebreide vergelijking van negen NO_x inventarisaties voor Oost-Azië is uitgevoerd om de NO_x uitstoot bepaald uit satellietmetingen te valideren.

In hoofdstuk twee vervingen we in DECSO het verouderde model CHIMERE 2006 door de nieuwe versie CHIMERE v2013. Een OmF (Observatie minus Forecast) criterium is toegevoegd om observaties weg te filteren die sterk afwijken door hoge aerosolconcentraties. Met deze verbeteringen is het algoritme verbeterd tot DECSO versie 3b (DECSO v3b). De Nanjing Olympische Jeugdspelen zijn geselecteerd als case studie om de verbeteringen te demonstreren, aangezien tijdens deze spelen zeer strenge luchtkwaliteitsvoorschriften zijn ingevoerd door de lokale overheid. Satellietwaarnemingen van OMI toonden een daling aan van 32 % van de NO_2 kolomconcentraties tijdens de Olympische periode in vergelijking met de gemiddelde waarde over de afgelopen tien jaar. De resultaten van DECSO v3b tonen aan dat

de NO_x uitstoot tijdens de Olympische Jeugdspelen met tenminste 25 % gedaald is. Het algoritme detecteerde ook een reductie van 10 % in uitstoot tijdens het Chinese Lente Festival. Deze studie demonstreert de mogelijkheid van het DECSO-algoritme om veranderingen in de NO_x uitstoot op een tijdschaal van maanden te registreren.

We hebben DECSO v3b verder ontwikkeld tot DECSO v5 door de toepassing van het Kalman filter te verbeteren om de NO_x-uitstoot in afgelegen gebieden beter te kunnen detecteren. We hebben de karakterisering verbeterd van de fouten covariantie matrix van de gevoeligheid van NO_2 kolomwaarnemingen voor de NO_x uitstoot per grid cel. De resulterende achtergrondruis in de uitstootschattingen is hierdoor met een factor 10 gedaald. We hebben ook een beperking in de grootte van de aanpassing van de uitstoot getallen ingevoerd om het OmF-filtercriterium te vervangen. Deze verbetering voorkomt onrealistische fluctuaties in de bepaalde dagelijkse uitstoot en verhoogt de snelheid waarmee de uitstoot getallen worden bijgewerkt doordat er meer satellietwaarnemingen gebruikt worden. We hebben de NO_x-uitstoot in Oost-Azië berekend met DECSO v5 voor een periode van 10 jaar. We hebben het belang van biogene uitstoot aangetoond, die de seizoensgang van de NO_x-uitstoot bepalen, vooral in landelijke gebieden. Daarnaast is het verbeterde algoritme beter in staat om de seizoensgang van de NO_x-uitstoot vast te leggen én voor de eerste keer zijn schipvaartroutes langs de Chinese kust aangetoond die normaal gesproken onder de weggewaaide NO_2 van het Chinese vasteland verborgen blijven. De precisie waarmee de maandelijkse uitstoot in elke grid cel bepaald is door DECSO v5 is ongeveer 20 %. De uitstoot afgeleid door DECSO v5 komt goed overeen met andere inventarisaties zoals MIX.

In hoofdstuk 4 hebben we de uitstoot van maritieme NO_x afgeleid met DECSO v5 toegepast op de OMI observaties boven Chinese kustgebieden. Het is de eerste keer dat de maandelijkse NO_x-uitstoot voor een periode van 10 jaar (2007 tot 2016) is bepaald op basis van satellietmetingen boven de Chinese zeeën. De trendanalyse laat zien dat de maritieme uitstoot blijft stijgen tot en met 2012 met een continue toename van ongeveer 20 % per jaar en daarna vertraagt tot een toename van ongeveer 3 % per jaar. Dit weerspiegelt het feit dat er geen effectieve voorschriften ingevoerd zijn voor de uitstoot van NO_x voor de scheepvaart in China. De seizoensgang in de uitstoot van de scheepvaart heeft regionale variaties, maar alle regio's vertonen een verminderde uitstoot in de winter. De met de satelliet afgeleide ruimtelijke verdeling en omvang van de maritieme uitstoot in de Chinese wateren komen goed overeen met bottom-up studies die gebruik maken van het Automatische Identificatie Systeem van schepen.

We hebben geprobeerd de NO_x-uitstootschattingen voor Oost-Azië in hoofdstuk 5 te valideren door de vergelijking van negen uitstoot-inventarisaties van NO_x, waarvan vier inventarisaties afgeleid van satellietwaarnemingen en de volgende vijf bottom-up-inventarisaties voor Oost-Azië: REAS (Regional Emission inventory in

ASia), MEIC (Multi-resolution Emission Inventory for China), CAPSS (Clean Air Policy Support System) en EDGAR (Emissions Database for Global Atmospheric Research). Twee van de met satellietwaarnemingen afgeleide inventarisaties zijn bepaald met DECSO v5 toegepast op waarnemingen van óf OMI óf GOME-2. De andere twee zijn bepaald met het EnKF-algoritme, dat is gebaseerd op een ensemble Kalman filter toegepast op waarnemingen van verschillende sporengassen met behulp van óf het chemische transportmodel CHASER óf MIROC-chem. De vergelijking toont een goede overeenkomst aan in alle afgeleide totale NO_x-uitstoot over het vasteland van China met een gemiddelde bias van ongeveer 20 % in de jaarlijkse uitstoot. Alle inventarisaties tonen een typische reductie in uitstoot van 10 % aan tijdens het Chinese Lente Festival en verder een piek in december. De bias in NO_x-uitstoot en de onzekerheden in de variabiliteit in tijd worden groter naarmate de ruimtelijke schaal afneemt. De op OMI waarnemingen gebaseerde uitstoot vertoont een zomer piek door de sterke uitstoot uit de bodem en van biomassaverbranding in dit seizoen. Het gebruik maken van observaties van verschillende instrumenten wordt aanbevolen voor de op satellieten gebaseerde aanpak.

Het werk dat in dit proefschrift is gepresenteerd, laat zien dat NO_x-uitstoot afgeleid van satellietwaarnemingen van dezelfde kwaliteit is als van bottom-up inventarisaties. De getallen gebaseerd op satellietwaarnemingen zijn echter snel beschikbaar en de temporele variabiliteit van de NO_x-uitstoot is beter te bepalen met deze satellietmetingen. We hebben echter in dit proefschrift DECSO alleen op Oost-Azië toegepast. In de toekomst zullen we DECSO v5 ook toepassen in andere regio's, bijvoorbeeld Europa, India en het Midden-Oosten. De uitstoot van NO_x met behulp van satellietwaarnemingen kunnen nog verder worden verbeterd wanneer observaties met een hogere tijds- (uurlijks) en ruimtelijke (7 km $\times$ 3.5 km) resolutie beschikbaar komen.

1

Introduction

1.1. Atmospheric constitution and structure

The Earth's atmosphere is crucial for all living organisms on Earth. It is a thin layer consisting of different gases covering the Earth. The state of and small changes in the Earth's atmosphere affect activities and survival of life. The main ingredients of the atmosphere are nitrogen (N_2, 78 %), oxygen (O_2, 21 %), and argon (Ar, 0.9 %) (see Figure 1.1). Water vapour is also one of the main constituents of the atmosphere but with a variable concentration, which can range from 0 to 4 %. The small remaining part of the atmosphere is mainly composed of carbon dioxide (CO_2), neon (Ne), helium (He), ozone (O_3), etc., which are known as trace gases. All these gases are gathered around the Earth's surface captured by the Earth's gravity. They are approximately in hydrostatic equilibrium. Following the barometric law, the pressure of the atmosphere decreases exponentially with altitude. The pressure at sea level is normally about 1013 hPa and decreases to about 0.01 hPa at the height of 80 km, below which 99.999 % of the atmospheric mass resides.

The atmosphere is vertically classified in four main layers, which are troposphere, stratosphere, mesosphere, and thermosphere. The classification of vertical layers is based on the change in the vertical temperature gradient (See Figure 1.2). The lowest layer is the troposphere, where weather phenomena occur and temperature decreases as altitude increases. Studies of air pollution generally focus on the troposphere. The troposphere itself consists of two parts: the planetary boundary layer (PBL) and the free troposphere. The PBL directly interacts with the Earth's

1

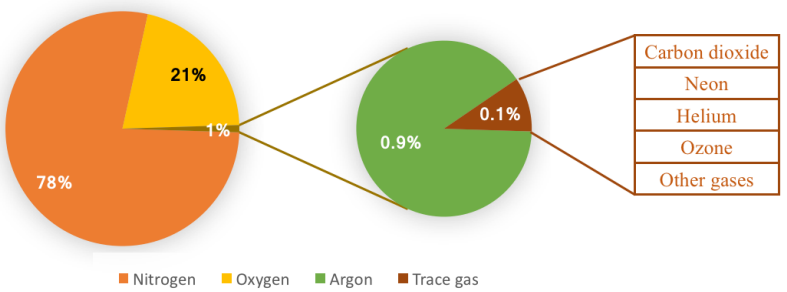

Figure 1.1: Atmospheric composition of dry air.

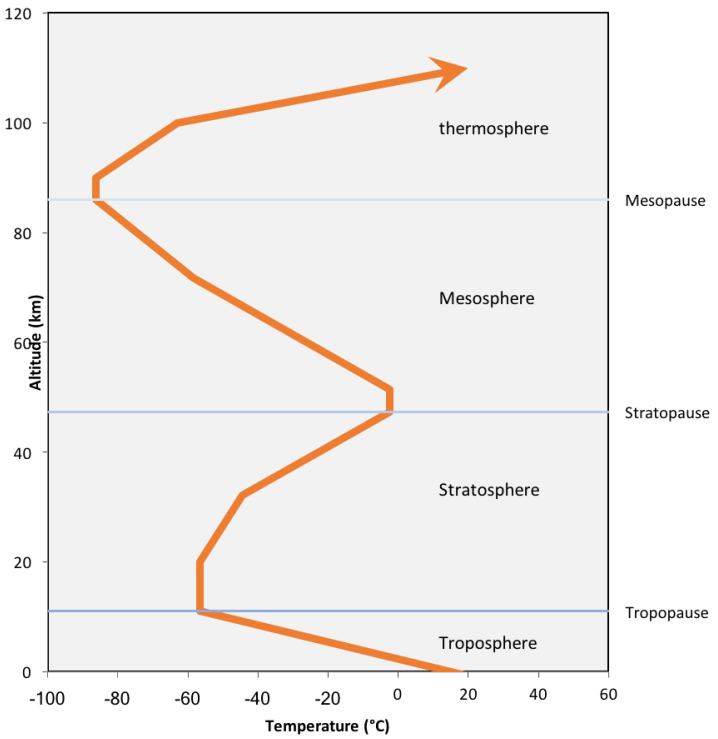

Figure 1.2: Vertical structure of atmosphere with the temperature profile.

surface through exchanges of e.g. heat, moisture, momentum, and air pollutants between troposphere and surface. The PBL height ranges from 100 to 3000 m, and depends on the thermal convection and wind shear. On top of the PBL is an inversion layer, which is called the entrainment zone, where exchange and mixing

of air pollutants from the PBL to the free troposphere take place. The tropopause is the transition layer between the troposphere and stratosphere. The typical height of the tropopause is about 5 to 18 km, depending on latitude and season. The main feature of the tropopause is the rapid change of the temperature gradient with height. In the stratosphere, the temperature gradient is opposite to that in the troposphere. The temperature increases with height because of the absorption of solar ultraviolet radiation by O_3. The stratosphere ends in the stratopause at about 50 km. Above the stratopause lies the mesosphere, which extends from 50 to 85 km. The temperature in the mesosphere decreases with height. Above the mesosphere is the thermosphere, where the air is directly heated by absorption of X-ray and ultraviolet (UV) radiation of the sun.

1.2. Air pollution

1.2.1. Nitrogen oxides (NO_x)

Since the famous smog episode in Los Angeles in the early 1950s, scientists have identified the chemical reactions involving sunlight, nitrogen oxides (NO_x=NO+NO_2) and hydrocarbons as the basic mechanism for photochemical smog. This attracted attention to the role of NO_x in the troposphere.

NO_x is emitted by both natural and anthropogenic sources. The global total NO_x emissions are about 50 Tg N yr^{-1} and have been nearly constant during the last two decades but the trends of NO_x emissions by regions are quite diverse (Miyazaki et al., 2017). In nature, NO_x can be produced via lightning flashes due to their high temperature. The mechanism in the formation of NO_x under conditions of high temperatures will be introduced in Chapter 1.2.2. The global lightning emissions are about 5 to 7 Tg N yr^{-1} (Miyazaki et al., 2014; Finney et al., 2016).

Another natural source of NO_x is soil. NO is the predominant form of soil NO_x emissions. It comes from both abiotic and biotic processes. The abiotic process is called chemo-denitrification, when NO_x is emitted especially in acid soil with high organic matter content. Biological processes of nitrification and denitrification are the main reason of soil NO_x emissions, which can be affected by concentrations of ammonia and nitrate radicals in soil, soil moisture, temperature and soil properties. Thus, human activities such as changes of land use or use of nitrogen fertiliser (Akiyama et al., 2000) affect these NO emissions. The global soil NO_x emissions are estimated to be about 13 Tg N yr^{-1} (Vinken et al., 2014).

Biomass burning is the burning of living and dead vegetation either naturally or

caused by human activities. Burning vegetation causes a surge of smoke, which is a complex mixture of many particulates and gases including NO_x. Natural biomass burning can be caused by for example lightning strikes. Man-made fires, such as burning of agricultural waste, grassland or forest, are usually associated with land clearance and land use change for agricultural purposes. Global NO_x emissions from biomass burning are about 5 to 8 Tg N yr^{-1} (Jain et al., 2006; Lamarque et al., 2010).

However, the main contribution to NO_x emissions is from anthropogenic sources, especially in urban areas. Combustion processes in several source type categories, like industry, thermal power plants, transport and domestic, are the major contributors to NO_x emissions. Especially energy-intensive processes in petrochemical, cement, iron and steel industries are among the highest anthropogenic emitters. High temperatures in combustion engines causes a relatively high amount of NO_x emitted by traffic. That is why urban areas usually show high NO_2 concentrations. In the traffic source sector also shipping plays an important role, since ship emissions are responsible for more than 10 % of the total NO_x budget. Using fossil fuels, such as coals, which contain nitrogen, lead to additional NO_x emissions via the oxidation of nitrogen in the fuel during combustion. Global anthropogenic emissions of NO_x are about 30 Tg N yr^{-1} (Granier et al., 2011). Table 1.1 summarizes the major sources and their ranges of emissions.

Table 1.1: Overview of global NO_x emission sources.

Source type	Emissions (Tg N yr^{-1})
Soil	4 - 15
Biomass burning	5 - 8
Lightning	5 - 7
Anthropogenic	26 - 34

1.2.2. The role of NO_x in the troposphere

NO_x is usually emitted as NO during lightning or in combustion processes when the temperature is above 2000 K, which is high enough to break down O_2 molecules. Atomic oxygen is produced and reacts with N_2 to generate NO. This process involves the following three equilibrium equations:

$$O_2 \leftrightarrow O + O \tag{R1}$$

$$O + N_2 \leftrightarrow NO + N \tag{R2}$$

$$N + O_2 \leftrightarrow NO + O \tag{R3}$$

The formation of NO during combustion is affected by three factors: O_2 concentration, peak temperature and time of exposure at peak temperature. NO emissions increase with increases in any of these three factors. After the production of NO, NO_x follows a rapid cycle between NO and NO_2:

$$NO + O_3 \rightarrow NO_2 + O_2 \tag{R4}$$

$$NO_2 + h\nu \overset{O_2}{\rightarrow} NO + O_3 \tag{R5}$$

Since ambient NO_2 needs sunlight to transform into NO, the concentration of NO_2 normally has a strong diurnal cycle. Note that in the NO-NO_2 cycle no net O_3 is produced, but with the existence of HO_2 or organic peroxy radical (RO_2) NO has alternative ways to transform into NO_2:

$$NO + HO_2 \rightarrow NO_2 + OH \tag{R6}$$

$$RO_2 + NO \rightarrow NO_2 + RO \tag{R7}$$

This reaction breaks the balance of the NO-NO_2 cycle and will generate O_3 via (R5). The main formation of HO_2 in Equation (R6) is due to the oxidation of CO and volatile organic compounds (VOCs).

The removal of NO_x from the atmosphere is via the oxidation with OH to nitric acid ($HONO_2$, or HNO_3), which is considered to be the main sink of NO_x during daytime. At night, NO_2 reacts with O_3 forming N_2O_5. NO_x sinks also include the formation of nitrates by reacting with sulphate aerosols or volatile organic compounds. These reservoir species of NO_x can be removed from the atmosphere via dry and wet deposition. NO_x has a short lifetime, which varies from a few hours in the tropics to about several days at midlatitudes in winter. The lifetime of NO_x depends on many factors, such as meteorological conditions, photolysis timescale,

and OH concentrations. However, long-range transport of NO_x also occurs due to peroxyacetyl nitrates (PANs) as one of its reservoir species which has an atmospheric lifetime of longer than one month in the upper troposphere and releases NO_x during its decomposition.

1.3. The impact of NO_x on environment and human health

NO_x as well as its secondary pollutants, such as O_3 and nitrate particles, are regarded as major air pollutants. High NO_2 concentrations can be seen as a reddish-brown layer over urban areas, while nitrate particles can make air hazy and reduce the visibility (see Figure 1.3). NO_x itself and its secondary pollutants are also toxic and harmful for the environment. Various human body systems and organs are affected in both short- and long-term exposures of high concentrations of NO_x, ozone and PM, which can lead to respiratory and heart diseases, lung cancer and asthmatic attacks (Abbey et al., 1999; Kampa and Castanas, 2008).

When the NO_x reservoir gas HNO_3 is solved in water, this can lead to acid rain, which is harmful to plants, aquatic animals and cultural heritage. Acid rain directly damages the leaves of plants, and leads to reduced photosynthesis. It destroys the PH balance of soil, lakes and affects the connected ecosystems (Kampa and Castanas, 2008). Deposition of NO_x and nitrates can also cause eutrophication of lakes, rivers and bays since nitrogen is one of the main nutrients for plants. Excessive nitrogen in water causes overgrowth of plants and algae on the water surface and decrease of oxygen in the water. Consequently, this leads to serious problems of water quality and deterioration of aquatic ecological system.

NO_x emissions have a complicated impact on climate change since they have both warming and cooling effects. NO_x leads to the increase of tropospheric O_3, aerosol and OH radical. O_3 is a greenhouse gas causing positive radiance forcing and enhances the influence of CO_2 on global warming (Ramanathan et al., 1985). Tropospheric O_3 also makes a large contribution to global warming because of the significant suppression of the global land-carbon sinks due to reduced plant productivity (Sitch et al., 2007). The increase of aerosols and OH radicals on the other hand has a cooling effect. The increasing concentrations of OH reduce the lifetime of the greenhouse gas methane (CH_4), especially over ocean due to shipping emissions in a relatively clean marine environment (Corbett et al., 1999; Eyring et al., 2010). Shindell et al. (2009) showed that increased NO_x emissions enhance the global burdens of hydroxyl and sulphate and cause a net cooling effect by considering the

Figure 1.3: A reddish-brown layer above the temple of Heaven in Beijing. The photo was taken at 13:40 local time, 27 February 2017. The hourly NO_2 concentration was about 110 ug/m3 near the surface according to the local in-situ measurement of the Ministry of Environment Protection in China

influence of NO_x on both O_3 and aerosol.

1.4. High emissions in East Asia

In East Asia, the highest NO_2 concentrations have been observed during the last two decades (see Figure 1.4). With the help of satellite observations, it has been shown that the NO_2 concentration increased significantly in East Asia from 1996 to around 2011 (Irie et al., 2005; Richter et al., 2005; van der A et al., 2006; Liu et al., 2016; van der A et al., 2017). Emissions of air pollutants rapidly increased in this region, especially in China, due to the fast-increasing energy consumption caused by rapid industrial development and economic growth. NO_x emissions from China (43 %) and Japan (13 %) contributed to about 60 % of the total NO_x emissions in Asia. Without any air quality control measures, total NO_x emissions in Asia in 2020

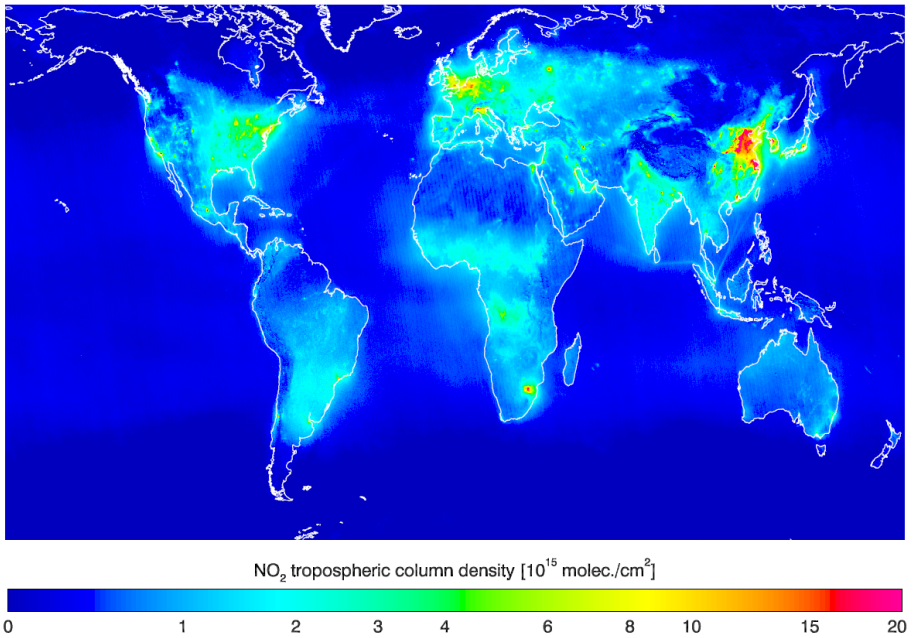

Figure 1.4: The average tropospheric NO_2 column concentration from 2005 to 2015 observed by the OMI satellite instrument.

would have increased with about 2000 % relative to 2005 (Bouarar et al., 2017).

Nevertheless, China is threatened by one of the worst air pollution problems in the world (Kan et al., 2012), as the largest developing country with strong economic expansion over the past two decades. 70 % of urban areas are highly polluted and their air quality is below the national ambient air quality standards. 75 % of urban residents are exposed to unhealthy air according to the data of the State Environment Protection Administration of 1995 to 2004 (Shao et al., 2006). In 2004, the annual mean of PM10 concentration was 121 μg m^{-3} in the cities nationwide (Kan et al., 2009), while the guideline for air quality suggested by the World Health Organization for annual PM10 concentrations is less than 50 μg m^{-3}. The statistical studies on diseases caused by ambient air pollution in China show that the Chinese residents, which are more than one fifth of the global population, have significant health risks due to ambient air pollution (Kan et al., 2012). High PM10 concentrations lead to a reduction of life expectancy of about 3 years in China (Ebenstein et al., 2017).

Air pollution draws more and more public attention in China due to the increasing number of days with very low visibility. On 1st Jan 2017, Jiangsu Province sent an

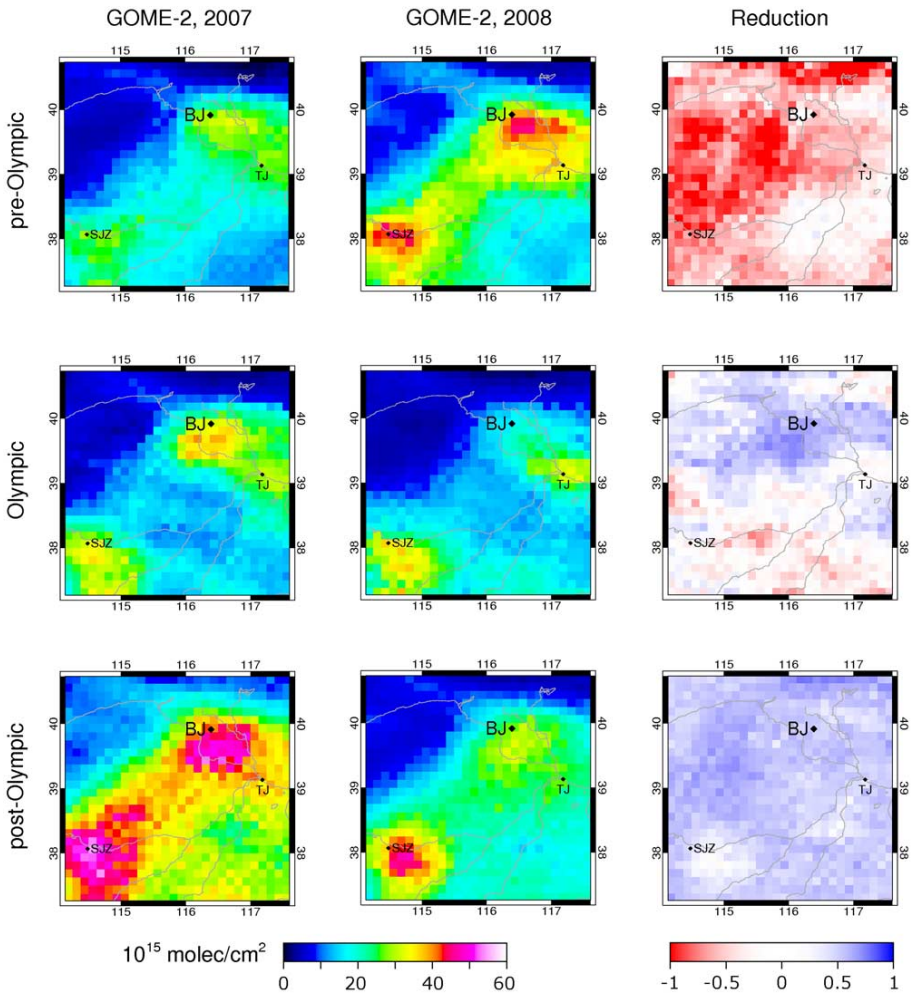

Figure 1.5: Tropospheric NO_2 columns observed by GOME-2 for a pre-Olympic, Olympic and post-Olympic period in 2007 (left) and 2008 (middle). In the Olympic period, the strongest (right) concentration reductions are found around Beijing. Concentration reductions are still present in the post-Olympic period (Mijling et al., 2009).

air pollution alert to the public since the visibility was less than 50 m. Apart from discussing the weather, nowadays people in China also care about concentrations of PM. When days are very hazy, people wear masks outside to protect themselves from the strong air pollution. Air quality forecasts are becoming as popular as weather forecast in China. The national and local authorities use these forecasts to decide when they should declare air pollution alerts and advise people to stay indoors.

In addition, due to the severe problems of air quality, all international events held in China have specific requirements on air quality that should meet the air quality standards of the World Health Organization. This obliges the local authorities to take some permanent and temporary air quality regulations to ensure good air quality during event periods, for example, the 2008 Olympic Games in Beijing, the 2010 World Expo in Shanghai, and the 2014 Youth Olympic Games in Nanjing. These events also give researchers great opportunities to study the effect and efficiency of different air quality regulations on reducing concentrations of air pollutants. Figure 1.5 shows an example of NO_2 reduction during the Beijing Olympic Games measured from GOME2.

1.5. NO_x emissions estimated with the bottom-up approach

To make correct strategies on air quality control, information on strength and location of pollutant emission sources is very important for policymakers. Emission inventories are also needed for better understanding in atmospheric research. They are crucial input to air quality models, which are used to assess our knowledge of atmospheric processes, to analyse historical air pollution events, different emission scenarios and trends, and to forecast air quality. The incorrect temporal allocation of precursor emissions can lead to very wrong predictions of air quality (Eder et al., 2009). NO_x emissions play a key role in simulating ozone in chemical transport models, especially over urban areas (Ma and van Aardenne, 2004).

An empirical way to estimate NO_x emissions is the so-called bottom-up approach. With this approach, emissions are calculated based on different source categories: anthropogenic and natural sources. For anthropogenic emissions, the main source categories are industry, power plants, transport, residential and agricultural. To calculate emissions from each source category, information is required of emission activity rate (such as fuel consumption or material production), emission factor (emissions per fuel unit), combustion technology and penetration of abatement control measures. This information will be referred to as emission calculation input data. Figure 1.6 shows the framework of emission calculations in the bottom-up approach.

For the sources with a fixed location, we take the NO_x emission estimates from power plants as an example. It needs input data of boiler type, coal, oil or gas consumption rate, emission factor, emission abatement technology type, heating value of coal, oil or gas used for each unit, unit capacity per power plant and

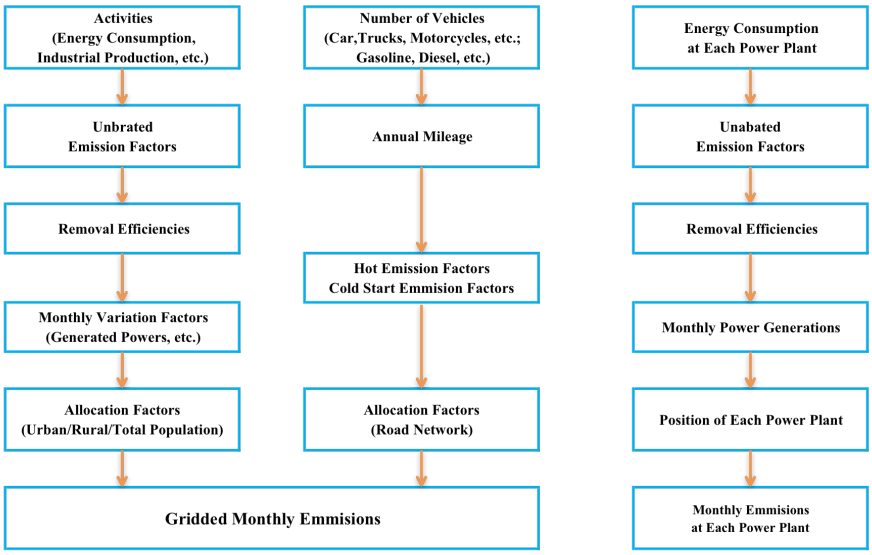

Figure 1.6: The framework of emission calculations in the bottom-up approach (adapted from Kurokawa et al., 2013).

operation time (Zhao et al., 2008; Q Zhang et al., 2009; Liu et al., 2015).

Transport is usually the main source of NO_x, which accounts for about 40 % of the global total NO_x emissions (Janssens-Maenhout et al., 2015). The calculation of emissions from transport is quite different compared to other sources, because emissions from the transport category are mobile and affected by vehicle stock, vehicle technology, emission factors, activity level and their spatial distribution. A method to estimate these emissions is using a road segment on the basis of activity data, such as traffic flow and vehicle types (Niemeier et al., 2004), which is difficult to achieve on a global scale due to limitations on data availability or accessibility. In Asia these data are difficult to obtain. In that case, an older method is used, which calculates emissions on a provincial or national level and allocates total emissions to grids or roads based on proxies such as gross domestic product, population density (Zheng et al., 2014).

Compiling a comprehensive bottom-up emission inventory over a large geographic region is quite challenging because of the numerous emission calculation input data for different cities, provinces and countries. One way to estimate emissions is to use a consistent framework in the calculation process with available resources. Many regional or global inventories are conducted in a unified way, for

example, the TRACE-P (Streets et al., 2003) and REAS (Ohara et al., 2007) emission inventory for Asia and the global inventory EDGAR V4.3.1 (Crippa et al., 2016). Nowadays the coverage of species, source categories, and time period are often not consistent in inventories including many countries. Emission data are usually available at different spatial and temporal resolutions. Since many local or regional inventories are state-of-art inventories using local information, which can be hardly available outside the region, a so-called 'mosaic' method has been applied to get better emission inventories. This mosaic method harmonizes several emission inventories of different countries or regions into a single emission inventory over a larger domain in a uniform format. The INTEX-B (Q Zhang et al., 2009) emission inventory over Asia is developed using the 'mosaic' method by combining improved emissions over China and the best available local emission inventories from Japan, Korea, Taiwan and India. MIX (Li et al., 2017) is the latest available Asian emission inventory, which combines 6 different national and regional emission inventories for the year 2008 and 2010 with a horizontal resolution of $0.25^\circ \times 0.25^\circ$. The recent comprehensive global inventory HTAP_v2 (Janssens-Maenhout et al., 2015) also uses a mosaic method combining national inventories of the USA and Canada, regional inventories for Europe and Asia with the global inventory EDGAR.

For the bottom-up approach, the more detailed information is obtained, the more accurate emissions with more detailed source categories can be estimated. In the early days of studies on emission estimates, especially over regions with little emission information, the input data for calculation were mainly determined by extrapolation and assumptions, which usually resulted in large uncertainties. Nowadays, with more specific information, the uncertainties of emission estimates for the bottom-up approach could be significantly reduced. The early inventories usually did not have complete information on all power plants or industry factories, even lacking their locations. For example, the Asian inventory REAS v2 (Kurokawa et al., 2013), which is an improved version of REAS, includes only 380 power plants for year 2008, while MIX has emissions from 2411 plants for the same year. Since the calculation of emissions using the bottom-up approach requires gathering enormous amounts of information, the updates of bottom-up inventories are usually slow. The official inventories provided by countries have a time lag of at least one year. The National Emissions Inventory of the United States for example is updated every three years.

Uncertainties can be estimated by using error propagation of uncertainties on activity data and emission factors (Streets et al., 2003) or Monte Carlo approach (Zhao et al., 2011), but most inventories do not provide emission uncertainties. For the same area, the variation of emissions given by different inventories can be quite large (Granier et al., 2011; Ding et al., 2017; Saikawa et al., 2017). It is very

tough to identify essential causes for the discrepancies during intercomparison of inventories, because detailed information on calculation input data and processes used to conduct the inventories are not always provided. Li et al. (2017) concluded that in the MIX inventory for Asia the uncertainty in NO_x emissions is up to 49 %. However, the evaluation of uncertainties in emissions is rather difficult because of the insufficient knowledge of human activities and emission measurements of the various sources, especially in developing countries with rapid changes of emission factors. For instance, China implements air quality control measures for NO_x emissions since 2011, but the exact start dates of operating the abatement equipment are usually difficult to obtain. Additionally, the information provided by different energy statistics, which are used as input data for emission calculations, are inconsistent. This inconsistency leads to significant difference in emissions (Hong et al., 2017).

In the last two decades, when satellite observations of NO_2 column concentrations became available, the temporal variation and spatial distribution of NO_2 have been better studied and understood (Richter et al., 2005; van der A et al., 2006). Emissions can be constraint using inversion techniques with satellite observations. This approach, called 'top-down' or satellite-derived, helps to significantly reduce the uncertainties of bottom-up inventories (Streets et al., 2013). In the next section, I briefly introduce the satellite-derived approach.

1.6. NO_x emission estimates from satellite measurements

1.6.1. Satellite observations

Using satellite observations of atmospheric species is an important way to monitor changes in NO_2 column concentrations, such as the trend and seasonality (Richter et al., 2005; van der A et al., 2006; Schneider and van der A, 2012), since satellites provide observations with global coverage and fixed spatial and temporal resolution, while in situ and airborne measurements of NO_2 have either temporal or spatial limitations.

In this thesis, I use observations from two instruments, the Global Ozone Monitoring Experiment 2 (GOME-2) and the Ozone Monitor Instrument (OMI), which are on the sun-synchronous polar-orbiting MetOp-A and EOS-Aura satellites, respectively. GOME-2 and OMI are optical spectrometers sensing the Earth's backscattered radiance and extra-terrestrial solar irradiance in the ultraviolet (UV) and visible

(VIS) wavelengths. Both instruments are nadir looking and have global coverage. The detected wavelength range is from 240 to 790 nm for GOME-2 and from 270 to 500 nm for OMI. Both of them have a relatively high horizontal resolution: GOME-2 has a pixel size of 80 km × 40 km, which changed to 40 km × 40 km after 15 July 2013; the pixel size of OMI is 24 km × 13 km at nadir and increases to 150 km × 28 km at the edge of the swath.

The principle of spectrometers to measure atmospheric trace gases is based on the fact that the radiation backscattered from the Earth's atmosphere and surface has been influenced by the light absorbing properties of the trace gases. The difference in the radiance spectrum reflected from the Earth and measured from the Sun can be used to retrieve information on concentrations of different gases since the absorbing properties are related to the type of gas molecule (see Figure 1.7). NO_2 abundances in the atmosphere can be retrieved through the VIS spectral window of 405 to 465 nm, where the NO_2 absorption features are strongest and the overlap with other absorbers is avoided.

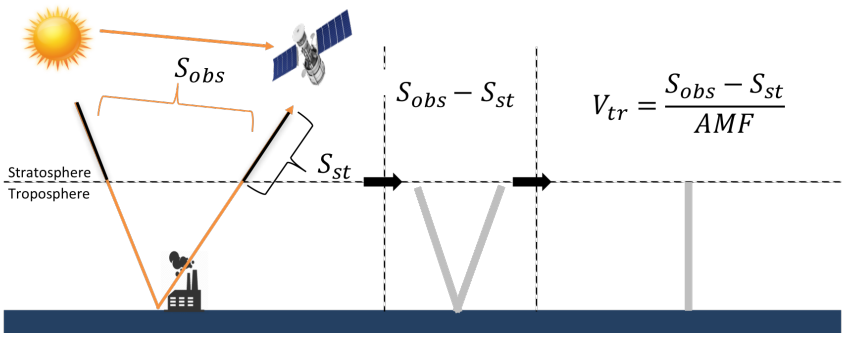

Figure 1.7: The principle of satellite observations and how to convert the total slant column (S_obs) to tropospheric vertical column (V_tr). The spectrometer on the satellite measures a spectra from the Earth's surface and the Sun. S_st is the stratospheric slant column. AMF is the air mass factor.

The satellite data of tropospheric NO_2 columns we used in this thesis are retrieved with the DOMINO v2 algorithm (Boersma et al., 2011). The first step in the algorithm is to use the Differential Optical Absorption Spectroscopy (DOAS) to determine NO_2 slant columns by fitting the differential absorption cross sections to the measured reflectivity spectrum. The NO_2 slant column is the amount of NO_2 along the average path length taken by photons within a fit window as travelling from the sun through the Earth atmosphere to the satellite instrument. The second step in the retrieval algorithm is to subtract the stratospheric contribution from the total slant column to get the tropospheric slant column. The information of the stratospheric contribution is obtained by assimilating slant columns into the TM4

global CTM. The last step is to convert the tropospheric slant column to a vertical column with the tropospheric air mass factor (AMF), which is calculated by a forward model including parameters such as cloud fraction, cloud height, a priori NO_2 vertical profile, terrain height and surface albedo. The calculation of the AMF is essential in the retrieval process, since the errors in the AMF can cause high biases of about 0 to 40 % in the retrieval data. To use only the retrievals of good quality, it is required to filter out observations with high cloud fractions and bright surface scenes. More detailed information about our filtering criteria is described in each chapter where retrieval data is used.

1.7. Emission estimates from space

Satellite-derived emissions have been developed to improve emission estimates and reduce uncertainties in existing inventories. Emission estimates using satellite observations started with a simple mass balance method. This method assumes that NO_x concentrations have an exponential decay, which depends on wind speed and lifetime, and that the diffusion of NO_x is negligible. Based on these assumptions, a linear relation between NO_x concentration and emissions is derived. With observations of NO_2, ratio between NO and NO_2, lifetime and wind speed, NO_x emissions can be estimated. Leue et al. (2001) first used this method to estimate annual emissions for various parts of the world. They estimated annual lifetime by using the exponential function of NO_2 decay with known annual NO_2 columns and wind speed. The ratio between NO_2 and NO was calculated by following a simple photochemical-stationary state among NO, NO_2 and O_3.

To improve the accuracy of emissions, Martin et al. (2003) used the mass balance method to estimate monthly emissions by obtaining information on lifetime and NO_2/NO ratio from a chemical transport model (CTM), which accounts for complex chemical reactions and calculates a concentration field from an emission inventory. To further improve the emissions derived from the mass balance method, they combined the emissions with a bottom-up inventory as a priori emissions by using the ratio of the simulated to the observed columns. An a posteriori inventory with error estimates was provided for the existing locations in the a priori emissions. In this method, it is assumed that the smearing length scale related to the short chemical lifetime of NO_x is less than the width of the model grid cell. This requires that the model simulations have a coarse resolution, which should be larger than at least 1°. The limitation of the mass balance method is that it neglects the influence of atmospheric transport and the non-local relation between emissions and concentrations. This is considered by Zhao and Wang (2009), who applied the

mass balance method iteratively on a daily basis to estimate monthly emissions by using high temporal and spatial resolution observations from the OMI instrument. Another way to describe the relation between tropospheric NO_2 columns and NO_x emissions is by performing multiple model runs with a random sampling of errors of both NO_x concentration and emission rate (Bayesian Monte Carlo method). Konovalov et al. (2006) applied this method using 100 different model runs to calculate the sensitivities in a 5 × 5 grid box around a grid cell, allowing for transport of short-lived chemical species. However, the method is very time consuming.

Advanced data assimilation methods, such as 4DVAR and the Kalman filter, are also used for emission estimates using satellite observations to consider the influence of transport and the non-linear and non-local relation between emissions and concentrations. The 4DVAR (four dimensional variational) data assimilation method, which is known as an adjoint technique, is applied to estimate NO_x emissions (Müller and Stavrakou, 2005; Stavrakou et al., 2008; Kurokawa et al., 2009). It is a method of estimating a set of parameters by optimizing the fit between model simulations and observations. The advantage of this method is that it can address non-linear problems and large number of control parameters. This technique depends on the evaluation of the gradient of the cost function with respect to the control variables, which are obtained by a backward adjoint model. However, the development of an adjoint model for a CTM is a complex and time-consuming task. The Kalman filter is an optimization technique without an adjoint model, which combines the model forecast with observations to give the 'best' estimate of the state variable. This optimization considers the weight of uncertainties in both observations and model forecasts and gives the uncertainty analysis of the estimated state variable. The challenge in using the Kalman filter method is to obtain the sensitivity of NO_2 on NO_x emissions and the error covariance of the model forecast.

Miyazaki et al. (2012) used an ensemble Kalman Filter to estimate global NO_x emissions. The sensitivity of NO_2 columns on NO_x emissions and their error covariance are obtained by the analysis of the spread of ensembles of model simulations. Mijling and van der A (2012) designed a fast inversion algorithm with high resolution to estimate regional NO_x emissions based on an extended Kalman filter using a 2D trajectory analysis to solve the non-local relation between emissions and NO_2 columns. A detail introduction of this algorithm will be shown in the next section since the thesis mainly focus on further developing and validating this algorithm to improve emission estimates of NO_x, especially over East Asia.

NO_x emissions derived from satellite observations through the inversion methods mentioned above are in good agreement with bottom-up inventories. This approach is able to provide a better temporal evolution of emissions, especially

its seasonality, which is difficult to capture in the bottom-up approach. The main advantage of using the satellite-derived approach is that we can get emissions soon after observations become available. A limitation of the satellite approach is to classify source categories, which usually requires a priori information from the bottom-up approach.

1.7.1. DECSO

The extended Kalman filter is used to optimise the state by combining model forecast and observations. Mijling and van der A (2012) developed the emission inversion algorithm DECSO (Daily Emission estimates Constrained by Satellite Observations) based on an extended Kalman filter. The application of the extended Kalman filter in NO_x emission estimates is different from data assimilation of trace gas concentrations, since it adjusts NO_x emissions based on observations of NO_2 concentration. In the DECSO algorithm, the state vector $\mathbf{e}$ consists of NO_x emissions. According to the Kalman filter, the cost function J at each time step t, in our case, describes the difference of simulated and observed concentrations and the difference of analysed and forecasted emissions weighted with their error covariances:

$$J(t) = [\mathbf{y}(t) - H(\mathbf{e}(t))]^T \mathbf{R}^{-1} [\mathbf{y}(t) - H(\mathbf{e}(t))] + \left[\mathbf{e}(t) - \mathbf{e}^f(t)\right]^T \mathbf{P}^f(t)^{-1} \left[\mathbf{e}(t) - \mathbf{e}^f(t)\right] \tag{1.1}$$

$\mathbf{e}^f$ is the vector of forecasts of NO_x emissions. $\mathbf{y}$ is the vector of observations of NO_2 columns. $\mathbf{P}^f$ is the error covariance matrix of the forecasted emissions $\mathbf{e}^f$. The optimal NO_x emissions are also referred to as the analysis of NO_x emissions $\mathbf{e}^a$, which are derived by minimizing of the cost function J:

$$\mathbf{e}^a(t) = \mathbf{e}^f(t) + \mathbf{K}\left[\mathbf{y}(t) - H\left(\mathbf{e}^f(t)\right)\right] \tag{1.2}$$

H is the observation operator, which describes the dependence of tropospheric NO_2 columns in a satellite pixel on emissions in a model grid. It is assumed that when H is applied to the true state, it introduces unbiased errors having a normal distribution around zero with covariance $\mathbf{R}$. A CTM is used to simulate NO_2 concentrations with a priori emissions as input. $H[\mathbf{e}(t)]$ can be calculated by transferring the simulated columns on the model grid onto the satellite footprint using area-weighted interpolation and applying the averaging kernel. The average kernel (AK)

from the satellite retrieval describes the sensitivity of the satellite instrument to the NO_2 density on different heights. The AK is applied to the modelled vertical profile to enable direct comparison between simulated and observed columns. **K** is called the Kalman gain, which is used to adjust NO_x emissions based on the weight of **R** and $\mathbf{P}^f$ through the following equation:

$$\mathbf{K} = \mathbf{P}^f(t)\,\mathbf{H}\left[\mathbf{H}\mathbf{P}^f(t)\,\mathbf{H}^T + \mathbf{R}\right]^{-1} \tag{1.3}$$

H is the Jacobian of the observation model H. It describes the sensitivity of tropospheric NO_2 columns in a pixel to changes in the emissions. An advantage of the Kalman filter is that it optimises the state vector and at the same time gives the error estimate of the state vector, according the following equation:

$$\mathbf{P}^f(t) = (\mathbf{I} - \mathbf{K}\mathbf{H})\,\mathbf{P}^f(t) \tag{1.4}$$

$\mathbf{P}^a$ is error covariance matrix of the analysis of the emissions $\mathbf{e}^a$. The forecast of the NO_x emissions $\mathbf{e}^f$ is calculated through an emission model M based on the analysis of emissions $\mathbf{e}^a$ from the previous time step:

$$\mathbf{e}^f(t + \Delta t) = M\left[\mathbf{e}^a(t)\right] \tag{1.5}$$

For the emission model M we assume persistency, which means that the emissions of tomorrow are equal to the emissions of today. The time step Δt of each emission forecast is one day, which corresponds to the time step of new satellite observations of NO_2 columns used in DECSO. **M** is the matrix representation of M, which is equal to the identity matrix **I**. The error covariance of the forecasted emissions $\mathbf{e}^f$ is calculated via:

$$\mathbf{P}^f(t + \Delta t) = \mathbf{M}\mathbf{P}^a(t)\,\mathbf{M}^T + \mathbf{Q}(t) \tag{1.6}$$

where **Q** is the covariance matrix of the modelled emissions $\mathbf{e}^f$.

To apply the Equation (1.1) – (1.6), we face two major challenges:

1. How to construct the Jacobian matrix **H**, which determines the relation between emissions NO_x and observations of NO_2. With the assumption that the decay of concentration follows an exponential function depending on the

lifetime τ of NO_x, the sensitivity H_{ij}^{*} of the concentration in grid cell i on emissions in grid cell j can be calculated with the equation:

$$\mathrm{H}_{ij}^{*}\left(\tau_j\right) = \gamma_i \frac{a_i}{a_j} \int_0^{t_n} e_j \Omega_{ij}\left(t\right) f_i\left(t_n - t\right) dt \tag{1.7}$$

where γ is the ratio of NO_2 and NO_x concentrations, and a represents the area of a model grid cell, Ω is the transport kernel, and f is an emission modulation function used to present diurnal cycles of the emissions. γ is described by the CTM.

The calculation of the transport kernel Ω is based on a simple 2D terrain-following a trajectory transport equation using a space dependent wind field. The source grid cell is divided into 150 sub grid cells. For each sub grid cell, a forward trajectory is calculated with an injection height, which is based on the NO_2 vertical profile. The lifetime of NO_x is calculated by solving the following equation:

$$\mathbf{c}\left(t_n\right) = \mathbf{G}\mathbf{c}\left(0\right) + \mathbf{H}^{*}\mathbf{e} \;\;,\;\; \left(G_{ij} = \frac{a_i}{a_j} e_j^{-\frac{t_n}{\tau_j}} \Omega_{ij}\left(t_n\right)\right) \tag{1.8}$$

where $\mathbf{c}(t_n)$ is the CTM simulated concentration after time step t_n, typically one day, starting from $\mathbf{c}(0)$. **G** describes the advection and decay of the initial concentration $\mathbf{c}(0)$ during time t_n. $\mathbf{H}^{*}\mathbf{e}$ describes how additional concentrations resulting from the emissions are distributed over the grid cells. Solving Equation 1.8 requires a single run of the CTM. We transfer $\mathbf{H}^{*}$ to **H** by applying the AK and vertical and horizontal interpolation/integration of grid cells on the satellite footprint. After this we have constructed the Jacobian matrix **H** for a single time step.

2. How to derive the error covariances **R** and **Q**:

   The covariance matrix **R** of the observation operator is calculated based on the statistics of the observation minus forecast (OmF). Covariance matrix **Q** of the emission model is determined by analysing different assumptions for several emission scenarios. The details of calculating these covariance matrices **Q** and **R** of the emission model and observation operator respectively will be discussed in chapter 3.

1.8. Research objectives and thesis overview

In general, a weak point of existing inventories is their low temporal resolution and their bad timeliness. The seasonal variability is normally poorly captured in emission inventories and often inventories are several years old. Small sources in remote

areas are sometimes missing in bottom-up inventories, such as newly built power plants. For East Asia, only few inventories exist that includes regional biomass burning and maritime emissions. The global inventories including these emissions have large uncertainties over this area due to the lack of information on local biomass burning and shipping activities. In principle, satellite-derived emissions can improve the above issues depending on the quality of the inversion algorithm, since satellite observations (e.g. from OMI) provide NO_2 columns with a daily global coverage and availability of a few hours after observation. Estimating emissions from satellite observations is relatively new, so that inversion algorithms still need a lot of development to provide more accurate emissions with higher resolution on both temporal and spatial scales. All emission inventories, both bottom-up and satellite-derived, are facing the same challenge of validation due to the difficulty in directly measuring emissions on the ground on a large scale.

In my PhD study, I used the DECSO algorithm to estimate NO_x emissions over East Asia. The main concept of the algorithm is the combination of chemical transport model simulations and observations to adjust emissions. This means that the accuracy of emissions is not only related to the algorithm itself but also to the quality of the model and satellite retrievals used in DECSO. How to improve the DECSO algorithm and how to validate the derived emissions are the main objectives of this thesis.

In Chapter 2, we improve the algorithm to better resolve small-scale emission changes in time and location. The improvements consist of an updated CTM and better filtering of erroneous satellite observations. To demonstrate the quality of the improved algorithm, we took the Youth Olympic Games held in Nanjing as a case study, since strict air quality regulations have been taken by the local authority to reduce NO_x emissions during this event.

Chapter 3 concentrates on the improvements of emission estimates over remote areas since important emissions exist in remote places, where information on emissions is difficult to obtain and often lacking, for example, over the ocean. Small artificial emissions that sometimes are the results of the DECSO algorithm over clean areas are referred to as background noise. With this background noise, weaker emission sources in these clean areas, such as shipping emissions, are difficult to detect. Chapter 4 shows that the improvements of DECSO enable us to detect maritime emissions near the Chinese coast, which are often hidden in the outflow of observed NO_2 columns from the mainland of China. Based on the long-term record of NO_2 satellite observations from OMI, the emissions from 2007 to 2016 over the Chinese seas are presented. A persistent increase in shipping emissions is shown following the trend in cargo trade volumes.

In chapter 5, uncertainties of NO_x emissions have been investigated via an intercomparison of nine inventories derived using both bottom-up and satellite-derived approaches over East Asia. The analysis shows that the uncertainties rapidly increase when the spatial and temporal scales decrease. Several recommendations are suggested for both satellite-derived and bottom-up approaches to further improve NO_x emissions.

In the last chapter, I present the concluding remarks and an outlook on future research.

2

NO_x emissions estimates during the 2014 Youth Olympic Games in Nanjing

The Nanjing Government applied temporary environmental regulations to guarantee good air quality during the Youth Olympic Games (YOG) in 2014. We study the effect of those regulations by applying the emission estimate algorithm DECSO (Daily Emission estimates Constrained by Satellite Observations) to measurements of the Ozone Monitoring Instrument (OMI). We improved DECSO by updating the chemical transport model CHIMERE from v2006 to v2013 and by adding an Observation minus Forecast (OmF) criterion to filter outlying satellite retrievals due to high aerosol concentrations. The comparison of model results with both ground and satellite observations indicates that CHIMERE v2013 is better performing than CHIMERE v2006. After filtering the satellite observations with high aerosol loads that were leading to large OmF values, unrealistic jumps in the emission estimates are removed. Despite the cloudy conditions during the YOG we could still see a decrease of tropospheric NO_2 column concentrations of about 32 % in the OMI observations when compared to the average NO_2 columns from 2005 to 2012. The results of the improved DECSO algorithm for NO_x emissions show

This chapter has been published in Atmospheric Chemistry and Physics as Ding et al.(2015).

a reduction of at least 25% during the YOG period and afterwards. This indicates that air quality regulations taken by the local government have an effect in reducing NO_x emissions. The algorithm is also able to detect an emission reduction of 10% during the Chinese Spring Festival. This study demonstrates the capacity of the DECSO algorithm to capture the change of NO_x emissions on a monthly scale. We also show that the observed NO_2 columns and the derived emissions show different patterns that provide complimentary information. For example, the Nanjing smog episode in December 2013 led to a strong increase in NO_2 concentrations without an increase in NO_x emissions. Furthermore, DECSO gives us important information on the non-trivial seasonal relation between NO_x emissions and NO_2 concentrations on a local scale.

2.1. Introduction

Reducing air pollution is one of the biggest environmental challenges currently in China. Nearly 75 % of urban areas are regularly polluted in a way that was considered unsuitable for their inhabitants in 2004 (Shao et al., 2006). In mega cities and their immediate vicinities, air pollutants exceed the Chinese Grade-II standard ($80 \mu g\, m^{-3}$ for daily NO_2) on 10–30 % of the days between 1999 to 2005 (Chan and Yao, 2008). Air pollution is directly related to the economic growth in China and its accompanying increase of energy consumption. In the last 2 decades, air pollutants persistently increased in China. For instance, satellite measurements showed that NO_2 column concentrations increased about by 50 % from 1996 to 2005 (Irie,2005; Richter et al., 2005; van der A et al., 2006). By combining satellite observations with air quality models, Itahashi et al. (2014) showed that the strong increase of NO_2 columns over East China was caused by a doubling of NO_x (NO_x = NO + NO_2) emissions from 2000 to 2010. Zhang et al. (2007) found that NO_x emissions increased by 70 % between 1995 and 2006 and Lamsal et al. (2011) found that anthropogenic NO_x emissions increased 18.8 % during the period 2006 to 2009.

Table 2.1: Air-quality regulations taken by the Nanjing authorities in the year of YOG2014. The period is the start time of different regulations. The italic regulations are still effective after the YOG.

Period	Regulations
1 May – 30 June	The local government started to shut down the coal-burning factories.
1 – 15 July	All coal-burning factories have been shut down.
16 – 31 July	The work on one third of construction sites was stopped. The parking fees in downtown increased sevenfold.
1 – 15 August	The work on 2000 construction sites was stopped. Heavy-industry factories reduced manufacturing by 20 percent. *Vehicles with high emissions were banned from the city*. Open space barbecue restaurants were closed. *900 electric buses and 500 taxis have been put into operation.*
16 – 31 August	The work at all construction sites was put on hold.

Nanjing, the capital of Jiangsu Province, is a highly urbanized and industrialized city located in East China, in the northwest part of the Yangtze River Delta (YRD). By 2012, the area of Nanjing had a population of 8.2 million (Nanjing statistical Bureau, 2013). The YRD is one of the largest economic and most polluted regions in China.

Tu et al. (2007) found that the largest fraction of air pollution by NO_x and SO_2 can be attributed to local sources in Nanjing. Li et al. (2011) concluded that air pollutant concentrations and visibility demanded urgent air pollution regulations in the YRD region. From 16th to 29th August 2014, the Youth Olympic Games (YOG) were held in Nanjing. To guarantee good air quality during the Games, the city government carried out temporary strict environmental regulations with 35 directives from May to August. Other cities in the YRD cooperated with Nanjing to ensure good air quality during the Games. The periods with the main regulations are shown in Table 2.1. In addition, several technical improvements have been implemented to reduce pollution from heavy industry and power plants.

For previous major international events in China, local authorities have tried to comply with the air quality standards of the World Health Organization (WHO), which has a limit of 200 $\mu g\,m^{-3}$ for hourly NO_2 concentrations. For each event, the local government imposed restrictions on heavy industry, construction and traffic. In 2008 the Beijing Municipal Government implemented a series of air pollution control measures for Beijing and surrounding cities to guarantee good air quality for the 29th Olympic Games. These control measures significantly reduced the emissions and concentrations of pollutants. Satellite data show that the NO_2 column concentrations decreased at least 40 % compared to previous years (Mijling et al., 2009; Witte et al., 2009). Both bottom-up and top-down emission estimates show a decrease of about 40 % in NO_x emissions (Wang et al., 2009; Mijling et al., 2013; Wang et al., 2010). During the 2010 World Expo in Shanghai the NO_2 column was reduced by 8 % from May to August according to an analysis of Hao et al. (2011) of space-based measurements compared to previous years. In November 2010 emission reduction measures introduced by the Guangzhou authorities also successfully improved air quality for the Asian Games. Wu et al. (2013) claimed a NO_x emission reduction of 43.5 % based on mobile DOAS measurements. The emission reduction of NO_x based on model simulations was estimated to be about 40 % (Liu et al., 2013).

However, to study the effectiveness of the air quality measures, it is not enough to look at the concentration measurements alone, as the reduction of air pollutants can also be affected by favorable meteorological conditions. Emissions need to be derived to better show the effect of temporary air quality regulations carried out for the Games. Up-to-date emission data are difficult to obtain, as most emission inventories are developed by a bottom-up approach based on statistics on source sector, land-use and sector-specific emission factors.

The bottom-up approach introduces large uncertainties in the emission inventories. To improve emission inventories, a top-down approach can be used by

estimating emissions from satellite observations (Streets et al., 2013). For constraining emissions of short-lived species, Martin et al. (2003) used the ratio of the simulated to the observed column to scale a priori emissions. They used optimal estimation to weigh the a priori emission inventory with the top-down estimates, resulting in an a posteriori inventory with error estimates. This method assumes that the relationship between emissions and concentrations is not affected by transport. Non-linear and non-local relations between emission and concentration can be indirectly solved by applying the method iteratively (e.g. Zhao and Wang, 2009), although a posteriori error estimates are lost in this way. Kurokawa et al. (2009) and Stavrakou et al. (2008) used 4DVAR techniques to estimate emissions by applying an adjoint model of the chemistry transport model to calculate the sensitivities. Another popular data assimilation method is the ensemble Kalman filter (Evensen, 2003), which does not require an adjoint model and is relatively easy to implement. As an extension of the Kalman filter, it employs a Monte Carlo approach to represent the uncertainty of the model system with a large stochastic ensemble. Whenever the filter requires statistics such as mean and covariance, these are obtained from the sample statistics of the ensemble (Miyazaki et al., 2012).

To get fast updates for short-lived air pollutants, Mijling and van der A (2012) designed a Daily Emission estimates Constrained by Satellite Observation (DECSO) algorithm. DECSO is an inversion method based on an extended Kalman filter. The algorithm only needs one forward model run of a chemical transport model (CTM) to calculate all local and non-local emission/concentration relations. It updates emissions by addition instead of scaling, enabling the detection of unaccounted emission sources.

In this study, we use the latest version of DECSO with OMI satellite data to study how the environmental regulations affect the NO_x emissions in Nanjing during the 2014 YOG. Detecting emission changes for Nanjing is challenging, as it is a smaller city than, e.g., Beijing. In addition, Nanjing is in one of the most populated areas of China close to Shanghai with a population of about 24 million. Therefore we have introduced a few improvements in the DECSO algorithm to better resolve small-scale emission changes in time and location. The improvements consist of an updated CTM and better filtering of erroneous satellite observations. The emission estimates will be based on the satellite observations of OMI, taking advantage of its high spatial resolution needed to resolve the changes in the Nanjing area. With this improved algorithm we will compare the NO_x emissions during the YOG with NO_x emissions of the previous year in the Yangtze Delta River.

2.2. Methods

2.2.1. Emission estimates

For the emission estimates of NO_x over China we use the DECSO algorithm (Mijling and van der A, 2012). It uses a CTM to simulate the NO_2 concentrations and daily satellite observations of NO_2 column concentrations to constrain NO_x emissions. The algorithm is based on an extended Kalman filter to get new emission estimates by optimizing NO_2 column concentrations of model and satellite observations. The inclusion of sensitivities of NO_2 column concentrations on the NO_x emissions in other locations is an essential part of DECSO. A terrain-following trajectory analysis is used in this calculation to describe the transport of NO_2 over the model domain for a time interval between two overpasses of the satellite instrument. This approach results in a fast algorithm suitable for daily estimates of NO_x emissions on a $0.25^\circ \times 0.25^\circ$ resolution. A detailed description of DECSO v1 can be found in Mijling and van der A (2012).

The CTM used in DECSO is CHIMERE (Schmidt, 2001; Bessagnet et al., 2004; Menut et al., 2013). CHIMERE is implemented on a $0.25^\circ \times 0.25^\circ$ spatial grid over East Asia from 18° N to 50° N and 102° E to 132° E. It contains 8 atmospheric layers up to 500 hPa. The meteorological input for CHIMERE is the operational meteorological forecast of the European Centre for Medium-Range Weather Forecasts (ECMWF) with a horizontal resolution of approximately 25 km × 25 km. The Multi-resolution Emission Inventory for China (MEIC) (He, 2012) for 2010 gridded to a resolution of $0.25^\circ \times 0.25^\circ$, is used for the initial emissions in DECSO. Outside China, where no MEIC emissions are defined, the emission inventory of INTEX-B (Q. Zhang et al., 2009) is used. As the emission sector definition used in MEIC and INTEX-B does not match the 11 activity sectors according to the SNAP (Selected Nomenclature for Air Pollution) 97, which are internally used in the CHIMERE model, we estimate the redistribution of the emissions over the sectors (see Table 2.2).

As mentioned by Mijling and van der A (2012), to compare CHIMERE simulations with satellite observations, we extend the modeled vertical profiles from 500hPa to the tropopause by adding a climatological partial column, which is from an average of a 2003–2008 run of the global chemistry transport model TM5. The simulated NO2 column concentrations on the model grid are redistributed to the satellite footprints. To enable direct comparison between simulated and observed tropospheric vertical column, the averaging kernel from the satellite retrieval is then applied to the modeled vertical profile.

In this study, we used an updated version of DECSO, which is referred to as

Table 2.2: Estimated redistribution of MEIC sectors over SNAP 97 sectors.

	MEIC sectors				
SNAP 97 sectors	Power	Industry	Transport	Residential	Agriculture
Combustion in energy and transformation industries	1	–	–	–	–
Non-industrial combustion plants	–	–	–	1	–
Combustion in manufacturing industry	–	0.3	–	–	–
Production process	–	0.3	–	–	–
Extraction and distribution of fossil fuels and geothermal energy	–	0.4	–	–	–
Solvent and other product use	–	–	–	–	–
Road transport	–	–	1	–	–
Other mobile sources and machinery	–	–	–	–	–
Waste treatment and disposal	–	–	–	–	–
Agriculture	–	–	–	–	1
Other source and sinks	–	–	–	–	–

DECSO v3a. In particular, the calculation speed has been improved in this update. DECSO does not distinguish between biogenic emissions and the anthropogenic sectorial emissions. Emission differences are attributed to anthropogenic contribution only, i.e., the biogenic emissions are assumed to be modeled correctly by the CTM. Emission updates are distributed by ratio over the sectors (power, industry, transport, domestic) as described by the a priori emission inventory. If a grid cell is dominated by power plant emissions, however, emission updates are attributed to the power sector only. The locations of power plants are provided to the algorithm as additional a priori information. In DECSO v3a, the emission injection height has been made sector-dependent. Emissions are injected in the lowest three model layers of the CTM; each sector having its own characteristic vertical emission distri-

bution. For example, transport emissions are released at the surface, while power plant emissions are fully released in the third model layer corresponding to a typical smokestack height. Trajectory calculations of the observed species are crucial in the determination of the source-receptor relations. The DECSO algorithm uses meteorological wind fields (the same as used in the CTM) to calculate how the content of a tropospheric column is advected over the model domain. Here, the injection heights are distributed according to the modeled vertical NO_x distribution. In DECSO, the forward trajectory calculation is changed to a backward trajectory calculation, i.e., the source-receptor relations are calculated backward in time, based on the height distribution of NO_x modeled at satellite overpass time.

In DECSO v3a, tuned synthetic error estimates E_{obs} estimates are used, derived from the original satellite observation via

$$E_{obs} = f \cdot E_{sat} + (1 - f) \cdot (0.5 \cdot E_{sat}), \text{with } f = e^{(-\frac{c_{sat}}{2})}, \quad (2.1)$$

where E_{sat} is the original observation error from the retrieval method and C_{sat} is the retrieved NO_2 column of the satellite observation. The unit in this formula is 10^{15} molecules cm^{-2}. The modified errors give more weight to satellite observations with high values during the assimilation by reducing their relative error while maintaining the dominating absolute error for low values (typically around 0.5×10^{15} molecules cm^{-2}). In this way, DECSO better captures new emission points or high-emission episodes.

2.2.2. Satellite observations

In this study, satellite observations from the Dutch-Finnish Ozone Monitoring Instrument (OMI) on NASA's Aura satellite (Levelt et al., 2006) are used in DECSO. The satellite was launched on 15 July 2004 into a sun-synchronous polar orbit at 705 km altitude. OMI is a nadir-viewing spectrometer measuring the atmosphere-backscattered solar light in the ultraviolet-visible (UV/VIS) range from 270 to 500 nm with a spectral resolution of about 0.5 nm. The 114° wide view of OMI results in a swath width of 2600 km, providing daily global coverage in about 14 orbits. The local overpass time is around 13:30 local time (LT). The pixel size of OMI is 24 km × 13 km at nadir and increases to about 150 km × 28 km at the end of the swath.

We use the tropospheric NO_2 vertical column concentrations retrieved with the Dutch OMI NO_2 retrieval (DOMINO) algorithm version 2 (Boersma et al., 2011). The data set is available on the Tropospheric Emissions Monitoring Internet Service (TEMIS) portal (http://www.temis.nl). The DOMINO algorithm first obtains NO_2

slant columns from the OMI reflectance spectra by using Differential Optical Absorption Spectroscopy (DOAS). After separating the stratospheric and tropospheric contribution to the slant column, DOMINO converts the tropospheric slant column to a vertical column with the tropospheric air mass factor (AMF) (Boersma et al., 2007, 2011). DOMINO v2.0 mainly improves the NO_2 air mass factor by improved radiative transfer, surface albedo, terrain height, clouds and a priori vertical NO_2 profiles. The bias between DOMINO v2.0 and Multi-Axis Differential Optical Absorption Spectroscopy (MAX-DOAS) ground observations at five locations is only -10 $\pm$ 14 % over China and Japan (Irie et al., 2012). The DOMINO algorithm does not explicitly account for the effect of aerosols on the solar radiation. Rather it is indirectly accounted for by the higher cloud fraction in aerosol contaminated scenes. However, Lin et al. (2014) concluded that especially in China the effects of aerosols and surface reflectance anisotropy have implications for retrievals of NO_2 from OMI and suggested that exclusion of high aerosol scenes supports better emission estimates at fine spatial and temporal scales.

Since 25 June 2007, OMI data have been affected by the so-called row anomaly, which deteriorates the spectral observations for particular viewing directions of OMI (Boersma et al., 2011; Kroon et al., 2011). Twenty-nine out of the 60 rows are affected by the row anomalies and no longer used after 1 January 2011. We also filter out the four pixels at either side of the swath, because the size of these pixels is 3 times larger than the model grid cell. After the filtering, the largest footprint is about 75 km $\times$ 21 km. To reduce the influence of cloudy and bright surface scenes on the quality of the retrieval product, we use only observations having a surface albedo lower than 20 % to remove observations over snow and ice (Product Specification Document of DOMINO v2 on www.temis.nl). The observations with clouds below 800 hPa are also filtered out as these retrievals are very sensitive to small differences in the NO_2 profile shape and the retrieved cloud height. Mijling and van der A (2012) filter out the observations with a cloud fraction higher than 20 %. Based on this filtering, there are no tropospheric NO_2 satellite observations over Nanjing during the YOG due to the cloudy conditions at the overpass time of the satellite. Thus, to obtain more NO_2 satellite observations, we use observations with a cloud radiance fraction lower than 70 % (comparable with a cloud fraction of about 30–35 %) instead of the cloud fraction lower than 20 %. From our analysis of the satellite data we conclude that as a result of this new limit on the cloud fraction the error on the measurements increases by less than 20 % and without introducing biases. Yet this effect is compensated by the advantage that more data becomes available. The number of observations over the whole domain increases by about 37 % on average.

2.2.3. Ground-based observations

To validate the model results in Nanjing, we use available independent measurements from the national in situ observation network, which are collected and maintained by the China National Environmental Monitoring Center (CNEMC). The aqicn.org team publishes the hourly Air Quality Index (AQI) of specific air pollutants, such as NO_2, SO_2, and particulate matter (PM_{10} and $PM_{2.5}$), on their website based on the measurements from CNEMC. The AQI is calculated by the conversion table from the Technical Regulation on Ambient Air Quality Index in China published by the Ministry of Environmental Protection (http://kjs.mep.gov.cn/hjbhbz/bzwb/dqhjbh/jcgfffbz/201203/W020120410332725219541.pdf). We use the same table to convert the AQI back to the surface concentration unit of $\mu g\,m^{-3}$. For this study, the NO_2 hourly in situ measurements of Nanjing for the period of April 2013 to December 2014 are used. The location of these measurements is the Nanjing People's Government building, which is located in the center of Nanjing. Interpretation of the validation results is troubled by the absence of peripheral information of the in situ measurements. For instance, the type of instrument is unknown and the exact location of the measurement such as the height or the distance to a local traffic road is unclear.

2.3. Improvements of DECSO

2.3.1. Model improvement

The performance of the CTM is important for the DECSO results. CHIMERE v2006 is an outdated model version which has been used in DECSO algorithm versions up to v3a. To improve the emission estimation results, we updated the CTM to CHIMERE v2013 (DECSO v3b).

The new model adds biogenic emissions of six species: isoprene, α-ioporene, α-pinene, β-pinene, limonene, ocimene and NO. These biogenic emissions are calculated by the model preprocessor using the MEGAN model and land use data (Menut et al., 2013). The added biogenic emissions can affect the emissions estimated for rural areas as biogenic NO emissions in rural areas cannot be neglected in summertime. Compared to the old version of CHIMERE, the new model version includes a more advanced scheme for secondary organic aerosol chemistry. In addition, the chemical reaction rates are updated and a new transport scheme is used in the new CHIMERE model. The new CHIMERE model includes the emission injection height profile for different emission sectors. For CHIMERE v2013 we use the same input data except for the land use data. We use land use data from the GlobCover Land

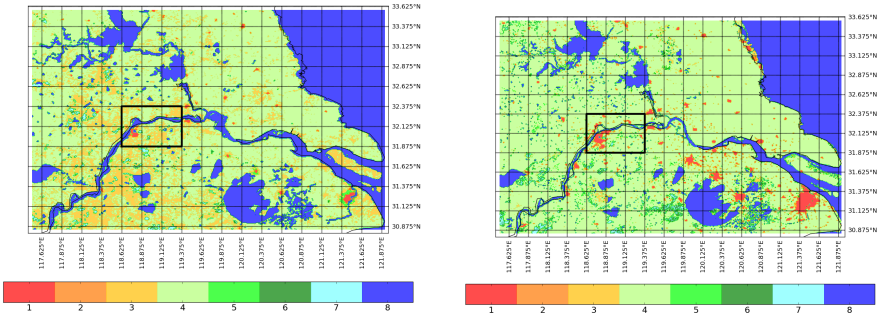

Figure 2.1: Land use over the Jiangsu Province from Global Land Cover Facility (1994) (left) and the GlobCover Land Cover (2009) (right) and as used in CHIMERE v2006 and CHIMERE v2013. The eight categories are: 1. Urban, 2. Barren land, 3. Grassland, 4. Agricultural land, 5. Shrubs, 6. Needleleaf forest, 7. Broadleaf forest, 8. Water. The solid rectangle (about 50 km × 90 km indicates the 6 grid cells that cover the Nanjing area.

Cover (GCLC version 2.3) database, which are updated for the year 2009, while the land use database included in CHIMERE v2006 is the Global Land Cover Facility (GLFC) giving the land use of 1994. As China is a fast developing country, the land use may have large differences in 15 years due to urbanization (see Figure 2.1). Thus, the updated land use database will positively affect the model simulations over China.

To assess the effect of the new CTM, we run DECSO v3a and DECSO v3b for the period January 2013 to August 2014. Figure 2.2 shows the comparison of the average diurnal cycle of surface NO_2 concentrations from the two CHIMERE models with in situ observations in Nanjing averaged for January to August 2014. We select the $0.25° \times 0.25°$ model grid cell that contains the in situ measurement location. According to GCLC database, 70 % of the grid cell is urban area. We see that the surface NO_2 concentration of CHIMERE v2013 during nighttime is closer to the observations than for CHIMERE v2006. Our earlier model evaluations of CHIMERE showed that the nocturnal surface NO_2 concentrations simulated by CHIMERE v2006 are usually too high in urban areas caused by unrealistically low boundary layer heights and too little vertical diffusion. In CHIMERE v2013, the boundary layer heights over urban areas are limited by a minimum boundary layer height. As expected, v2013 improves the surface concentration simulation at nighttime, while differences during daytime are rather small compared to the in situ observations. We calculate the bias and root mean square error (RMSE) between the model results and in situ observations. The bias of CHIMERE v2013 is 3.7 $\mu g\,m^{-3}$, which is 10 $\mu g\,m^{-3}$ smaller than for CHIMERE v2006. The difference of RMSE between the two models is very small,

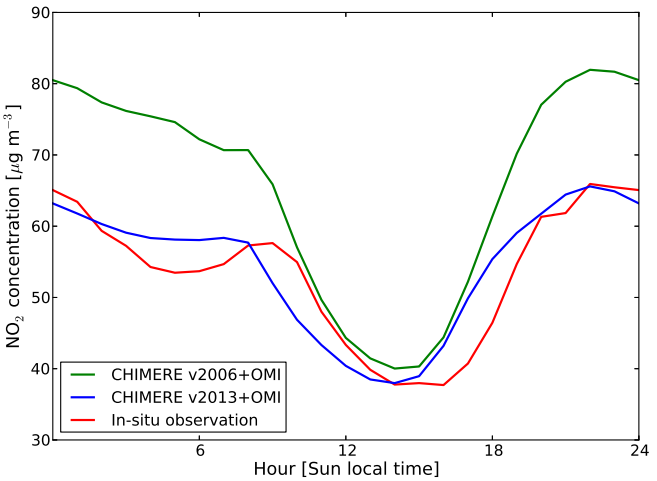

Figure 2.2: The diurnal cycle in Nanjing from January to August 2014 according to in situ observations, OMI-assimilated CHIMERE v2013 and CHIMERE v2006.

the RMSE of CHIMERE v2013 is 28 $\mu g\,m^{-3}$ and of CHIMERE v2006 is 31 $\mu g\,m^{-3}$. For the satellite overpass time, the bias improves from 4.4 to 1.8 $\mu g\,m^{-3}$ while the RMSE remains the same. However, in urban areas the local sources have transient influences on in situ observations. Blond et al. (2007) concluded that urban in situ observations of NO_2 cannot be used for the validation of a CTM model with low spatial resolution because the representativeness of the in situ measurement for the grid cell is very low. In spite of this, by using the 8-month average of the diurnal cycle to reduce the transient influences on the in situ measurements, we see some improvements for averaged NO_2 concentrations in CHIMERE v2013.

In order to get a more comprehensive validation of the model results, we compare the two CHIMERE models with OMI satellite observations. During the data assimilation of DECSO the daily Observation minus Forecasts (OmF) values have been stored. The OmF is a common measure for the forecasting capabilities of the model in the data assimilation. We compare the absolute OmF of both models for the summer (June to August) of 2014 in Figure 2.3. In the Figure a linear regression is fitted through the data points that shows the absolute OmF of CHIMERE v2013 is lower than that of CHIMERE v2006 indicating a better performance of CHIMERE v2013 in summertime. However, the absolute OmF of two models is similar in wintertime. Since biogenic emissions are negligible in wintertime, this may point to an effect of the missing biogenic emissions in the older version of CHIMERE. Based on these comparisons we selected CHIMERE v2013 in DECSO v3b for NO_x emission

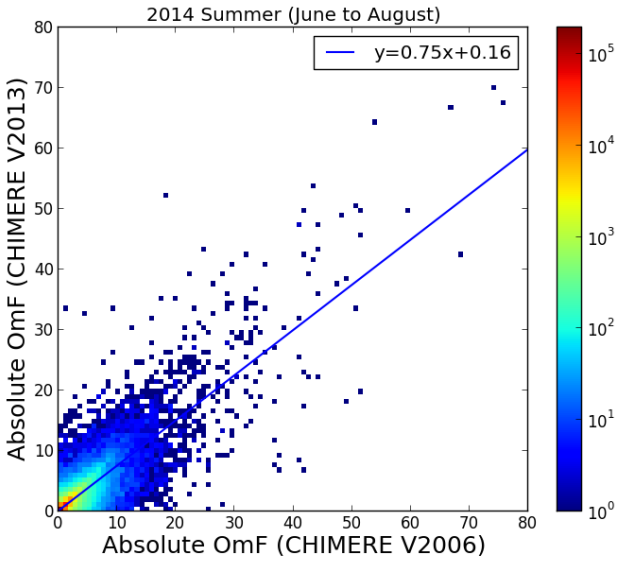

Figure 2.3: The comparison of the absolute OmF (10^{15} molecules cm^{-2}) of CHIMERE v2006 and CHIMERE v2013 for the whole East Asian domain from June to August. The colorbar represents the frequency of satellite observations for that specific value of OmF.

estimates in this study.

2.3.2. Quality control of satellite data

Earlier studies showed that the DOMINO v2 retrievals do not account enough for the effect of high aerosol concentrations on NO_2 columns (see Section 2.2.2) and at the same time we know that high aerosol concentrations are a significant problem in most megacities in China. When checking the time series of NO_x emissions over Nanjing for 2013 by DECSO v3b, we find some suspicious fluctuations at particular days. At these dates the derived NO_x emissions drop to zero in 1 day and then slowly increase again to the previous emission levels in the following days. These unrealistic emission updates concurred with extreme OmF values (lower than -5×10^{15} or higher than 10×10^{15} molecules cm^{-2}) with relative small OmF variances, which are calculated as the quadratic sum of model and observation errors (Figure 2.4). In the time period of our study there are 20 days with these extreme OmF values, 6 are positive and 14 are negative. All are having a significant impact on the NO_x emissions. For most of those 20 days, the in-situ observations of PM10 from CNEMC (see Section 2.2.3) show high aerosol concentrations, which are above 100

$\mu g\,m^{-3}$ in Nanjing. We also see a strong haze above Nanjing for all these 20 days from visual inspection of the MODIS RGB images. In addition, we notice that the MODIS images show higher cloud fractions than the fractions retrieved from OMI observations. The deviating of cloud fraction information from the OMI satellite retrieval is probably due to the aerosol conditions, which are not taken into account in the cloud retrieval algorithm (Acarreta et al., 2004; Stammes et al., 2008). High aerosol concentrations can not only complexly affect the cloud fraction and cloud pressure retrieval but also directly affect the NO_2 retrieval and results in either over- or under- estimated NO_2 column concentrations (Lin et al., 2014).

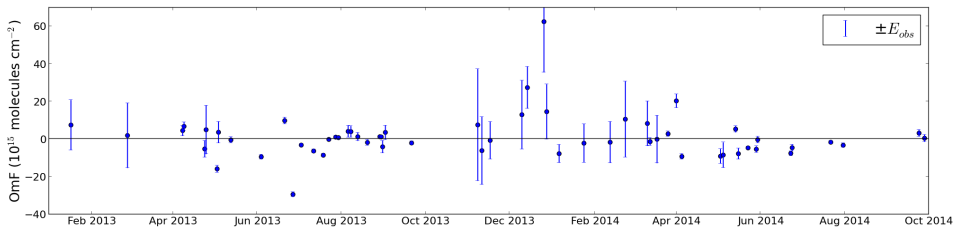

Figure 2.4: The time series of the OmF from January 2013 to September 2014 for the single grid cell over the center of Nanjing. The error bar is the root mean square error of observations (E_{obs}).

Figure 2.5 shows an example of such an extreme case for East China on 6 May 2013 with high (positive) OmF values in combination with low observational uncertainties (Equation 2.1). In the image we identify two areas with satellite observations that are at least 10×10^{15} molecules cm^{-2} higher than the model forecast. One is over the Hulunbuir sand land at the border of China and Mongolia, the other one is around the Bohai Bay. We compared the observations with the MODIS RGB and Aerosol Optical Depth (AOD) images on that day (Figure 2.6). The MODIS AOD image shows high aerosol values around the Bohai Bay and over the Hulunbuir sand land. The RGB image of MODIS shows haze around the Bohai Bay, which indicates that high aerosol concentrations are presented in that area. However, the aerosol information is not used in the retrieval of the DOMINO NO_2 product leading to NO_2 observations that are strongly deviating from the model forecast.

The effect of high aerosol concentrations on the NO_2 retrieval is non-linear and depends strongly on both the type of aerosol and its concentration. Also the height of the aerosol layer and the presence of clouds play a role (Leitão et al., 2010; Lin et al., 2014). It is therefore difficult to filter out outliers in the observed NO_2 based on aerosol data. In the data assimilation it is assumed that the OmF distribution is Gaussian and the OmF can be used to filter outliers from the data. So far, no OmF outlier criterion has been used in DECSO. Our previous analysis, however, shows

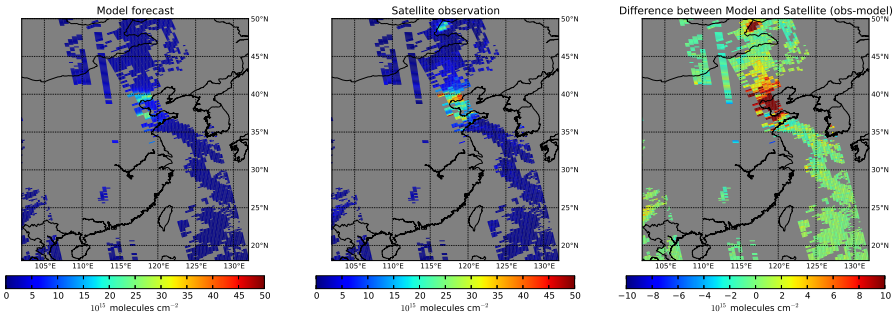

Figure 2.5: The comparison of the CHIMERE v2013 forecast (left) with OMI satellite observations (middle) on 6 May 2013. The right plot shows the difference between observations and forecast (OmF).

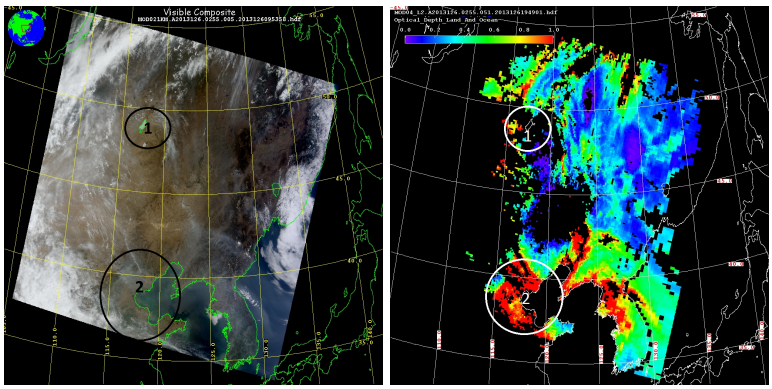

Figure 2.6: The RGB image (left) and Aerosol Optical Depth (right) from MODIS on 6 May 2013. Circle 1 and circle 2 represent the Hulunbuir sand land andthe Bohai Bay respectively. (The figures are from https://ladsweb.nascom.nasa.gov/browse_images/granule_browser.html).

the need for the detection of outliers. A filter has to be implemented with care, to avoid the algorithm becoming insensitive to new emission sources such as new power plants. Not losing sensitivity to new emission sources is also the reason we do not choose a relative filter criterion. We select an OmF filter criterion in the range of $[-5, 10] \times 10^{15}$ molecules cm^{-2} based on our analysis discussed below.

The distribution of OmF of all pixels over our domain from January 2013 to September 2014 is Gaussian except for its tails and 97 % of the OmF is in the interval of $[-5, 10] \times 10^{15}$ molecules cm^{-2}. However, over highly polluted areas both satellite observations and model results have larger errors resulting in higher OmF values. In addition, the lifetime of NO_2 is much longer in winter than in summer. Therefore, the NO_2 column concentration is higher than in summer, which

may lead to large OmF values in winter time. We choose 15 high-polluted cities in China based on AQI and study the distribution of the OmF for the summer period (April to September, 2013) and the winter period (October, 2013 to March, 2014) (Figure 2.7). As expected, the distribution of OmF is wider in winter than in summer. In summer, 70 % of the OmF values are in the interval of [–5, 10] $\times$ 10^{15} molecules cm^{-2}, while in winter 50 % of the OmF values are within [–5, 10] $\times$ 10^{15} molecules cm^{-2}. We select an asymmetric interval because the assimilation is especially sensitive to very negative outliers in OmF caused by low observations (having small observational errors associated), as opposed to very positive outliers caused by high observations, which are associated with large observational errors. The observations with low error have more weight in the data assimilation process. To figure out the effect of a large OmF on NO_x emission estimates, we compare a free run of CHIMERE v2013 with the MEIC inventory with a run with the DECSO v3b assimilation. During the summertime (June to August), the difference in the seasonal average of the NO_2 column concentration between these two runs is 4.8 $\times$ 10^{15} molecules cm^{-2} in the Nanjing area (six grid cells). This column difference is caused by the NO_x emission difference of 9.2 $\times$ 10^{15} molecules cm^{-2} h^{-1}. From a simple back-of-the-envelope calculation we derive that a negative 5 $\times$ 10^{15} molecules cm^{-2} difference in NO_2 columns requires a 9.6 $\times$ 10^{15} molecules cm^{-2} h^{-1} emission change, which would mean that all NO_x emissions in Nanjing would be removed in a single day. This change in emission is comparable to the total emissions of two large-sized coal-fired power plants. This shows that a change in OmF of 5 $\times$ 10^{15} molecules cm^{-2} is very unrealistic even in the most extreme cases. Therefore, this limit will be used as a criterion to filter outliers, which are in general caused by wrong NO_2 retrievals. To avoid the influence of the extreme OmF on emission estimates and still be able to monitor real emission changes, we filter out negative OmF values lower than 5 $\times$ 10^{15} molecules cm^{-2} and positive OmF values more than 10 $\times$ 10^{15} molecules cm^{-2} to be conservative. After applying the OmF filter criteria, we filter out 16 % of the extreme OmF in the polluted cities and less than 3 % in the whole domain. The large unrealistic jumps in emission disappear from the time series.

2.4. Emission analysis for the Nanjing Youth Olympic Games

First, we compare NO_2 monthly average concentrations in 2014 with previous years using in situ and satellite observations. For the in-situ observations we select the monthly mean at 13:00 LT to be able to compare the results with the satellite observations whose overpass time is about 13:30 LT (see Figure 2.8), which is

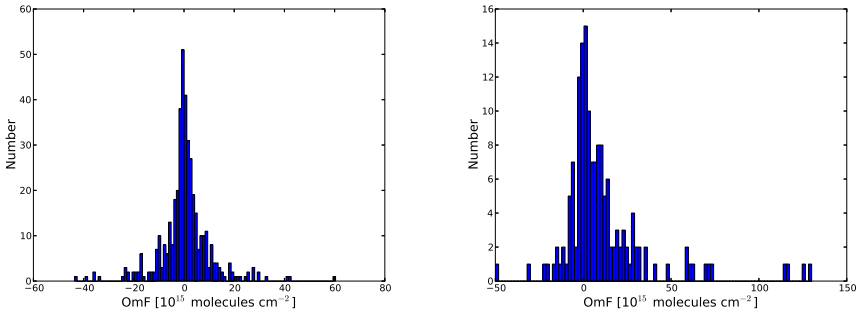

Figure 2.7: The distribution of the OmF values over 15 polluted cities in summer (left) and in winter (right). The 15 polluted cities are Baoding, Beijing, Chengdu, Harbin, Hohhot, Guangzhou, Jinan, Shanghai, Shenyang, Shijiazhuang, Tianjin, Wuhan, Xi'an, Xingtai and Zhengzhou.

also the average overpass time in Nanjing. Compared to the year 2013 the in situ measurements show no significant improvement in the surface NO_2 concentration at 13:00 LT for the period May to August, 2014 when the government took air quality regulations for the YOG. However, we see a high variability in the monthly averaged data, indicating that the data are strongly affected by highly variable local sources (e.g. local traffic) and weather. We also calculate the monthly average using all measurements and we still see a high variability in the time series. Because of the high variability in the ground data and its low representativity for the whole city of Nanjing, we discarded this data set in our analysis.

Figure 2.1 shows the land-use over Jiangsu Province. The rectangle referred to as the Nanjing area, covers the whole of Nanjing including all industrial areas along the Yangtze River. According to the MEIC sector distribution, the power plants in the selected area are dominating the NO_x emissions. To study the effects of the air quality regulations for the YOG on tropospheric NO_2 column concentrations, we compare the monthly averages of satellite observations over the Nanjing area for each year from 2005 to 2014 by regridding the observational data on the model grid over the area.

The satellite observations show that on average the NO_2 column concentrations are rather similar from year to year (Figure 2.9). Although a small increasing trend from 2005 to 2011 is visible in the satellite data, it is negligible compared to the SD of the natural variability. It is clear that the NO_2 columns have a seasonal cycle that is lower in summer than in winter due to the seasonal change of the NO_2 lifetime (van der A et al., 2006). Note that the small decrease in columns in February might be caused by the reduced emissions during the Spring Festival (Q. Zhang et al., 2009). The monthly averages of NO_2 in situ observations shown by Wang et al. (2011) for

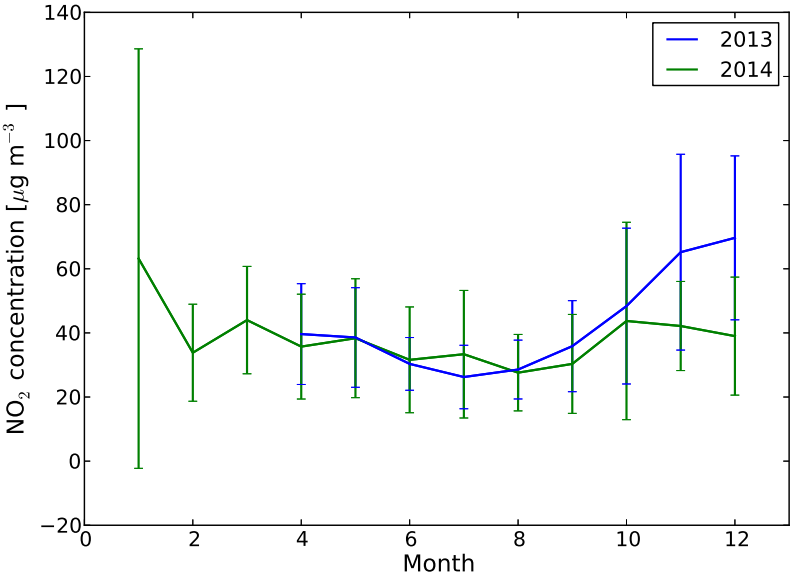

Figure 2.8: The monthly averaged in situ NO_2 concentration at 13 local time in Nanjing for 2013 and 2014.The bar is the standard deviation (natural variability) of the observations for each month (derived from the daily data on www.aqicn.org).

Beijing, Shanghai and Guangzhou in 2005 were also reduced by around 10 % in February. We see that the NO_2 column during the YOG period (August 2014) is on average only 6.6×10^{15} molecules cm^{-2}, which is the lowest value among the last 10 years and more than 3 standard deviations from the mean. Possibly due to the effect of the continuous air quality regulations for the YOG and afterwards, the NO_2 columns of the following months are also lower than for previous years. The more permanent measures (traffic-related) resulting from the YOG affect a small fraction of the total emissions. In November, the local government took similar air quality regulations for the first National Memorial ceremony held on 13 December, 2014. That might explain the lower NO_2 columns of the last 2 months of 2014 compared to those of 2013 and compared to the average of the last 8 years. However, it is still within the range of the standard deviation of NO_2 columns for the last 8 years. Differences from year to year can also be attributed to the meteorological conditions (Lin et al., 2011). Particularly in December 2013, NO_2 columns are very high. This episode is well known as a heavy smog period in Nanjing because stagnant air in the region accumulated anthropogenic pollution. Compared to the averaged NO_2 column in August from 2005 to 2012, the NO_2 column of August in 2014 is decreased by 32 % in Nanjing. However, this significant decrease can be caused by

the rainy weather during that month. Thus, NO_x emission estimates are needed to show if the air quality regulations were really effective. The emission estimates use not only satellite observations in the location of the YOG but use all observations over China that are transported to and from Nanjing. Besides transport of air, the meteorological effect on the lifetime of NO_2 is taken into account.

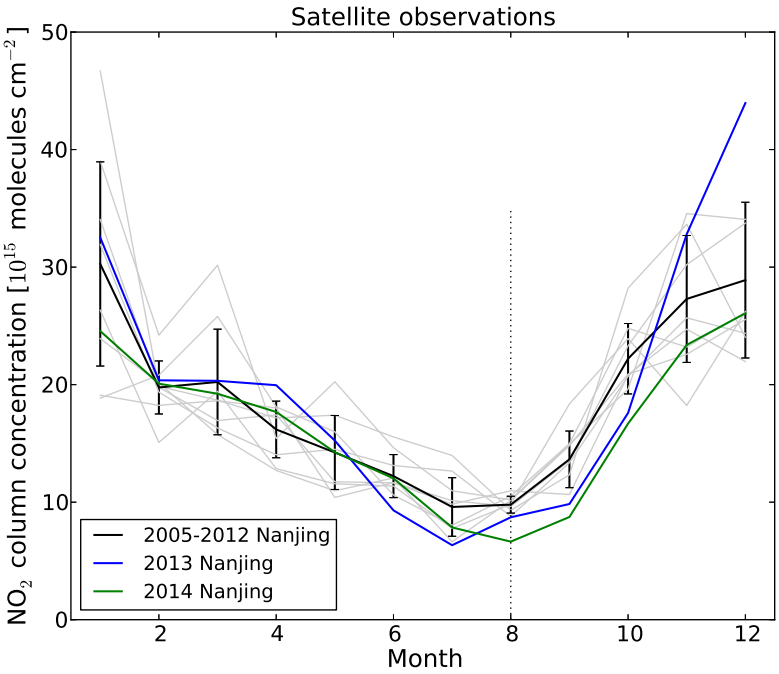

Figure 2.9: The monthly averages of OMI satellite observations of tropospheric NO_2 concentrations. The solid lines are the measurements over the Nanjing area. The grey lines are the monthly averages for each year from 2005 to 2012 to indicate the annual variability. The black lines show the average value for the years from 2005 to 2012. The bars are the standard eviations of monthly NO_2 observations from 2005 to 2012.

To compare the NO_x emissions in Nanjing in 2014, especially during the YOG, with the same period of the year 2013, we run DECSO v3b with the OmF criterion as described in Section 3.2 from October 2012 to December 2014, where the first 3 months are used as a spin-up period. Figure 2.10 shows the monthly NO_x emissions in Nanjing for the year 2013 and 2014 estimated by this version of DECSO. For comparison the initial MEIC inventory is also plotted in the figure. The NO_x emissions have a different seasonal cycle compared to the NO_2 columns of satellite observations in Nanjing. The months with high emissions are June and July while the highest NO_2 columns of the satellite observations appear in January and De-

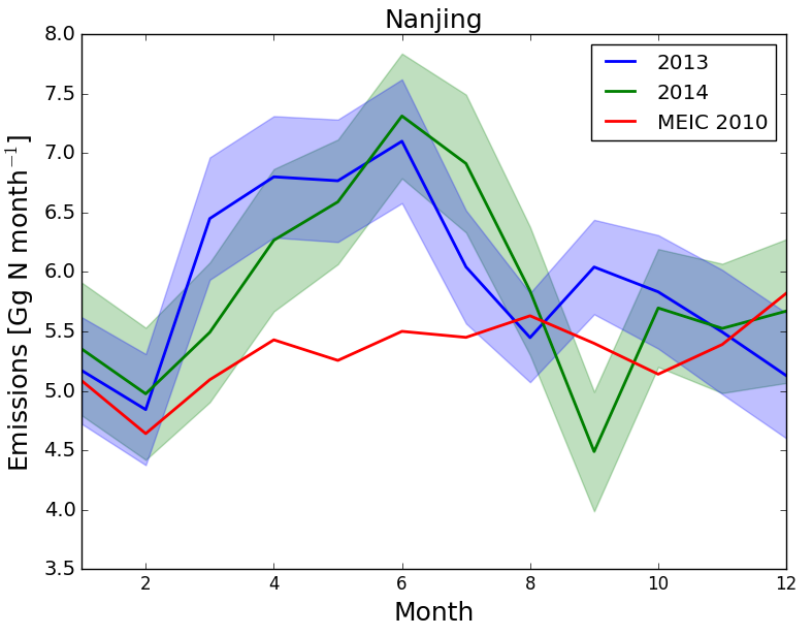

Figure 2.10: The monthly NO_x emission estimates by DECSO in Nanjing for 2013 (blue line) and 2014 (green line) and the monthly NO_x emission of the MEIC inventory of 2010 (red line). The shade areas show the error of the mean NO_x emission estimates from DECSO.

cember. According to the sector distribution in the MEIC inventory, the emissions of power plants and industrial activities are the main sources in Nanjing. At least 50 % of the total NO_x emissions are from power plants and 40 % are from the industrial activities. H. Zhang et al. (2009) showed that the seasonal cycle of the electricity consumption in Nanjing for the 7 years from 2000 to 2006 peaks in the summertime, because the electricity consumption and power load are highly correlated with temperature in summer. The value of electricity consumption in summer is at least two times higher than in winter every year and keeps increasing during those 7 years. The seasonality of electricity consumption is caused by the increasing usage of air conditioning in the hot season, while there is no heating system used in winter time in Nanjing. The opposite cycles of column concentrations (Figure 2.9) and emissions (Figure 2.10) show that the high NO_2 concentrations in winter in Nanjing are mainly affected by the long lifetime of NO_x, while the seasonal cycle of NO_x emissions is reversed as a result of the increased electricity consumption in summertime. The difference with the seasonal cycle of MEIC might be attributed to the fact that our results are derived on city-level, while the seasonal cycle for bottom-up inventories are often derived on a national or provincial scale (e.g. Q. Zhang et al., 2009). The

monthly average temperatures from June to September are above 20 degree. The monthly temperatures in 2014 did not deviate much from the climatological values.

We see a drop in NO_x emissions in February for both years calculated with DECSO, which is also visible in the MEIC inventory of 2010 (Figure 2.10). This jump is consistent with the decrease of NO_2 columns of the satellite observations in February compared to the neighboring months. Compared to the neighboring months, the NO_x emission reduction in February is about 10 % in 2013 and 2014. This NO_x emission decrease was also noticed by Q. Zhang et al. (2009) in the INTEX-B inventory and likely to be caused by the reduced industrial activities during the Spring Festival. Lin and McElroy (2011) also showed that the Spring Festival causes a reduction of about 10 % on NO_x due to the decrease of thermal power generation based on the analysis of several satellite observations. Interestingly, we do not see an increase of NO_x emissions in the December 2013 smog period. This shows that the smog is caused by the meteorological conditions rather than increased emissions.

Figure 2.10 shows a large reduction of NO_x emissions in September, 2014. The total NO_x emissions in September in Nanjing are 4.5 Gg N. Compared to the same time of the year 2013, the reduction is about 25 %. However, the emission reduction in this case seems to have a delay of 1 month. The shaded area in Figure 2.10 represents the error on the derived emissions without taking into account the error introduced by the Kalman Filter time lag. Reductions in emissions at the end of August or the following months can appear with a time lag in the Kalman filter results (see e.g Brunner et al., 2012). This time lag is not fixed but depends on the amount, interval, accuracy and distance of the observations and it is therefore difficult to quantify. In our case, this is partly a consequence of the use of monthly means, while the regulations became active at the end of August. It is also a consequence of the lack of satellite observations due to the rainy (and therefore cloudy) weather in the second half of August 2014 when the YOG took place. For these kind of conditions, DECSO only detects the full extent of the emission reduction in September. We also see a NO_x emission reduction of 10 % in August, 2013, compared to the neighboring months. One likely reason for this reduction is that the Asian Youth Games were held during that time. The local government also took measures to ensure good air quality for that event but they were not as strict as for the YOG in 2014. We conclude that the NO_x emission reduction detected by DECSO for the YOG period and afterwards was at least 25 %, showing that the air quality regulations taken by the local government were effective.

2.5. Discussion and conclusions

In this study the effect of the air quality regulations of the local government during the YOG in Nanjing in 2014 has been quantified by analyzing observations on the ground and from the satellite. The focus in this study was on the reduced NO_2 concentrations and NO_x emissions. We compared NO_2 during the YOG period with previous years using the in situ and the OMI satellite observations. The in situ observations have a large variability, even after averaging on a monthly basis. This is probably caused by the variability of local sources and it indicates that these in situ observations are not representative for the larger area of Nanjing. The in situ data show no significant decrease during the YOG period. Since we have no error estimates of the in situ observations and very little information on the instrument and measurement techniques we discard the results of the in-situ observations in our conclusions.

For the view from space we limited ourselves to retrievals of tropospheric NO_2 from OMI, taking advantage of the high spatial resolution of OMI observations compared to similar instruments. The monthly OMI satellite observations showed a 32 % decrease of the NO_2 column concentration during the YOG period in Nanjing compared to the average value for the last 10 years. However, the decrease of NO_2 columns observed by the satellite is not an objective measure to verify the impact of the air quality regulations taken by the local government, because changes in NO_2 columns can have more causes such as horizontal transport of NO_2 or increased wet deposition of the NO_2 reservoir gas NO_3 due to the rainy weather. Furthermore, due to cloudy conditions, the August average of 2014 is based on few observations. Therefore, it is important to analyze the emissions to show if the air quality regulations have really affected the NO_2 concentrations.

The results of our improved emission estimate algorithm DECSO show that NO_x emissions decreased by at least 25 % in September 2014, which shows that the air quality regulations were effective during the YOG period and that only a small part of the reduced NO_2 column concentrations were caused by the weather conditions. However, the reduction has a one month delay in our results. This is because satellite observations were scarce in the Nanjing area during the YOG (16 to 29 August) causing the DECSO algorithm to converge slower to the new emissions, which is typical for the Kalman filter approach used in DECSO. Although the strong point of Kalman Filter is its detailed error analysis, this time lag is not incorporated in its error formalism. In future research we intend to reduce this time lag by using a smoothing Kalman Filter technique.

We were able to see the emission reduction of NO_x in the selected six grid

cells representative for the Nanjing area. That means that DECSO is at least able to estimate NO_x emissions on a spatial resolution of about 50 km × 90 km. If we apply the same analysis on single grid cells the results are noisier because the footprint of the OMI covers on average a larger area than a single grid cell. To achieve emission estimates in a smaller area, either satellite observations with a higher spatial resolution are required or longer time periods should be considered.

The quality of our emission estimates is highly related to the quality of the model and the satellite observations. We improved the DECSO algorithm by using a new version of the CTM: CHIMERE v2013 instead of CHIMERE v2006. The comparison of OmF between two models showed that CHIMERE v2013 has a better performance in summertime. Good quality of satellite observations is also essential for emission estimates. The DOMINO retrieval algorithm does not properly account for the effects of high aerosol concentrations, which are common in China, on the retrieved NO_2 columns. In case of high aerosol concentrations, the difference between the model simulations and the retrievals is very large, which leads to wrong updates of NO_x emissions in DECSO. To improve the satellite observations we have set an OmF criterion to filter out erroneous observations and to avoid unrealistic NO_x emission updates. We set the limitation to the range -5×10^{15} molecules cm^{-2} to 10×10^{15} molecules cm^{-2} for the OmF. With this filter criterion, the unrealistic updates of NO_x emissions are mostly prevented. We will further analyze the impact of high aerosol concentrations on the retrieved NO_2 columns in future research.

Furthermore, we observed an opposite seasonal cycle of NO_x emissions compared to the NO_2 columns observed by OMI satellite. The seasonal cycle of NO_x emissions is not the same for the whole China domain since the different climate in the north and the south of China leads to a different seasonality of energy consumption during the year. In Nanjing, as in most parts of southern China, people use air conditioning in summer and do not use heating systems in winter. This leads to a larger electricity production of power plants in summer resulting in higher NO_x emissions. Tu et al. (2007) studied the air pollutants in Nanjing and also found high NO_2 columns in winter but concluded that the high NO_2 columns were caused by high NO_x emissions in winter, while our emission estimates show the opposite. Wang et al. (2007) analyzed the seasonality of NO_x emissions based on GOME satellite observations for the regions north and south of the Yangtze River, defined as north and south China. Their results of south China showed the same seasonal cycle of NO_2 columns but a very weak seasonality of NO_x emissions and they also concluded that the NO_x lifetime mainly determines the NO_2 columns. Ran et al. (2009) explained high NO_x concentrations in winter are caused by slower chemical processes and shallow boundary layers contributing to accumulation of NO_x. The table in Wang et al. (2012) of annual and summer NO_x emissions from

coal-fired power plants in 2005–2007 for different provinces in China showed that the NO_x emissions in Jiangsu Province in summer are higher than mean seasonal emissions.

In conclusion, we not only found a reversed seasonal cycle peaking in summertime in the emission estimates, but also indications for reduced emissions during the Spring Festival, the Asian Youth Games in 2013 and the YOG 2014. Based on our emission estimates the air quality regulation during the YOG 2014 and afterwards reduced the NO_x emissions by at least 25 percent. This, together with favorable meteorological conditions, was responsible for a decrease of 32 % in NO_2 column concentrations observed from space. For the case of the YOG, our results can help the local government to identify the impact of their air quality regulations on reducing NO_x emissions.

Acknowledgement

The research was part of the GlobEmission Project funded and supported by the European Space Agency. We acknowledge Tsinghua University for providing the MEIC inventory and the ESA GlobCover 2009 Project for the land use dataset. The MODIS images used in this study were acquired as part of the NASA's Earth-Sun System Division and archived and distributed by the MODIS Adaptive Processing System (MODAPS). The OMI is part of the NASA Earth Observing System (EOS) Aura satellite payload. The OMI project is managed by the Netherlands Space Office (NSO) and the Royal Netherlands Meteorological Institute (KNMI).

3

Space-based NO_x emission estimates over remote regions improved in DECSO

We improve the emission estimate algorithm DECSO (Daily Emission estimates Constrained by Satellite Observations) to better detect NO_x emissions over remote areas. The new version is referred to as DECSO v5. The error covariance of the sensitivity of NO_2 column observations to gridded NO_x emissions has been better characterized. This reduces the background noise of emission estimates by a factor of 10. An emission update constraint has been added to avoid unrealistic day-to-day fluctuations of emissions. We estimate total NO_x emissions, which include biogenic emissions that often drive the seasonal cycle of the NO_x emissions. We demonstrate the improvements implemented in DECSO v5 for the domain of East Asia in the year 2012 and 2013. The emissions derived by DECSO v5 are in good agreement with other inventories like MIX. In addition, the improved algorithm is able to better capture the seasonality of NO_x emissions and for the first time it reveals ship tracks near the Chinese coasts that are otherwise hidden by the outflow of NO_2 from the Chinese mainland. The precision of monthly emissions derived by DECSO v5 for each grid cell is about 20 %.

This chapter has been published in Atmospheric measurement techniques as Ding et al.(2017a).

3.1. Introduction

Nitrogen oxides ($NO + NO_2 = NO_x$) are important air pollutants and play a crucial role in climate change by catalysing the formation of tropospheric ozone and forming secondary nitrate aerosol (Shindell et al., 2009; IPCC, 2014). Anthropogenic emissions are the main source of NO_x. Better emission estimates may help policymakers to mitigate the adverse influence of those air pollutants. However, it is difficult to obtain up-to-date emission data. Bottom-up emission inventories rely on gathering statistical data, which is time consuming and often results in a delay of a few years. In addition, statistics on emission-related activities and emission factors introduce large uncertainties to the bottom-up emission inventories. Satellite observations provide long-term NO_2 column concentrations with a global coverage and they are able to improve NO_x emission estimates (Streets et al., 2013) . Emissions of dominant sources like megacities can be derived from satellite observations using a simple mass-balance approach (Martin et al., 2003) . Smaller sources, like biogenic emissions or ship tracks are more difficult to distinguish, especially if they are close to the dominant sources. These lower NO_x emissions are derived from satellite observations with inversion techniques, taking into account the transport of NO_x (e.g Stavrakou et al., 2008; Miyazaki et al., 2012).

Mijling and van der A (2012) developed the inversion algorithm DECSO (Daily Emission estimates Constraint by Satellite Observation) based on an extended Kalman filter with a regional chemical transport model (CTM). This algorithm takes the transport of NO_x from its source into account by including 2-D trajectory analysis in the sensitivity of NO_2 concentration on NO_x emissions. Other NOx emission studies based on a Kalman filter often use the decoupled direct method to calculate the sensitivity (Napelenok et al., 2008; Tang et al., 2013) or an ensemble Kalman filter (Miyazaki et al., 2012). The emission estimates of DECSO improve upon existing emission inventories in the Middle East and South Africa (www.globemission.eu). The DECSO algorithm has the capability to show trends and seasonality on a provincial scale for China and the derived emissions are in good agreement with the bottom-up inventories in Asia (Mijling et al., 2013). Ding et al. (2015) improved the algorithm performance by updating the CTM and adding a satellite data quality control. The improved temporal and spatial resolution enables detection, e.g. of the NO_x reductions during the Nanjing Youth Olympic games in August 2014.

Estimating emissions from satellite data is relatively new, and many developments are ongoing in this field. General weak issues in inventories are their low temporal resolution and the lack of information for small sources in remote areas. The seasonal variability is normally poorly captured in emission inventories.

Mijling and van der A (2012) showed that DECSO is able to detect the shipping emissions along the Chinese coastal seas, which are not included in the anthropogenic emission inventories INTEX-B (Q. Zhang et al., 2009) and MIX (Li et al., 2017; http://www.meicmodel.org). However, Ding et al. (2015) mentioned that emissions from DECSO have also large day-to-day fluctuations due to the noise in the observations. In remote ocean areas where emissions should be close to zero, we still see relatively high emissions, which we refer to as background noise. This background noise is appearing in low-emission areas, where random negative emissions derived from the measurements are set to zero because the CTM cannot handle negative emissions. This results in, on average, a positively biased emission for this region. This background noise can have an unrealistic seasonal cycle. Because of this background noise, weaker emission sources, such as shipping emissions or small isolated power plants are difficult to distinguish. A new version of DECSO, referred to as DECSO v5, has been developed with special attention for those issues. The improvement in observing low emissions will be demonstrated for two cases. One case is for biogenic sources and fire emissions in rural areas, which are relatively weak over often-large areas. The second case is for shipping emissions close to the coast, where low emissions exist in proximity to large sources of cities along the coast. Both emission sources have large uncertainties in existing inventories.

Estimates of biogenic emissions contain large uncertainties. In regions where fire emissions from forests and biomass burning are dominant, the seasonal cycle of NO_x is not the same every year, since burnt areas are changing from year to year due to human activities (Schultz et al., 2008) and climate (Westerling et al., 2006). Van der Werf et al. (2006) showed that the seasonality of fire emissions varied a lot from 1997 to 2004 in central Asia. He et al. (2011) studied biomass emissions in the Pearl River Delta region by using a bottom-up approach and showed that the uncertainties of NO_x biomass burning emissions vary from 80 to 220 %.

Recent studies point out that ship emissions of NO_x make a significant contribution to the total NO_x budget. The global shipping emission inventories have large differences and high uncertainties from the statistical sampling of ship tracks and the simplified parameterizations used in shipping emission calculations (Wang et al., 2008). Shipping emissions, e.g. in the Indian Ocean, the Red Sea and the European seas are detected by SCIAMACHY, GOME, GOME-2 and OMI satellite observations (Beirle et al., 2004; Richter et al., 2004; Franke et al., 2009; Vinken et al., 2014). Richter et al. (2004) mentioned that the signal of ship tracks towards China and Japan is lost in the transported NO_2 plume from the sources over land, so that it is difficult to estimate emissions by using the mass-balance approach. By using the improvements of DECSO described in this paper, we will show that DECSO is able

to provide NO_x shipping emission estimates near the coast of China and detect the seasonality of NO_x emissions related to biogenic sources.

To improve the issues mentioned above, here we focus on the performance of the DECSO algorithm over low-strength emission regions. We improve the error covariances of the sensitivity of NO_2 column observations to gridded NO_x emissions. Adding an emission update constraint instead of using the satellite data quality control mentioned in Ding et al. (2015) removes the unrealistic fluctuations of emissions. As a consequence, we use more information from the satellite observations. With the updates applied to DECSO, the algorithm is better able to detect shipping emissions and other small sources and shows a more realistic seasonal cycle, especially over the low emission areas. In addition, we switch off the biogenic NO_x emissions in the CTM to calculate total NO_x emissions instead of only anthropogenic emissions. In Section 3.2, we briefly describe the DECSO algorithm. The improvements are presented in Section 3.3. We have applied the DECSO algorithm to the region of eastern China and for this area the improvements will be demonstrated. Monthly variability of emissions in different areas of East Asia and the shipping emissions over the China coastal region are shown in Section 3.4, followed by a discussion of the results in Section 3.5.

3.2. Emission estimates with the DECSO algorithm

DECSO is an emission estimate algorithm for short-lived trace gases, which updates daily emissions on a mesoscopic scale with a spatial resolution of $0.25^\circ \times 0.25^\circ$. It constrains NO_x emissions by combining the simulated NO_2 concentrations of a CTM with satellite observations. The essential part of DECSO is the calculation of the sensitivity of the NO_2 column concentrations (on a footprint of the satellite) to the gridded NO_x emissions, in which the transport of NO_2 over the model domain is taken into account. The transport is calculated using an ensemble of 150 isotopic 2-D trajectories for each grid cell. For the trajectory analysis, we use the operational meteorological forecast of the European Centre for Medium-Range Weather Forecasts (ECWMF) interpolated into half an hour time steps. The inversion method used in DECSO is based on an extended Kalman filter. The emissions and their error covariance derived from DECSO are independent of the a prior emission inventory after a spin-up time of about 3 months. Note that the assimilation with observations based on Kalman filter leads to the "true" emission estimates with a typical time lag (Brunner et al., 2012; Ding et al., 2015). Although the emissions are calculated on a daily basis, the final product of DECSO is a monthly emission database similar as

for bottom-up inventories.

We use the Eulerian offline CTM CHIMERE v2013 (Menut et al., 2013) in DECSO. To run a simulation of CHIMERE, external forcings like meteorological fields, primary pollutant emissions and chemical boundary conditions are required. We have implemented CHIMERE on a $0.25^\circ \times 0.25^\circ$ horizontal resolution over the regions of Europe, Middle East, South Africa, India and East Asia with eight vertical layers up to 500 hPa. The model is driven by the operational meteorological forecast of the ECWMF. The land use information we use for CHIMERE is from the GlobCover Land Cover database in 2009.

The satellite observations in this study are measured by the Dutch–Finnish Ozone Monitoring Instrument (OMI; Levelt et al., 2006) on NASA's EOS-Aura satellite. The spatial resolution is 24 km $\times$ 13 km at nadir and increases to about 150 km $\times$ 28 km at the edge of the swath. Its overpass time at the equator is around 13:30 local time. We use the tropospheric NO_2 column data of the Dutch OMI NO_2 retrieval (DOMINO) algorithm version 2 (Boersma et al., 2011). The data set can be found on the Tropospheric Emissions Monitoring Internet Service (TEMIS) portal (http://www.temis.nl). We use the same data filter criteria for the DOMINO v2 data as mentioned in Ding et al. (2015). The pixels affected by the so-called row anomaly (KNMI, 2012) and the four pixels at each side of the swath are filtered out. We use observations with a surface albedo lower than 20 % and a cloud radiance fraction lower than 70 %. The observations with clouds below 800 hPa are also excluded, because cloudy and bright surface scenes have a large influence on the quality of the retrieval product. After this filtering, we typically have about 2000 observations per day for each domain.

To compare the simulated concentrations from CHIMERE with satellite observed tropospheric columns, the modelled vertical profiles are extended from 500 hPa to the tropopause with a climatological partial column (2003 – 2008 average) simulated by the global CTM TM5 with a horizontal resolution of $2^\circ \times 3^\circ$ (Huijnen et al., 2010). We spatially average the simulated profiles on the model grid cell over the OMI footprints and apply the averaging kernel to the modelled profile. A more detailed description of DECSO can be found in Mijling and van der A (2012) and Ding et al. (2015).

3.3. Improvement of DECSO

3.3.1. Observation and representativeness error calculation

The inversion in DECSO is based on the extended Kalman filter, which assimilates emissions using a CTM to relate the emissions to daily observed concentrations. The analysis of the emission $\mathbf{e}^a$ is calculated from the observed NO_2 column concentrations $\mathbf{y}$ at time t and the forecasted emission $\mathbf{e}^f$ at time t using equation:

$$\mathbf{e}^a(t) = \mathbf{e}^f(t) + \mathbf{K}(\mathbf{y} - H\left[\mathbf{e}^f(t)\right]), \tag{3.1}$$

in which $\mathbf{K}$ is the Kalman gain matrix, and H is the observation operator (translating emissions into column concentrations) which includes the CTM, the extension of the simulated column to the tropopause, the average kernel from the satellite retrieval, and the interpolation to the satellite footprint. $\mathbf{e}^f(t)$ is equal to the analysis of the emissions from the previous day, following a persistent emission model. The Kalman gain matrix $\mathbf{K}$ combines error covariances of observations, model representation and emissions to determine how much information from the observations is to be used in the emission analysis:

$$\mathbf{K} = \mathbf{P}^f(t)\,\mathbf{H}[\mathbf{H}\mathbf{P}^f(t)\,\mathbf{H}^T + \mathbf{R}]^{-1}. \tag{3.2}$$

$\mathbf{P}^f$ is the error covariance matrix of the forecasted emissions. $\mathbf{H}$ is the sensitivity matrix (Jacobian) describing how the NO_2 column concentrations on a satellite footprint depend on gridded NO_x emissions, i.e. having matrix elements $H_{ij} = \frac{\partial y_i}{\partial e_j}$. Typical dimensions of $\mathbf{H}$ are about 2500 (daily observations) × 16 000 (emission grid cells).

$\mathbf{R}$ is the error covariance associated with observation operator H. The $\mathbf{R}$ matrix combines the observation error of the tropospheric NO_2 columns and the representation error introduced by the inaccuracy of the CTM and its projection onto the measured NO_2 column on the satellite footprint. $\mathbf{R}$ cannot be calculated directly, but we can derive its diagonal elements with help from the statistics of the Observation minus Forecast (OmF) of the NO_2 columns:

$$\sigma^2_{OmF} = \sigma^2_R + \sigma^2_{prem} = \sigma^2_{obs} + \sigma^2_{repr} + \sigma^2_{prem}. \tag{3.3}$$

The OmF variance consists of the variance of the $\mathbf{R}$ matrix (σ^2_R; consisting of the observation error σ^2_{obs} from the retrieval method and the representation error σ^2_{repr}) and the variance of the emission estimates propagated into the simulated col-

umn concentrations (σ^2_{prem}). σ^2_{prem} is taken from the diagonal elements of matrix $\mathbf{HP}^f(t)\mathbf{H}^T$.

In the previous versions of DECSO, the representation errors were calculated based on daily statistics of OmF since σ^2_{obs} and σ^2_{prem} are known. The observation errors were initially taken from the observations and later described by an empirical exponential relation with the observed column in version 3 (Ding et al., 2015). Mijling and van der A (2012) assumed that σ_{repr} is linearly related to the simulated tropospheric column concentration, and derived this ratio from daily OmF statistics. However, from day to day the number of observations varies a lot due to variability in cloudiness and scenes of observations (e.g. ocean vs. populated land). In days with few observations, the statistics are insufficient to derive the proper representation errors. This results in a lot of unrealistic day-to-day variations in σ_{repr}. In addition, because the observation coverage is smaller in wintertime than in summertime, the representation error is determined to be less accurate in winter due to the lack of statistics. Since emission updates (by Equation 3.1) are sensitive to the derived **R** matrix (used in Equation 3.2), this may lead to artificial seasonal fluctuations. We noticed that the average of **R** matrix elements is higher in winter than in summer, leading to biased emissions in summertime.

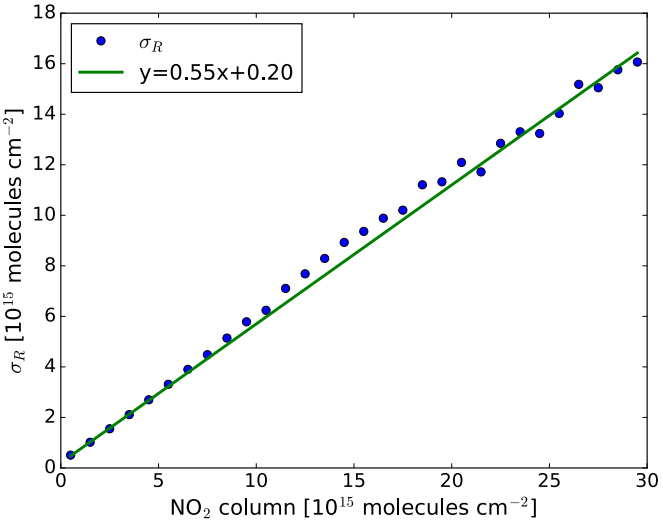

Figure 3.1: The relation between σ_R and the average of the observed and modelled NO_2 column. The green line is the fit result.

To improve this issue, we study the OmF statistics for monthly and yearly periods and directly relate σ^2_R to the NO_2 column instead of calculating the σ^2_{obs} and σ^2_{repr}

separately. We run DECSO over East Asia (18–50° N and 102–132° E) for 2013.

By binning the data in intervals of 1×10^{15} molecules cm^{-2} over the range of NO_2 column values, we use the OmF statistics and Equation 3.3 to derive σ_R per bin. For all observations 2013 we plot σ_R against the average c of observed and modelled NO_2 column and find a linear relation (see Figure 3.1):

$$\sigma_R = \varepsilon_{rel} c + \varepsilon_{abs}, \tag{3.4}$$

with relative coefficient $\varepsilon_{rel} = 0.55$ and absolute offset $\varepsilon_{abs} = 0.20$. Using data from other periods we found that this relation has very little variation from month to month and from year to year. Ding et al. (2015) used tuned synthetic error estimates for the satellite observations instead of the errors given by the retrievals. Tuning the error estimates of the satellite observations, as done for DECSO v3b, is no longer needed.

We apply this new linear relation in DECSO-exp. Figure 3.2 shows the comparison of yearly average emissions over the ocean for DECSO-exp and DECSO v3b. We see that the noise over remote areas is significantly reduced. The shipping emissions are smaller in DECSO-exp, but they are still clearly visible against the lower background values. The analysis of shipping emissions will be further discussed in Section 3.4. The monthly emissions in 2013 over a selected remote ocean area (20 to 25° N, 125 to 130° E) derived using DECSO-exp are much lower than DECSO v3b (Figure 3.3). We see the emissions derived by DECSO v3b vary from 4 to 10 Gg N month^{-1} with a summer peak. These emissions are too high for this area and the seasonal cycle is artificial. Since shipping emissions are the only emission source of NO_x in this part of the ocean where few ships are passing, the emissions over this area should be close to zero. The emissions derived by DECSO-exp are 10 times lower in summer compared to the emissions of DECSO v3b. The artificial seasonality also disappeared, since the higher values of DECSO-exp in April, May and December are within the range of emission uncertainties. By using the linear relation of σ_R with the NO_2 column, the calculation of σ_R is simplified, the background noise is reduced by 90 %, from about 16.7 Mg month per grid cell to about 1.7 Mg month per grid cell, and the artificial seasonal cycle has been removed over low emission areas.

3.3.2. Emission update constraint

Occasionally large differences between observed and modelled NO_2 columns appear, which are probably related to wrong satellite retrievals during high aerosol events (Ding et al., 2015). Several studies pointed out that the DOMINO retrieval

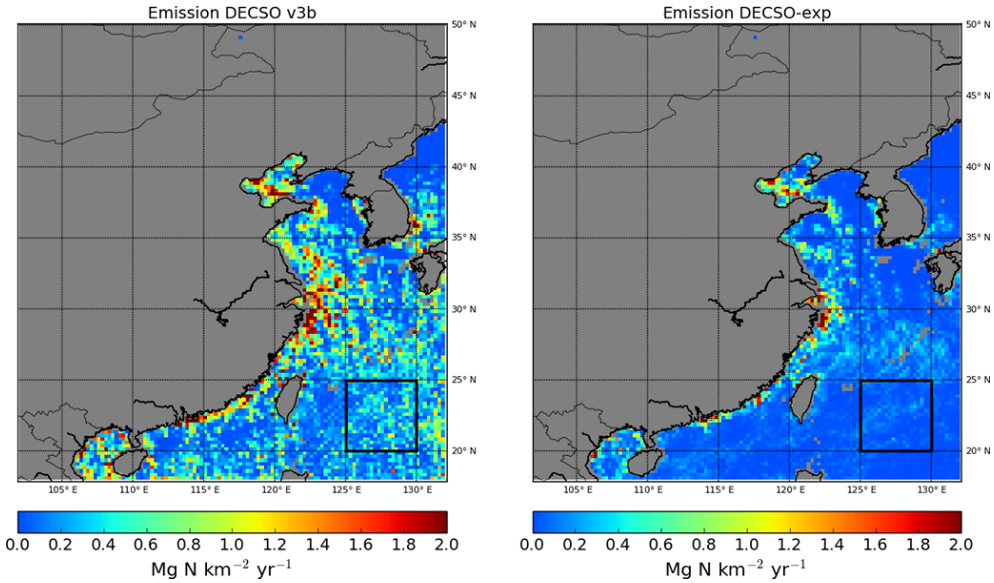

Figure 3.2: The comparison of NO_x emissions over the ocean derived with DECSO v3b (left) and DECSO-exp (right).

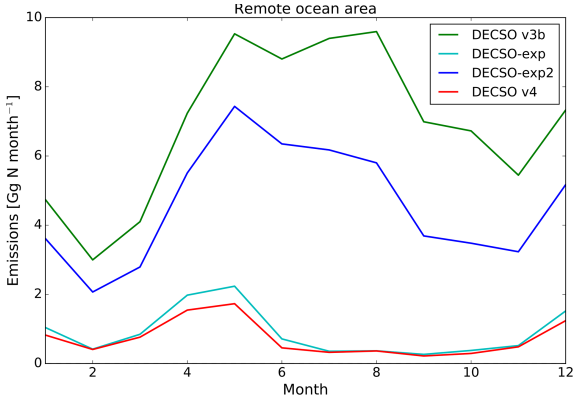

Figure 3.3: The total monthly NO_x emissions over a remote ocean area [20 ° N, to 25° N, 125 ° E to 130° E] derived with DECSO v3b, DECSO-exp, DECSO-exp2 and DECSO v4.

algorithm does not properly take the effects of high aerosol concentration into account (Leitão et al., 2010; Lin et al., 2014). To reduce false emission updates due to day-to-day fluctuations, Ding et al. (2015) used an OmF criterion to filter out satellite data that show large differences compared to the model simulations caused by these high aerosol events. Although filtering out these satellite data solves the problem, it may also delete correct satellite data. For example, if a new power plant

is built or an old one is removed, it can cause large changes of NO_2 concentrations in a single day. This is not simulated correctly by the CTM. With the OmF criteria, the emission updates will be unnecessarily slow since a lot of satellite data with large differences will not be used in the data assimilation. As we describe below, we improve the DECSO algorithm by using an emission update constraint to avoid unrealistically high fluctuations in the emission estimates.

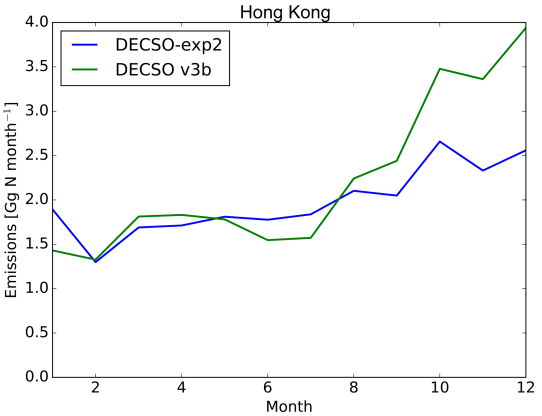

Figure 3.4: The monthly emissions in Hong Kong in 2013. DECSO-exp2 indicates the emissions derived using DECSO with the 3σ constraint. DECSO v3b indicates the emissions derived with the OmF filter.

In the DECSO algorithm, we use a persistent emission model, which assumes that the forecasted emissions of the current day are equal to the analysis of the emissions of the previous day, $\mathbf{e}^f(t) = \mathbf{e}^a(t-1)$. Assuming an optimal Kalman filter, the error of these emissions should have a Gaussian distribution, thus with 99.7 % of emissions within the range of 3σ from the mean. Therefore, we will use a 3σ interval to constrain the emission updates instead of the OmF criterion. To be able to handle both wrong observations, e.g. due to high aerosol load as well as new emission sources, we apply the following procedure during the data assimilation process: in case the emission update is larger than 3σ, we regard it outside the emission range and set the emission update equal to 3σ.

We run DECSO with this 3σ constraint for 2013 to test this new procedure, which is referred to as DECSO-exp2. With the new constraint, we use 10 % more satellite observations. Figure 3.4 shows that with the 3σ emission update constraint, the emission in Hong Kong is almost constant for the whole year with a small increase in winter. The emissions of DECSO v3b, however, are much higher (a factor of 2) in December than in January, which does not seem realistic since the vehicle emissions are the main source in Hong Kong and the seasonality is obscure (Kwok et al., 2010). Over the ocean, the fluctuation of emissions becomes smaller with

the new improvement compared to DECSO v3b (Figure 3.3). Note that the **R** matrix improvement is not applied in this run and therefore the improvement is only caused by the 3σ constraint, which can also be seen in Figure 3.3. With DECSO v4, the improvements on **R** matrix and the 3σ constraint are combined. The monthly emission data over East Asia of this version are available on www.globemission.eu.

3.3.3. Logarithm of emission

Negative emission estimates in DECSO are set to zero, because the CTM is not able to handle negative emissions. As a workaround, negative emissions are set to zero while the positive emissions in the nearby area are adjusted to compensate for the introduced bias. To make sure that the emission estimates remain positive, Brunner et al. (2012) replaced the emission state vector by its logarithmic value, assuming that the errors of this new state are Gaussian distributed. The assumption is not entirely correct in our case, but it is still a reasonable approximation.

To assess the effect of this approach in our setting, we define the logarithmic emissions ($\mathbf{x} = \ln(\mathbf{e})$) as the state vector in the Kalman filter. As a consequence, the observation operator H (see Equation 3.1) needs to be reformed. H^l is the sensitivity calculator describing how the NO_2 column concentrations **C** depend on logarithmic emissions **x**:

$$\mathbf{C} = H^l(\mathbf{x}) = H(\exp(\mathbf{x})). \tag{3.5}$$

In the Kalman filter, each element H^l_{ij} of Jacobian matrix $\mathbf{H}^l$ of the new observation operator can be easily derived as shown by Brunner et al. (2012):

$$H^l_{ij} = H_{ij}\exp(x_j) \equiv H_{ij}e_j. \tag{3.6}$$

In addition to the Jacobian, we need the error covariance of the modelled logarithmic emissions. Based on the derivative of the logarithmic value of the emission with respect to the emission itself,

$$\frac{dx}{de} = \frac{1}{e}, \tag{3.7}$$

the logarithmic emission error q^l can be expressed as follows:

$$q^l = \frac{q}{e}, \tag{3.8}$$

where q is the error of the modelled emissions. Mijling and van der A (2012) gave an assumption for the dependence of the emission error q on the emissions e:

$$q = \varepsilon_{abs}\exp\left(-\frac{\varepsilon_{rel}}{\varepsilon_{abs}}e\right) + \varepsilon_{rel}e. \tag{3.9}$$

ε_{abs} (0.02×10^{15} molecule cm^{-2} h^{-1}) and ε_{rel} (0.05) are the absolute and relative errors that are the dominating emission errors for low and high emissions respectively. By combining Equations 3.8 and 3.9, we get the error for the logarithmic emissions. However, if the emissions are close to zero, the error will become infinite, leading to computational errors. To avoid this, we define a new equation for q^l to calculate the emission error, which leads to similar emission errors as in previous DECSO versions and avoids infinite error values:

$$q^l = \alpha_1 \exp\left(-\frac{\alpha_1}{\alpha_2}x\right) + \alpha_2. \tag{3.10}$$

By setting $\alpha_1 = 0.009$ and $\alpha_2 = 0.02$, the emission error $q = q^l e$ is in good agreement with the original q calculated in Equation 3.9.

Using the new observation operator and the logarithmic emission error, we implement the logarithmic method based on DECSO v4 and run it for 2013, which is referred to as DECSO v4log. However, the results of this logarithmic method are not improved compared to DECSO v4. Instead, it increases the positive bias over low emission areas by a factor of 2. Also, the spin-up time is increased for low emission areas, which means it cannot detect the emission changes on a small temporal scale. Since the improvements by using the new **R** matrix and 3σ constraint for emission updates already reduce the background noise and remove the artificial seasonal cycle, we decide not to use the logarithmic approach in this study.

3.3.4. The threshold of the sensitivity matrix and the effect of biogenic NO_x emissions

A well-defined sensitivity matrix **H** (see Equation 3.2) is essential for a well-performing Kalman filter. As described by Mijling and van der A (2012), the calculation of **H** involves simplified 2-D trajectories to describe the transport of the concentration plumes over the emission grid. In some cases the bulk of the plume is shielded by clouds and the satellite only monitors a fraction of the plume at its edge. The edge of the plume is usually characterized by low sensitivity matrix **H** elements resulting from trajectory calculations with a high uncertainty. The inversion becomes ill-conditioned, resulting in strongly fluctuating emission updates with high associated uncertainties. These emission updates are based on limited information from the satellite. Therefore we have set a minimum value for the **H** matrix elements. In the previous versions of DECSO, we used 0.05 h as the minimum value. This value is still too low for the scarce winter observations at high latitudes leading to large biases, especially in these locations. In this study we set the threshold value to 0.1 h based on several tests using different threshold

values.

In DECSO v3b and v4, the derived NO_x emissions represent anthropogenic emissions. Biogenic emissions are generated internally in CHIMERE v2013 following a parameterization (including land-use data) by the MEGAN model (Guenther et al., 2006). However, Li et al. (2007) showed that emission factors of soil NO emissions in the same type of forests can differ a lot. This introduces large uncertainties in estimated biogenic emissions. Figure 3.5 shows the ratio of biogenic NO emissions from MEGAN and anthropogenic NO_x emissions from MIX. Biogenic emissions are about 5 % of total anthropogenic emissions in rural provinces in summer. Unfortunately overestimation of the MEGAN biogenic emissions in those rural areas can introduce biases in the local anthropogenic NO_x emission estimates by DECSO. For instance, in case MEGAN biogenic NO_x emissions are overestimated, the NO_x emissions derived by DECSO will be negative. As we mentioned in Section 3.3.1, DECSO sets negative emissions to zero and adjusts positive emissions in the surrounding area for compensation and mass balance.

By excluding biogenic NO_x emissions in CHIMERE, we derive the total surface NO_x emissions from satellite observations. The total emissions from the surface include anthropogenic, biogenic and fire emissions. Together with the improvement of **R** matrix, the 3σ constraint and the new threshold of the **H** matrix elements, this new DECSO algorithm is referred to as DECSO v5 (the monthly emission results calculated with this version are also provided on www.globemission.eu). The main differences of the various versions of DECSO mentioned in this paper are summarized in Table 3.1.

Table 3.1: Summary of main differences in various versions of DECSO.

DECSO version	Description
v3b	The base version described in Ding et al. (2015)
exp	Experimental version with improvement of the **R** matrix
exp2	Experimental version with improvement of the 3σ constraint
v4	Combined the improvements in exp and exp2
v4log	Logarithmic version of v4
v5	Estimate total emissions instead of only anthropogenic emissions

3.4. Results

We run DECSO v5 for the period 2012 to 2014 over East Asia. The final results are monthly emissions for this period, which means that irregular emissions and emissions for short time periods (for example from fires or lightning) are typically averaged over a month. As we showed in Section 3.3, the improvements in DECSO reduce the background noise and remove artificial season cycles over low-emission areas. Due to this, it will enable better emission estimates over low emission regions like ship tracks in the ocean, small cities in deserts, grassland, etc. Below we demonstrate the improvements in the emission estimates for these specific cases.

3.4.1. Seasonal cycle analysis

One way to validate the improvement of emission data derived by DECSO v5 is by comparing the forecast results of the CHIMERE model used in DECSO v5 and DECSO v3b with OMI satellite observations over the model domain. We compared the average of NO_2 column per season per grid cell over the whole domain. The comparison shows that the improvement of DECSO v5 in wintertime (December to February) is significant. The modelled NO_2 columns of DECSO v5 are in much better agreement with OMI satellite observations in winter with a correlation coefficient (R) of 0.96, while R is only 0.87 for DECSO v3b. Yearly averages and the other seasonal averages of NO_2 columns of both versions are in good agreement with OMI satellite observations, especially in summer. The R in summer of both versions is 0.97. The better agreement of DECSO v5 modelled columns with OMI satellite observations in wintertime results in a better seasonal cycle of emission estimates.

We compare the seasonal cycle of NO_x emissions on a provincial level in 2012 with the MIX emission inventory of 2012 (the latest year available in MIX) over China and MIX emission inventory (Li et al., 2017) outside of China. We find that in many provinces the seasonal cycles derived by DECSO are consistent with the MIX inventory. However, in most rural provinces, the difference between DECSO v5 and MIX is very large. Based on the ratio of biogenic emissions of MEGAN and anthropogenic emissions of the MIX inventory shown in Figure 3.5, we divide provinces in China into two groups. We select a group of 13 provinces with large areas of relatively high biogenic emissions as rural provinces. The remaining 16 provinces in the domain are considered anthropogenic emission provinces. The R (correlation coefficient) of seasonal emissions for anthropogenic emission provinces between DECSO v5 and MIX 2012 is 0.6, while for rural provinces the comparison is much worse (R is negative in most rural provinces) because MIX does not include biogenic NO_x emissions.

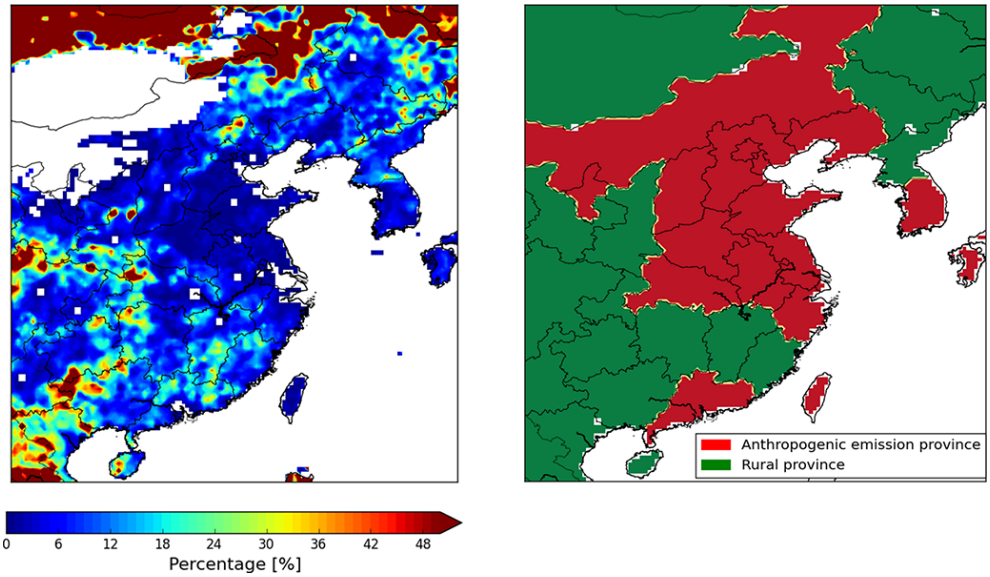

Figure 3.5: Ratio between biogenic and anthropogenic NO_x emissions in summer (left) and the distribution of anthropogenic emission provinces and rural provinces (right). Biogenic emissions are from the MEGAN model used in CHIMERE. Anthropogenic emissions are from the MIX (2012) emission inventory.

Figure 3.6 shows the seasonal cycle of two provinces as an example. Guangxi province is a typical rural province in China. About 60 % of the province is covered by forest (www.forestry.gov.cn), which is about 14×10^5 km^2. Both DECSO v5 and v3b show high emissions from spring to summer. The NO_x emissions estimated by DECSO v3b are only anthropogenic because biogenic emissions from MEGAN are calculated internally by the CTM. As we mentioned in Section 3.3, DECSO v3b has a high background noise with an unrealistic seasonal cycle, which explains the difference with DECSO v5. We calculate that in the Guangxi province, the background noise of DECSO v3b contributes to a maximum of about 6 in winter and 17 Gg month^{-1} in summer. By removing the background from DECSO v3b, the summer peak of emissions disappears. We see that monthly NO_x emissions from March to September derived by DECSO v5 are much higher than the emissions of MIX in 2012. The difference is probably due to biogenic emissions since MIX only includes anthropogenic emissions. DECSO v5 estimates include both anthropogenic and biogenic emissions. In summer, the emissions derived by DECSO v5 are about 50 % higher than in MIX. In Figure 3.5, we see that the biogenic emissions are 7–8 % of anthropogenic emissions in summer based on the information given by MEGAN. However, the uncertainties of biogenic emissions derived by MEGAN are at least 300 % (Guenther et al., 2006, 2012). Li et al. (2007) listed soil NO emission rates from different forests in the world including their results of broadleaf and pine

forests in southern China. By using their range of emission rates, we calculate the soil NO emissions in Guangxi in a range from 30 to 822 Gg N yr^{-1} by multiplication with the forest area, the upper limit being 3.5 times higher than the yearly total NO_x emissions derived by DECSO v5. This shows that the uncertainty in biogenic emissions from bottom-up emissions is quite high. DECSO v5 provides independent information about total surface NO_x emissions in the region since it is difficult to distinguish source types of the emissions.

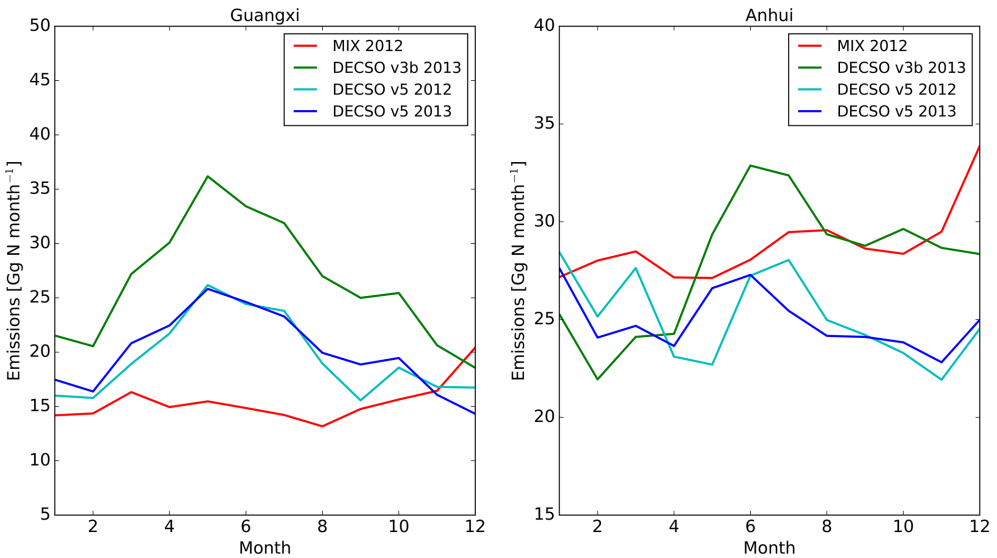

Figure 3.6: Monthly total emissions estimated by DECSO v5 (blue line) and DECSO v3b (green line) of Guangxi province (left) and Anhui province (right) in 2013. The cyan line and the red line represent monthly NO_x emissions from DECSO v5 and the MIX inventory in 2012.

Anhui province is an example of an anthropogenic emission province. In this province NO_x emissions derived by DECSO v5 are lower than MIX 2012. The peak that appears in March 2012 of DECOS v5 is probably due to high soil NO_x emissions which are not included in MIX. Jaegle et al. (2005) concluded that global soil NO_x emissions can be as high as 20 % of the total NO_x emissions. Many studies demonstrate that both the usage of fertilizer and the increase of rainfall lead to significantly higher soil emissions (Bouwman et al., 2002; Jaeglé et al., 2004; Ghude et al., 2010; Cui et al., 2012). Liu et al. (2015) showed that lots of areas are overfertilized in Anhui. The climate annual report of Anhui (http://www.ahqh.org.cn/product/yearqhmonitor.asp) shows that in March 2012 the precipitation is 50 % higher than normal for the month, and from May to July the province had a drought. This leads to the small peak of 10 % higher NO_x emissions in March 2012. DECSO v5 also shows a peak of NO_x emissions in June 2013, which

can be explained by the biomass burning in this month. The Globe Fire Emission Database (GFED) 4.0 (Giglio et al., 2013) shows large biomass burning areas in Anhui in May and June of 2013. Huang et al. (2012) pointed out that Anhui is one of the provinces with the highest agricultural fire emissions, with a peak in June. Stavrakou et al. (2016) conclude that the current estimates of agricultural fire emissions of post-harvest crop burning are much too low in China. These fires usually appear around the month of June, for which DECSO also shows higher emissions in Figure 3.6.

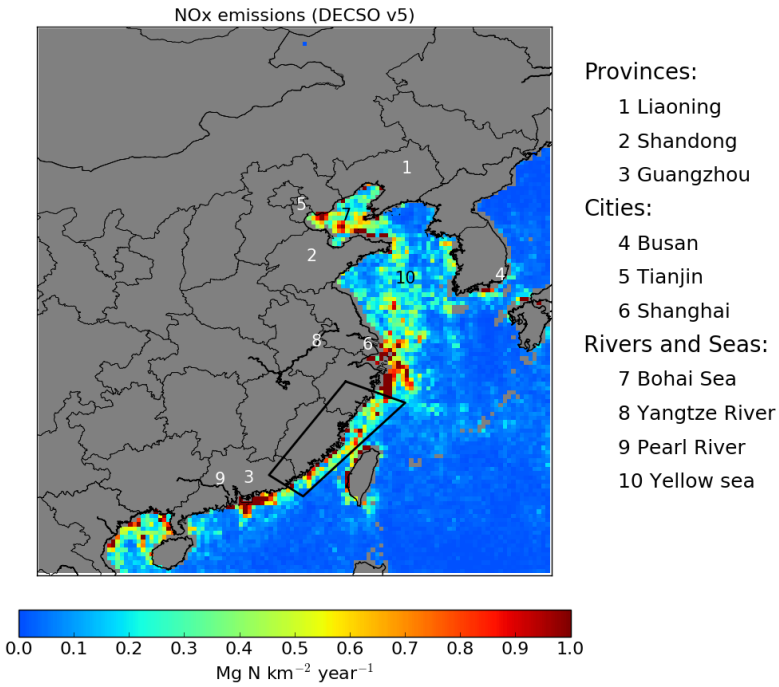

Figure 3.7: Emission estimates derived with DECSO v5 over the ocean in 2013. The black quadrangle indicates the selected area for analysing shipping emissions in the Taiwan Strait.

3.4.2. Ship track emissions near the Chinese coast

Figure 3.7 shows the yearly average emissions over the ocean in 2013 as derived with DECSO v5. We filter out the grid cells including any part of the land because we cannot distinguish shipping emissions from land-based emissions. We see a clear ship track near the coastal area from Guangzhou to Shanghai, which disperses in the Yellow Sea. Two high emission areas are at the edge of the Yangtze and Pearl River. In the Bohai Sea, at the coast of Shandong and Liaoning province,

the emissions become stronger where ships are more concentrated on the route to and from Tianjin. A strong emission area appears at the coast of South Korea around the port of Pusan. Figure 3.8 shows the ship locations for 1 day based on Automatic Identification system (AIS) signals, the worldwide ship position monitor system (www.shipfinder.com). Most of the ships are located close to the coast with a clear ship lane from Guangzhou to Shanghai, while ships become sparser in the Yellow Sea. We see a good correlation of the high ship densities and the high emission areas derived by DECSO v5 shown in Figure 3.7. Many of the ship locations in Figure 3.8 are close to the coast or on inland water and therefore are not visible in Figure 3.7.

We select the Taiwan Strait area within the black rectangular shown in Figure 3.7 to analyse the dependence of emissions on the distance to the coast. The total emissions for the selected area are about 49 Gg N yr^{-1} in DECSO v5 and 92 Gg N yr^{-1} in DECSO v3b. Figure 3.9 shows two peaks of the ship emissions in DECSO v5 as a function of the distance from the coast. The maximum emissions are close to the coast within the territorial waters of 24 nautical miles (44 km). The ships along the coastline contribute the most to the emissions. The second peak of emissions is shown at a distance of about 90 km from the coast. As this distance we often find cargo ships on long distance routes from and to Shanghai or Tianjin. Note that the calculated background noise (emissions in the remote area as defined in Section 3.3) is much lower than the ship emissions shown here. The background noise of DECSO v5, indicated by the dashed blue line, is as low as 0.017 Gg N per year per grid cell. The ship emissions derived by DECSO v3b show a similar pattern, but the values are two times higher due to the high background emissions (0.2 Gg N per year per grid cell).

When zooming in on Figure 3.8 (see the website http://www.shipfinder.com/), we distinguish two ship tracks in the selected area, which are also noticed by Liu et al. (2016). One is within the territorial waters from 20 to 44 km from the coast, which we refer to as the territorial shipping. The other is within a distance of 44 to 160 km, which is referred to as the long distance shipping lane. Since it is the first time that the ship emissions near the Chinese coast are derived by satellite observations, we have no reference for the same area. However, because of the dispersion of international shipping routes into several branches, it is expected that emissions in our long distance shipping lane will be less than in the dense ship tracks between India and Singapore and in the Red Sea that have been studied by other authors. By dividing by the 800 km length of the ship lane, the emissions are about 0.025 Gg N km^{-1} yr^{-1} in DECSO v5. Beirle et al. (2004) estimated that the ship emissions from Sri Lanka to Indonesia were about 10 to 73 Gg N yr^{-1} (0.005 to 0.038 Gg N km^{-1} yr^{-1}) from 1996 to 2001. For the same area but from 2002 to

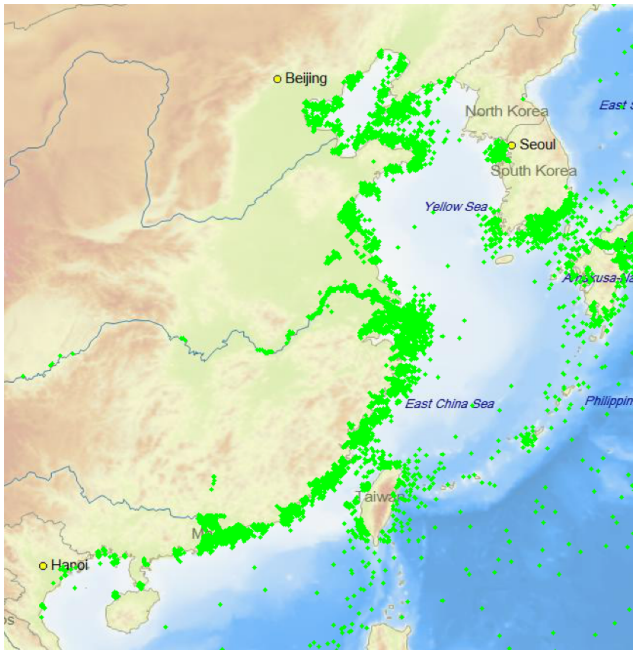

Figure 3.8: Ship locations at 5 November 2015 from Automatic Identification System (AIS) information (taken from http://www.shipfinder.com/).

2007, Franke et al. (2009) estimated the ship emissions were about 90 Gg N yr^{-1} (0.047 Gg N km^{-1} yr^{-1}). Based on the study of Richter et al. (2004), the ship emissions for the Red Sea area are about 0.03 Gg N km^{-1} yr^{-1} from 2002 to 2004. The magnitude of the shipping emissions over a long distance shipping lane derived by DECSO v5 seems to be in agreement with these studies. The emissions derived from DECSO v5 in the Chinese territorial waters are much higher than for the long distance shipping, which seems a good reflection of the much higher density of ships in these waters.

3.5. Discussions and conclusions

We have improved the DECSO algorithm to calculate better emission estimates over remote emission regions. DECSO v5 estimates total NO_x emissions instead of anthropogenic emissions to avoid the bias introduced by the uncertainties of biogenic emissions by MEGAN in the low emission areas. With a more solid approach of calculating error covariances of the sensitivity of NO_2 column observations to gridded NO_x emissions, DECSO removes the artificial seasonality that is caused by

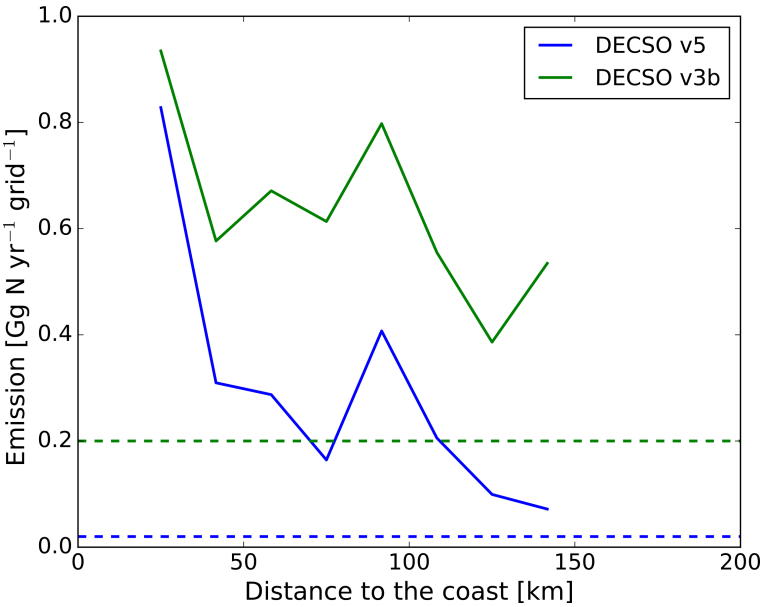

Figure 3.9: The relation between NO_x emissions over the ocean and the distance to the coastline in the Taiwan Strait (the quadrilateral area in Figure 3.7). The blue dashed line is the background noise in DECSO v5 and the green dashed line in DECSO v3b.

daily calculation of error covariances. The background noise has been reduced in the new version with a factor of 10 to a level of less than 0.02 Gg N yr^{-1} cell^{-1} and a rms (root mean square) error of 0.036 Gg N yr^{-1} cell^{-1}. Using the emission update constraint instead of an OmF filter enables DECSO to use 10 % more observations and removes unrealistic emission fluctuations found in DECSO v3b. By changing the threshold value of the sensitivity matrix **H**, the errors caused by few observations on the edge of the emission plumes have been decreased.

Direct validation of emission estimates is not possible due to the lack of independent observations. The accuracy of the emission estimates depends largely on the accuracy of the NO_2 satellite observations and of the CTM used in the inversion. Any random errors in the observations or the model are described in the Kalman filter and result in an error estimate for the emissions. Biases are more difficult to quantify. A negative or positive bias in the CTM can occur due to the influence of its limited resolution on NO_2-OH chemical feedbacks, which varies over different cities and time periods due to the size of the emission source (Valin et al., 2011). Random CTM errors are included in the calculation of the representation errors described in Section 3.3.1. Any systematic biases in the CTM (for example caused by non-linear chemistry in relation to the coarse resolution) will directly af-

fect the resulting emission estimate. In DECSO, the grid NO_2 columns simulated by the CTM are projected via a high-resolution grid onto the footprint of satellite observations, which avoids the bias caused by different resolutions of the CTM and satellite observations. The NO_2 observations can suffer from biases in scenes with high aerosol concentrations (Lin et al., 2014; Kuhlmann et al., 2015; Chimot et al., 2016) or the limited resolution of the a priori information used in the retrieval cases with high NO_2 concentration gradients (Heckel et al., 2011; Russell et al., 2011; Laughner et al., 2016). In China, however, there are few isolated emission sources with large concentration gradients. Therefore, several validation studies of the DOMINO v2 product with MAX-DOAS measurements show no significant biases in China on average (Irie et al., 2012; Wang et al., 2016). Ma et al. (2013) evaluated a gradient smoothing effect in the DOMINO v2 retrieval product in China and found no significant bias in winter and an upper limit for the bias in summer of 11–26 %. Large biases coming from, for example, the high aerosol cases are avoided by the emission update constraint explained in Section 3.3.2. However, we can roughly estimate the precision of the emission based on the year-to-year variability in the derived monthly emissions per grid cell in 2012 and 2013, since there is no significant trend in these two years (van der A et al., 2017). We calculate the average difference in monthly emissions between 2012 and 2013 over all grid cells (15 609 grid cells), which is about 20 %. We verify the result by comparing the derived monthly emissions for 2012 from DECSO with a run with a different initial emission inventory and starting year. We conclude that the precision is about 20 % for each grid cell. We do the same calculations on a provincial level and find that the provincial monthly emissions have much better precision of less than 2 %.

With all improvements implemented in DECSO v5, it shows good agreement with the MIX inventory in the spatial distribution. Figure 3.10 shows an overview of NO_x emission flux of each province from DECSO v5 and MIX in 2012. In some rural provinces (e.g. Guangxi, Yunan), NO_x emissions of DECSO are about 30 % higher than MIX. This is probably due to biogenic emissions that are not included in MIX. The NO_x emissions in Guangxi are much higher than MIX in summer. NO_x emissions of DECSO v5 are on average 30 % lower than MIX and go up to 80 % lower in most of the northern provinces of China. One possible reason for the low emissions in northern China is the underestimation of NO_2 tropospheric columns of DOMINO v2 specifically for that area of the world. We find a significantly high number of negative retrievals over this area in the winter months, which indicates a negative bias in the retrievals. This is partly due to a bias in the high air mass factor for retrievals at large solar zenith angles, introduced by the multiple scattering in the radiance transfer model used in the calculation of the air mass factor in DOMINO (Lorente et al., 2017). Another reason for the underestimation of emissions can

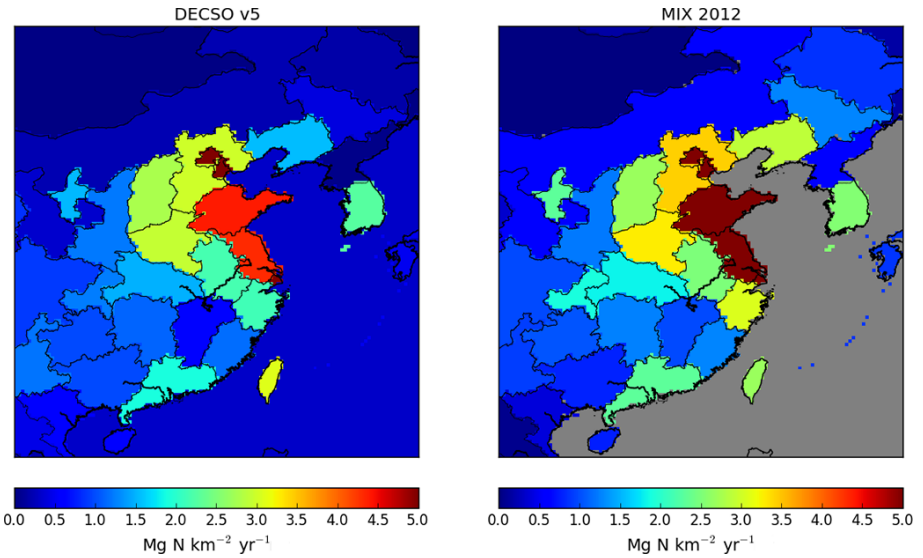

Figure 3.10: Annual emissions on a provincial level derived with DECSO v5 and from the MIX (2012) inventory, used for China and outside China respectively. Emissions over sea are not included in the MIX inventory.

be the uncertainties of NO_x sinks in the CTM used by DECSO for high latitudes. Stavrakou et al. (2013) showed that their NO_x emission results are about 20 to 50 % lower than MIX and they demonstrated the strong influence of NO_x loss uncertainties on top-down emission estimates. Mijling et al. (2013) discussed that the total anthropogenic NO_x emissions in eastern China from different inventories have a large range, which can be as large as 40 %. Except for the three northernmost provinces, the difference between DECSO v5 and MIX is within this range.

The relatively high R of 0.6 of seasonal emissions in anthropogenic emission provinces between DECSO v5 and MIX shows that DECSO v5 is able to capture the seasonality of NO_x emissions. However, the seasonality is not only dominated by anthropogenic emissions; biogenic emissions such as soil and fire emissions also have a large impact on the seasonality of emissions. Tie et al. (2006) showed that the total biogenic NO emissions in China are 50 % of total anthropogenic emissions and mostly from agricultural soils and synchronized with large populations and human activity. Meanwhile agricultural fire emissions from crop burning after harvest activity are also quite high. NO_x emissions of Anhui in 2012 and 2013 derived by DECSO v5 show small peaks in different months and this may be caused by high soil and fire emissions in those months.

By reducing the background noise in DECSO, we see more clear ship tracks near

the Chinese coastal areas, consistent with the ship locations. DECSO v5 reveals two shipping lanes in the Taiwan Strait: the territorial water shipping and the long distance shipping lane. The magnitude of the shipping emissions of the long distance shipping lane derived by DECSO v5 is comparable with other studies on shipping emissions derived from satellite observations in other areas of the world with similar ship density. The emissions in territorial water closer to the coast are much higher, which is also shown by Fan et al. (2016). Shipping emissions from DECSO v5 can be further studied for seasonality and yearly trends and also for other parts of the seas near China.

In summary, DECSO v5 derives the total NO_x emissions over East Asia with a very low background noise and reduces the artificial seasonal cycle over low emission regions compared to the previous versions. The seasonality of total emissions in DECSO v5 is more realistic and it gives comprehensive information of emissions in East Asia. The emissions and their seasonality over remote areas like seas, deserts and grasslands are as easily derived as emissions over populated areas and can be updated on a regular basis. Combining the sector information of bottom-up inventories with the emissions calculated by DECSO, more accurate and timely inventories can be provided for the modelling community.

Acknowledgements

The research was part of the GlobEmission project funded and supported by the European Space Agency. We acknowledge Tsinghua University for providing the MIX emission inventory. We acknowledge IPSL/LMD, INERIS and IPSL/LISA in France for providing the CHIMERE model. We acknowledge the use of tropospheric NO_2 column data of DOMINO version 2 obtained from www.temis.nl.

4

Maritime NO_x emissions over Chinese seas derived from satellite observations

By applying an inversion algorithm on satellite observations from OMI (Ozone Monitoring Instrument), monthly NO_x emissions for a 10-year period (2007 to 2016) over Chinese seas are presented for the first time. No effective regulations on NO_x emissions have been implemented for ships in China, which is reflected in the trend analysis of maritime emissions. The maritime emissions display a continuous increase rate of about 20 % per year until 2012 and slow down to about 3 % afterwards. The seasonal cycle of shipping emissions has regional variations but all regions show lower emissions during winter. Simulations by an atmospheric chemistry transport model show a notable influence of maritime emissions on air pollution over coastal areas, especially in summer. The satellite-derived spatial distribution and the magnitude of maritime emissions over Chinese seas are in good agreement with bottom-up studies based on the Automatic Identification System of ships.

This chapter has been submitted to Geophysical Research Letters.

4.1. Introduction

NO_x (NO_x=NO_2+NO) emissions from ocean-going ships contribute more than 10 % of the total anthropogenic NO_x emissions worldwide (Corbett et al., 1999, 2003; IMO, 2015). They have a large impact on the atmospheric chemistry and air quality in the marine boundary layer, and consequently have an impact on climate change (Lawrence and Crutzen, 1999; Eyring et al., 2010) and human health (H. Liu et al., 2016). Furthermore, the aerosol particles from ships may affect the maritime deep convection. This could lead to enhanced lightning, and therefore additional NO_x formation over shipping lanes (Thornton et al., 2017). Maritime transport emissions have large uncertainties due to the difficulty in determining shipping activities and emission factors. Satellite observations of NO_2 provide the possibility to detect ship tracks and estimate emissions. Beirle et al. (2004) showed the first detection of NO_x ship emissions derived by satellite observations of GOME over the Indian ocean by fitting the observations with a Gaussian function. Richter et al. (2004) found a clear NO_2 signal over the Red Sea and the Indian Ocean using the observations from the SCIAMACHY instrument. Furthermore, the combination of satellite observations with modelled columns of a chemical transport model (CTM) can be used to evaluate NO_x emissions in ship tracks. This was for instance used by Franke et al. (2009) to estimate the total NO_x emissions along the ship track from Sri Lanka to Indonesia. By using a mass-balance approach applied to the high spatial resolution measurements from the Ozone Monitoring Instrument (OMI) (Levelt et al., 2006), Vinken et al. (2014) derived shipping emission estimates over parts of the European seas. However, all mentioned methods are only applicable for specific ship tracks far away from sources over land. Near Chinese coastal areas the ship tracks are hidden in the outflow of NO_2 plumes from the mainland (see Figure 4.1(a)), which renders NO_x emissions from shipping activities difficult to detect from space. Traditional ship inventories are often lacking information on these ship activities or have large uncertainties on their ship emissions (C. Wang et al., 2008; Y. Zhang et al., 2017). Ding et al. (2017) showed clear satellite-derived NO_x emissions near Chinese coastal areas by using the inversion algorithm DECSO (Daily Emission estimates Constrained from Satellite Observations) combining CTM simulations and OMI satellite observations.

In the last decade, seaborne trade increased rapidly in East Asia. The number of studies of shipping emissions on a regional scale in East Asia is limited and most of them are at port or city level (Y. Zhang et al., 2017). The application of the data from the Automatic Identification System (AIS) significantly reduced uncertainties in bottom-up shipping emission inventories (Jalkanen et al., 2009). Fan et al. (2016) built a AIS-based model to calculate high-resolution shipping emissions of 2010 in

the sea around the Chinese Yangtze River Delta and parts of the East China Sea. Using a similar method, H. Liu et al. (2016) estimated that shipping emissions in East Asia accounted 16 % of the global shipping emissions in 2013. They also found that shipping emissions of NO_x in this region almost doubled compared to in 2001.

Based on the long-term record of NO_2 satellite observations from OMI, this study presents maritime NO_x emissions from 2007 to 2016 over the Chinese seas using DECSO. The long and consistent data series allows us to analyse the seasonal cycle and the trend of maritime NO_x emissions over Chinese seas. Since few air quality regulations on NO_x have been implemented for maritime transport in China, a persistent increase in shipping emissions is expected following the trend in cargo trade volumes. The effect of maritime emissions on NO_2 concentrations in coastal cities are investigated by using a regional CTM. To validate the results, the emissions are compared with the latest bottom-up ship emission inventory based on AIS data derived with the Ship Traffic Emission Assessment Model (STEAM) (Jalkanen et al., 2016).

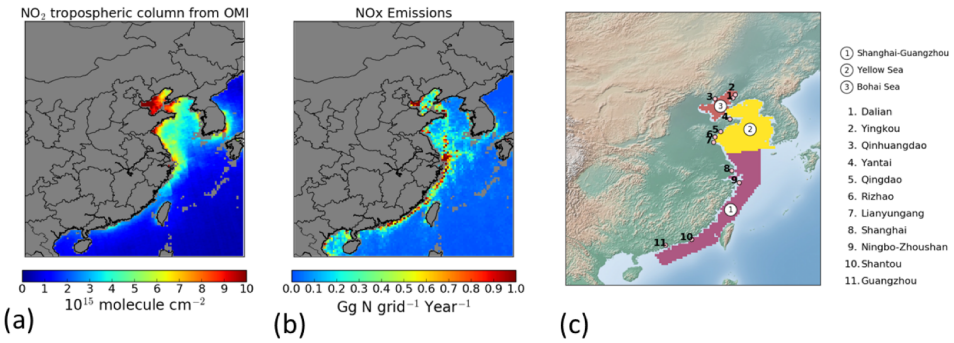

Figure 4.1: The average of (a) tropospheric NO_2 column concentrations over ocean observed by OMI from 2007 to 2016 and (b) NO_x emissions over ocean derived by DECSO applied to these OMI observations. (c) The three selected regions to study the shipping emissions near the Chinese coast are shown as colored areas. The numbers in the circle indicate the name of the regions. The numbers on the coasts indicate the locations of the main harbours.

4.2. Emission estimates

DECSO is a fast inverse modelling algorithm developed by Mijling and van der A (2012) to calculate daily emissions of NO_x based on an extended Kalman Filter. The algorithm combines simulated NO_2 column concentrations of a regional CTM with satellite observations. The sensitivity of NO_2 column concentrations on local and non-local NO_x emissions is calculated by including a simplified isobaric surface

2-D trajectory analysis. The improvements in the latest version of DECSO (referred to as DECSO v5) by Ding et al. (2017) enabled the detection of ship tracks near the Chinese coasts by significantly reducing the background noise of estimated NO_x emissions over remote areas.

We derived NO_x emissions over Chinese seas in the domain of East Asia (102–132° E, 18–50° N) with a horizontal resolution of 0.25° × 0.25° from 2007 to 2016 by using DECSO v5. The Eulerian regional off-line CTM CHIMERE v2013 (Menut et al., 2013) is used to simulate NO_2 concentrations. Its implementation in DECSO is described in Ding et al. (2015). The a priori emission field over the ocean is set to zero. We set the injection height of newly-found emissions over oceans at 40 m, representing an average funnel height for ships. We apply DECSO to observations from OMI due to its high spatial resolution, which is 24 km × 13 km at nadir and increases to 150 km × 28 km at the end of the swath. The tropospheric NO_2 column data of the DOMINO version 2 algorithm (Boersma et al., 2011) are used for the assimilation. To ensure retrievals in good quality, we use the filter criteria described by Ding et al. (2015, 2017) on the retrievals. In addition, to detect clear ship tracks, we exclude the observations with a large pixel size by filtering out 8 pixels at each side of the swath. The observations with a cloud radiance fraction larger than 50 % are excluded.

We use monthly NO_x emissions for our analysis. To calculate the uncertainty of monthly emissions in each region, we use the daily error estimate on each grid cell from the Kalman filter, which propagates errors from observations and the model. We assume the error of each grid cell has high temporal (day to day) correlation (up to 90 %) but low spatial correlation with an upper limit of 20 % with the 8 neighbouring grid cells.

4.3. Results

Figure 4.1(b) shows the average annual NO_x emissions from 2007 to 2016 derived with DECSO v5 over the Chinese seas. We see a clear ship track along the coast between Shanghai and Guangzhou. Over the Yellow Sea, high shipping emissions are revealed near Jiangsu province. A track from Shanghai to Yantai disperses in the Bohai Sea. We see high maritime emissions over the Bohai Sea and around the ports of Shanghai and Guangzhou. Half of the Chinese offshore platforms are located in the Bohai Sea. Over remote ocean areas, NO_x emissions are much lower and no notable shipping tracks are visible due to the low density of shipping activities, as confirmed by real-time shipping locations from AIS. Most shipping activities occur close to the coastal areas. Ding et al. (2017) depicted the shipping emissions

derived with DECSO near the coastline and concluded that their spatial distribution is consistent with the density of shipping activities. In this thesis, we analyze the seasonal cycle and trends of maritime emissions resulting from ships and offshore platforms in this area. We classify three regions shown in Figure 4.1(c), to study the evolution of shipping emissions near the Chinese coast.

4.3.1. Seasonal cycle

In Figure 4.2, we plot the month with the maximum monthly NO_x emissions for each grid cell over the ocean together with the seasonal cycle over each region. The upper limit of the relative error of the 10-year averaged monthly emissions per region is estimated to be about 20 %. A clear pattern of the maximum month distribution is shown over the Chinese seas. This means that the seasonal cycles of the shipping emissions have regional variation. We see that shipping emissions reach a maximum in May over southern Chinese seas, which is earlier than for the northern seas. More northwards, over the Yellow Sea and the Bohai Sea, the monthly shipping emissions gradually reach their maximum later. The earlier maximum month in the southern region can be explained by the start of summer monsoon in mid-May, which moves steadily northwards over East China (Burke and Stott, 2017). J. Wang et al. (2014) showed that the monsoonal climate and tropical cyclones decrease the safety for ships in the South China Sea, which results in fewer ships after May. Beside the influence of weather, the different summer moratorium of fishing in these areas is possibly another reason for the difference in the peak month of emissions. Over the Yellow Sea, shipping emissions increase in summer, which might be explained by the increase of tourism activities, while the shipping emissions reach their peak in September, because more fishing ships are expected in this month after the lifting of the summer moratorium in this area (Shen and Heino, 2014). Over the Bohai Sea and the Yellow Sea especially, the shipping activities decrease in winter due to sea ice and bad weather and start to increase again in April (L. Wang et al., 2013; F. Zhang et al., 2014).

4.3.2. Trend analysis

Figure 4.3(a) shows the linear change rate of shipping emissions in each grid cell from 2007 to 2016. We see a clear increasing trend at the track along the southern coast from Guangzhou to Shanghai and continuing to Shandong Province in the Yellow Sea with an average increase rate of about 0.1 Gg N per grid cell per year. Figure 4.4 shows the annual shipping emissions with an estimated uncertainty of about ±20 % for each of the selected three regions. The upper line is the sum of

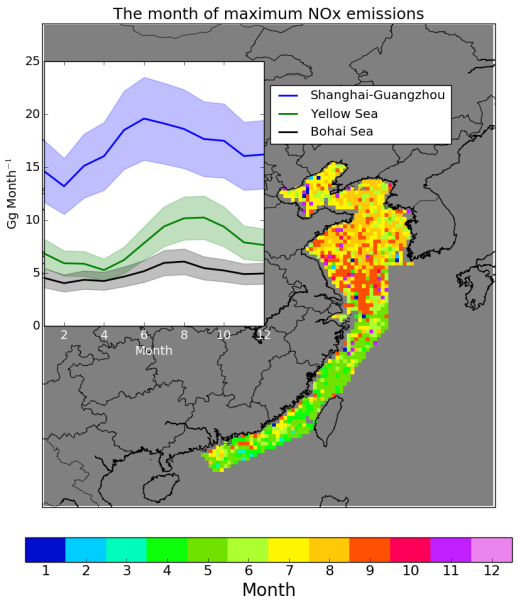

Figure 4.2: The month with the maximum monthly NO_x emissions for each grid cell over the ocean. The inset figure is the seasonal cycle of NO_x emissions for the selected three areas shown in Figure 4.1(c). The shaded bands in the inset figure indicates uncertainty.

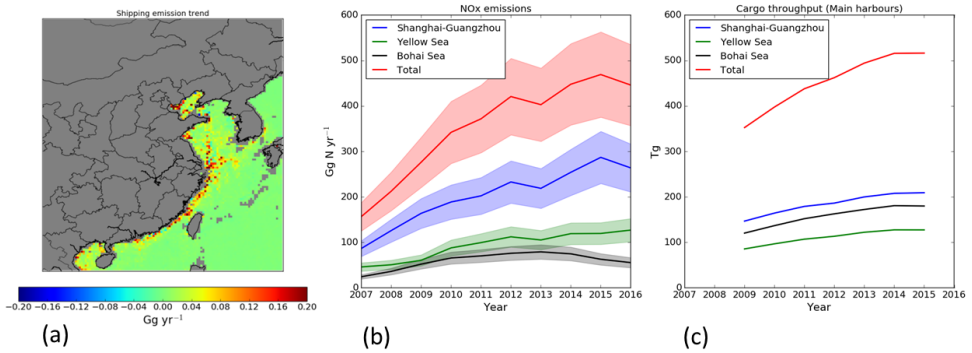

Figure 4.3: (a) The linear change rate of NO_x emissions per grid cell over the ocean from 2007 to 2016. The time series of (b) NO_x emissions from 2007 to 2016 and (c) cargo throughput volumes from main harbours from 2009 to 2015 over the selected three regions shown in Figure 4.1(c). The shaded bands in (b) indicate the uncertainty.

the three regions. We see that the relative increase rate levels off progressively, from about 30 % per year in 2007 to a very small trend in the last years. We have

currently no explanation for the decrease in 2013 and 2016. This decrease is not significant given the uncertainty of about 10 %. This is quite different compared to the trend of NO_x emissions and columns over Mainland China, where the NO_x emissions started to decrease since 2012 (F. Liu et al., 2016; van der A et al., 2017).

To rationalize the trend shown in Figure 4.3(b), we obtained the annual cargo throughput data of the main harbours (shown in Figure 4.1(c)) along the coast for the period of 2009 to 2015 from the National Bureau of Statistics China (NBSC, 2017). Cargo throughput volumes are commonly regarded as an indicator for shipping emissions (Streets et al., 1997) and used to compare with trends (de Ruyter de Wildt et al., 2012). Note that this does not account for fishing ships, recreational ships and for the size of cargo ships. Figure 4.3(c) shows the total volume of cargo throughput increased between 2009 and 2014 after which it remained at the same level. The trend is similar to that of shipping emissions shown in Figure 4.3(b). The ports along the Bohai Sea, Yellow Sea and the region from Shanghai to Guangzhou are summed up separately to approximate the shipping activity for these three regions. Note that ships delivering their cargo in ports of one region (especially Bohai) often also pass the other regions. For the Yellow Sea, this explains the lower cargo throughput compared to the higher NO_x emissions. The correlation coefficient (R) of the time series between shipping emissions and cargo throughput volumes are all above 0.95, for the Yellow sea, Shanghai-Guangzhou and the total of three regions, except for the Bohai Sea, which has an R-value of 0.84. We see that the annual emissions over the Bohai Sea show a decrease starting in 2014, while the cargo throughput volume becomes stable. Note that the emissions derived with DECSO are the total surface emissions. Over the Bohai Sea, the total NO_x emissions include the emissions not only from ships but also from several oil platforms in this region (Xing et al., 2015). In 2014, oil companies and the government signed the document "Responsibility for the total emission reduction targets" (Ren and Jin, 2014), in which the companies promise to reduce air pollutants from marine oil platforms. This might explain the decrease of emissions over the Bohai Sea after 2014. For all three regions, we see that the increase rate of emissions is higher than that of cargo throughput. This implies that regulations on NO_x emissions are either inexistent or ineffective for the maritime sector over open seas.

4.3.3. Contribution of shipping emissions to NO_2 air pollution

Shipping emissions near coastal areas amount to about 10 % of the total emissions over the mainland in our study domain. To study the influence of shipping emissions on shore regions, we set up two CHIMERE runs for the year 2015: one run using the

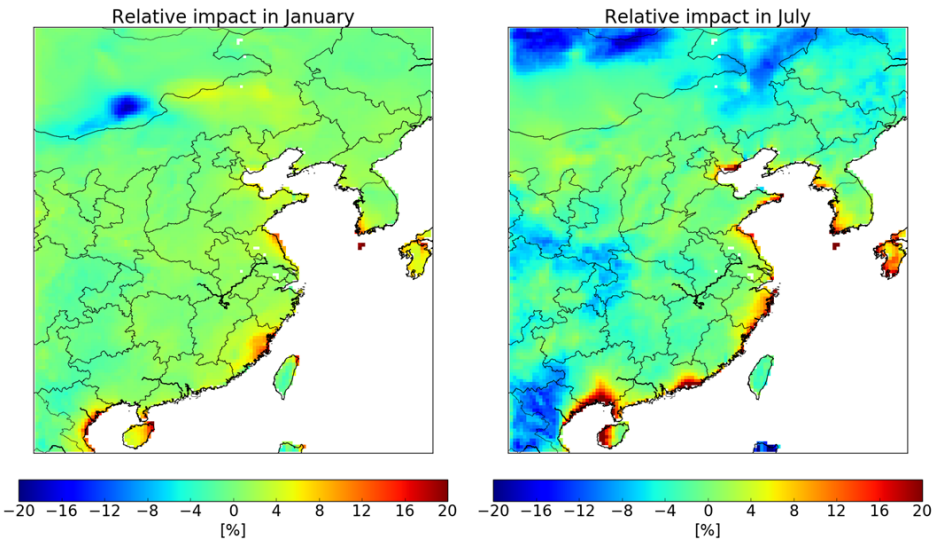

Figure 4.4: The relative impact of maritime emissions on the NO_2 columns over land in January and July 2015

MIX inventory (Li et al., 2017), which includes no maritime emissions, and the other using a combination of the MIX inventory and the maritime emissions of DECSO. We exclude the maritime emissions over the grid cells with more than 5 % covering land due to the difficulty in distinguishing them from other sources over land. This will result in an underestimation of the contribution of maritime emissions. From the model results, we see that the shipping lanes near the coast are always covered by the outflow from the mainland. The difference in NO_2 columns between the two runs is regarded as the contribution from shipping emissions. The contribution is higher in summer than in winter due to the summer monsoon wind from ocean to land (see Figure 4.4). In summer, the maximum occurred at the coastal areas of Fujian and Guangzhou Provinces and the contribution can be as high as 20 %. In winter, the contribution from shipping emissions to coastal cities is smaller. The non-negligible effect of shipping emissions can lead to large uncertainties in model simulations using emission inventories without the maritime sector.

4.4. Discussion

To further validate our shipping emissions, we compare them with the emissions derived with the STEAM model (Jalkanen et al., 2016), which uses the AIS data

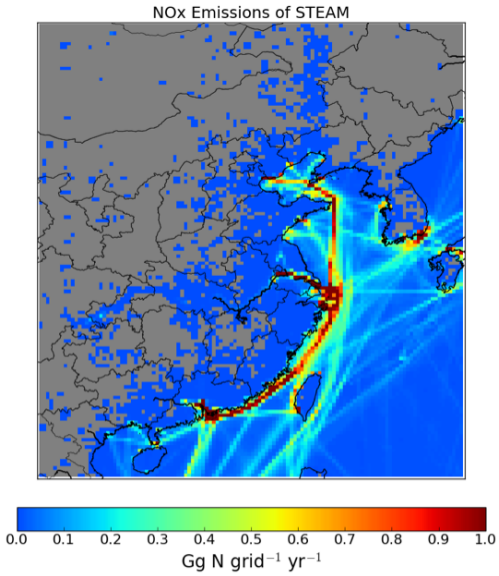

Figure 4.5: Shipping emissions derived from the STEAM model using AIS data in 2015.

worldwide. Data for the Asian region is available only for the year 2015. The resolution of STEAM data is 10 km × 10 km. For a meaningful comparison, we regrid the dataset to the same resolution as used by DECSO. Figure 4.5 shows the regridded shipping emission map of STEAM. We see that DECSO (Figure 4.1(b)) is in fairly good agreement with STEAM for shipping emissions with a strength higher than 0.4 Gg N per grid cell per year. However, shipping lanes with limited ship traffic are not visible in the DECSO data, because the resolution of DECSO emissions is limited to the pixel size of satellite observations. The coarse resolution of model and satellite observations can lead to an underestimation of shipping emissions (Valin et al., 2011). The longer lifetime of NO_2 and fewer observations in winter also lead to larger uncertainties in allocating emissions in DECSO. STEAM has uncertainties because of errors in the emission factor and incomplete AIS data. We calculate the annual emissions of STEAM data for the selected three regions. In 2015, over the Bohai Sea, Yellow Sea, Shanghai-Guangzhou regions, the annual detected total surface emissions are 23 Gg N, 84 Gg N and 215 Gg N with STEAM, while they are respectively 63 Gg N, 120 Gg N and 287 Gg N derived with DECSO. A fair agreement is found over the Yellow sea and the Chinese coastal region between Shanghai and Guangzhou. Over the Bohai Sea area, the emissions of DECSO are much higher than those of STEAM. However, since DECSO is estimating total emissions over sea, including ships without AIS and emissions from marine oil platforms, which are frequent in this region, emissions of DECSO are expected to be higher here.

The shipping emissions derived with DECSO are also comparable with other recent studies. Fan et al. (2016) used the AIS data to estimate shipping emissions in 2010 near the Yangtze River Delta. The results showed that annual shipping emissions in a zone bewteen 100–200 km of the coastlines are 150 Gg N per year and in the zone of 200-300km shipping emissions are 63 Gg N per year. Over the same areas, the emissions of DECSO are 143 Gg N per year and 71 Gg N per year respectively, which is within a 10 % error margin. H. Liu et al. (2016) derived shipping emissions from AIS data over Chinese seas in 2013, which were about 1799 Gg N per year for the Chinese coastal seas. For the same region, our estimated emissions are about 1422 Gg N per year. Note that the maritime emissions of DECSO excludes emissions over grid cells containing even a small fraction of land. Since these studies for different areas and different years are consistent with emissions from DECSO, these comparisons give us more confidence in our derived emissions and trend analysis.

4.5. Conclusions

In this study, we present the first long-term record of satellite-derived emissions over Chinese seas by using the DECSO algorithm. DECSO is able to detect total surface emissions under the strong outflow of NO_2 from Mainland China and can be applied to any other region of the world. The emissions are coming from off-shore platforms and all motorized ships. The continually increasing trend of NO_x emissions over sea is in agreement with the fact that no effective regulations have been implemented for ships in China. Our model simulations show that shipping emissions can contribute up to 5–20 % to local NO_2 concentrations at the densely populated coast. Since data about shipping emissions over China are usually not available, the air quality simulations and forecasts suffer large uncertainties especially near coast areas. DECSO provides monthly emissions for the last ten years, which provides missing information of emissions over ocean to modellers. In the future, when better satellite observations become available that have higher temporal and spatial resolution, e.g. TROPOMI (Veefkind et al., 2012) on a sun-synchronous satellite and geostationary satellites with instruments like GEMS (Kim, 2012) over Asia, Sentinel-4 (Ingmann et al., 2012) over Europe, and TEMPO (Zoogman et al., 2017) over America, we expect to detect even NO_x emissions of low-density ship tracks from space and subsequently to further improve shipping emission inventories.

Acknowledgements

The research was part of the OMI project funded and supported by the Netherlands Space Office. We acknowledge IPSL/LMD, INERIS and IPSL/LISA in France for providing the CHIMERE model. The NO_x emission data of DECSO are available on www.globemission.eu. The NO_x emission data of STEAM can be obtained by contacting co-authors J.-P. Jalkanen and L. Johansson.

5

Intercomparison of NO_x emission inventories over East Asia

We compare nine emission inventories of nitrogen oxides including four satellite-derived NO_x inventories and the following bottom-up inventories for East Asia: REAS (Regional Emission inventory in ASia), MEIC (Multi-resolution Emission Inventory for China), CAPSS (Clean Air Policy Support System) and EDGAR (Emissions Database for Global Atmospheric Research). Two of the satellite-derived inventories are estimated by using the DECSO (Daily Emission derived Constrained by Satellite Observations) algorithm, which is based on an extended Kalman filter applied to observations from OMI or from GOME-2. The other two are derived with the EnKF algorithm, which is based on an ensemble Kalman filter applied to observations of multiple species using either the chemical transport model CHASER or MIROC-chem. The temporal behaviour and spatial distribution of the inventories are compared on a national and regional scale. A distinction is also made between urban and rural areas. The intercomparison of all inventories shows good agreement in total NO_x emissions over mainland China, especially for trends, with an average bias of about 20 % for yearly

This chapter has been published in Atmospheric chemistry and physics techniques as Ding et al.(2017b).

emissions. All the inventories show the typical emission reduction of 10 % during the Chinese New Year and a peak in December. Satellite-derived approaches using OMI show a summer peak due to strong emissions from soil and biomass burning in this season. Biases in NO_x emissions and uncertainties in temporal variability increase quickly when the spatial scale decreases. The analyses of the differences show the importance of using observations from multiple instruments and a high spatial resolution model for the satellite-derived inventories, while for bottom-up inventories, accurate emission factors and activity information are required. The advantage of the satellite-derived approach is that the emissions are soon available after observation and that they are comprehensive (all sources included), while the strength of the bottom-up inventories is that they include detailed information of emissions for each source category.

5.1. Introduction

Emission sources are one of the crucial drivers for a chemical transport model (CTM). Accurate spatial and temporal emission distributions of air pollutants are important for air quality simulations and forecasts (Ma and van Aardenne, 2004; Eder et al., 2009; Zhang et al., 2012; Struzewska et al., 2016). Up-to-date emission information is also needed to help policy makers for efficient regulations to control air pollution. In general, two approaches are used to develop emission inventories. One approach is based on statistics combining local information such as emission activity rates and factors of different source categories (Streets et al., 2003). Here we refer to the inventories using this approach as bottom-up inventories. This method results in detailed information on the type, source sector, fuel and technology. The country-specific emissions are distributed in space with the location of the emissions using representative proxy data. Advances on temporal distribution are still needed to obtain representative maps that go beyond monthly resolution. However, large uncertainties are often introduced due to the uncertainties on all the input parameters in the calculation (Jaegle et al., 2005; Castellanos et al., 2014; Zheng et al., 2014; Li et al., 2016, 2017; Saikawa et al., 2017). It is also time consuming to collect all required information. Another approach to construct emission inventories is inverse modelling using satellite observations to constrain emissions by reducing the discrepancy between the modelled and observed concentrations and taking model and observation errors into account (Müller and Stavrakou, 2005; Konovalov et al., 2006; Sofiev et al., 2009; Miyazaki et al., 2012; Mijling et al., 2013; Streets et al., 2013; Stavrakou et al., 2016). In this study, the emissions derived with this approach are referred to as satellite-derived emissions. Since observations from satellite instruments like the Global Ozone Monitoring Experiment-2 (GOME-2) and the Ozone Monitoring Instrument (OMI) achieve near-global coverage in a single day, we expect that emissions derived from these satellite observations are well constrained on a daily and global basis. A limitation of satellite-derived emission inventories is the difficulty to distinguish emissions from different source categories.

Nitrogen oxides ($NO_x = NO_2 + NO$) play an important role in the formation of tropospheric ozone and secondary nitrate aerosols and in climate change (Jacob et al., 1996; Shindell et al., 2009). The emissions of air pollutants increased rapidly during the last two decades in East Asia due to the rapid economic development. Satellite observations as evidence show a strong increasing trend of NO_2 column concentrations since 1995 in China (Irie et al., 2005; Richter et al., 2005; van der A et al., 2006). Akimoto and Narita (1994) built the first regional NO_x emission inventory for Asia at a resolution of $1^\circ \times 1^\circ$. Van Aardenne et al. (1999) estimated NO_x emissions from 1990 to 2020 based on an energy consumption scenario to illustrate

the situation of the rapid increase in NO_x emissions in Asia. The early stage emission inventories including the Asian region had large inaccuracies because of the insufficient information on emission factors in this region, which were often based on information obtained from studies conducted in European or North American countries (Ma and van Aardenne, 2004). Several follow-up studies have been carried out to derive improved emission inventories for this region. Streets et al. (2003) constructed a comprehensive regional emission inventory with more species in support of the TRACE-P (Transport and Chemical Evolution over the Pacific) mission for Asia in 2000. However, Wang et al. (2004) concluded that the NO_x emissions of the TRACE-P inventory are largely underestimated, especially for China, compared to the emissions constrained by measurements from ground stations and aircrafts. Q. Zhang et al. (2009) developed an updated Asian inventory for the INTEX-B (Intercontinental Chemical Transport Experiment-Phase B) mission in 2006, which was based on the TRACE-P inventory but with refined temporal and spatial resolution. In 2007, a long-term Asian inventory REAS (Regional Emission inventory in ASia) was developed by Ohara et al. (2007) to analyse the trend of emissions. Kurokawa et al. (2013) updated the REAS inventory to a higher spatial and temporal resolution. Lee et al. (2011) built the first version of the South Korean national emission inventory CAPSS (Clean Air Policy Support System) using more detailed local information for emission activities and factors. Tsinghua University developed the Chinese inventory MEIC (Multi-resolution Emission Inventory for China) based on earlier work of Q. Zhang et al. (2009) (http://www.meicmodel.org). Recently, Li et al. (2017) constructed the new Asian inventory MIX by combining different regional and national inventories including REAS version 2.1, CAPSS, and MEIC. Zhao et al. (2011) concluded based on Monte Carlo simulations that the uncertainties of bottom-up emissions of NO_x are about -13 to 37 % in China. The major uncertainties are due to oversimplified source classifications and roughly estimated emission factors. The main anthropogenic emissions of NO_x in China are from transport and coal-fired power plants (Liu et al., 2015; Saikawa et al., 2017; Li et al., 2017). Because of the rapid implementation of new technologies and air quality control regulations for power plants and vehicles in China, their emission factors and activities are also changing with time, which makes the bottom-up emission estimates more uncertain (Zheng et al., 2014; Liu et al., 2015).

Satellite observations of atmospheric species can be used to closely monitor changes in emissions, such as the trend, seasonality, and diurnal cycles of emissions (Streets et al., 2013). For example, with satellites it was observed that NO_x emissions in China started to decrease after 2011 (Gu et al., 2013; de Foy et al., 2016; Krotkov et al., 2016; van der A et al., 2017) as a result of the national regulations for denitrification equipment at power plants. Mijling and van der A (2012) for the first

time derived high-resolution ($0.25^\circ \times 0.25^\circ$) emissions over East Asia from satellites using an advanced inverse method called DECSO (Daily Emission estimates Constrained by Satellite Observations) based on an extended Kalman filter. Ding et al. (2015) demonstrated that this approach is able to detect the monthly change of NO_x emissions due to air quality regulations on a city level. Miyazaki et al. (2012) derived the first global NO_x emission estimates using an inversion technique based on an ensemble Kalman filter and improved this method to constrain NO_x emissions by using satellite observations of multiple species (Miyazaki and Eskes, 2013; Miyazaki et al., 2017). This method is referred to as EnKF in this thesis.

All emission inventories, both bottom-up and satellite-derived, are facing the same challenge of validation since it is difficult to directly measure emissions on the ground on such large scales. A common way to validate emission inventories is using them in a chemical transport model to simulate NO_2 column concentrations and compare these with in situ or satellite observations. In this way, however, the validations are highly related to the model performance, which may result in inconsistent conclusions (Zhao et al., 2011).

In this study, we compare the satellite-derived inventories from DECSO and EnKF with a comprehensive collection of regional bottom-up inventories for East Asia: REAS v2.1 and an interim version of 2.2, MEIC, CAPSS and EDGAR v4.3.1 (Emissions Database for Global Atmospheric Research). The global HTAP v2 is not used because in our domain it is identical to MIX, which includes REAS, MEIC, and CAPSS. To evaluate the effect of the satellite instrument, we compare two emission datasets from DECSO applied to GOME-2 and OMI observations. To examine the effect of the forecast model performance in the inversion, we compare two emission datasets from EnKF using different CTMs. The intercomparison of nine emission inventories is presented for the time period 2000–2015 for East Asia on a $0.25^\circ \times 0.25^\circ$. Figure 5.1 shows the emission maps in 2008 of all inventories used in this study, including an average of emissions from all these inventories over the selected domain (102–132° E, 18–50° N). The description of all emission inventories used in this study will be presented in Section 5.2. Section 5.3 shows the difference of the spatial and temporal distribution among the nine inventories. The uncertainties of the inventories are discussed in Section 5.4.

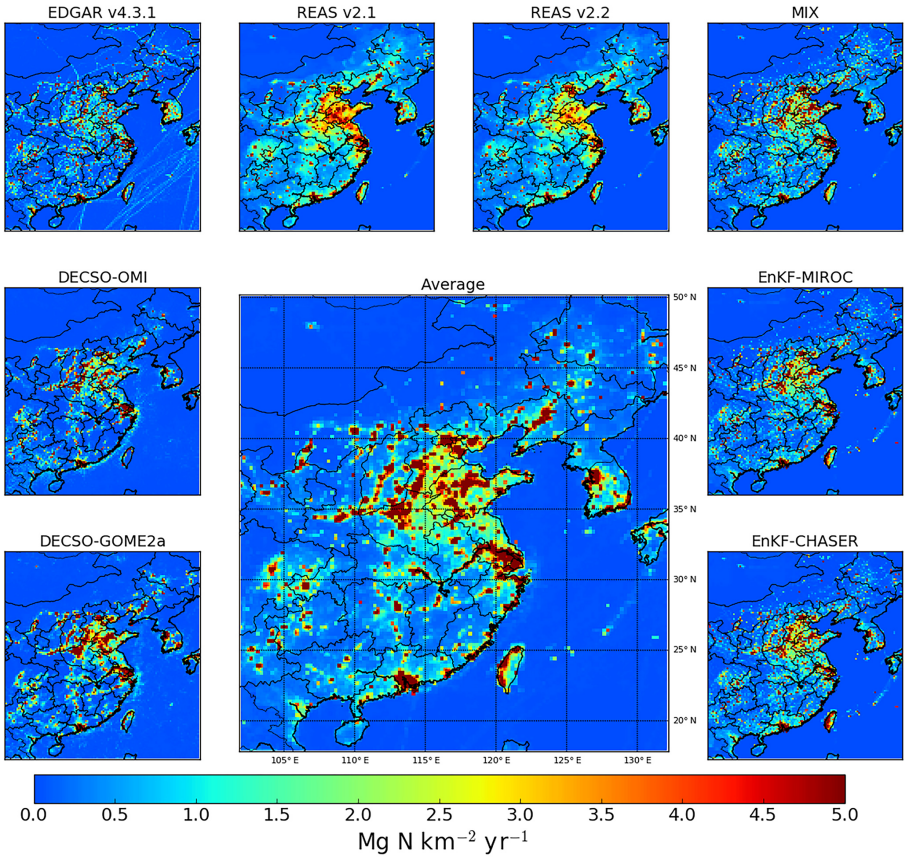

Figure 5.1: NO_x emissions over East Asia of all inventories in this study and their average in 2008. The averaged emissions over land are the mean of all emission inventories. Over the ocean the emissions are the average of DECSO-OMI, DECSO-GOME2, REAS v2.2 and EDGAR v4.3.1.

5.2. Emission inventories

5.2.1. Bottom-up inventories

5.2.1.1. EDGAR

The Emissions Database for Global Atmospheric Research (EDGAR) (Janssens-Maenhout et al., 2013) is a global bottom-up emission inventory using consistent methodology allowing straightforward implementation of scenario assumptions. Emission calculations of the latest version, v4.3.1, are based on information of international energy balances of IEA (IEA, 2014a, b) and agricultural statistics of FAO (2012) and other national or regional statistical information. EDGAR classifies

emissions into 12 source sectors: energy, combustion in manufacturing industry, industrial processes and product use, oil production and refining, fossil fuel fires, road transport, non-road ground transport, aviation, shipping, agricultural waste burning, residential and others. It provides global gridded maps of sector specific and historical emission data from 1970 to 2010 (monthly for 2010) with a high spatial resolution of $0.1^\circ \times 0.1^\circ$. A detailed description of EDGAR v4.3.1 can be found in Crippa et al. (2016). In this study, we use the yearly emissions of NO_x from 2000 to 2010 integrated to a resolution of $0.25^\circ \times 0.25^\circ$ on our study domain.

5.2.1.2. REAS

The Regional Emission inventory in ASia (REAS) v2.1 (Kurokawa et al., 2013) provides NO_x emission from 2000 to 2008 at a $0.25^\circ \times 0.25^\circ$ horizontal resolution. REAS v2.1 is based on the previous version REAS v1.1 with updates of activity data and parameters as well as an improvement of temporal and spatial resolution. It enlarges the domain by adding central Asia and the Asian part of Russia. REAS v1.1 was developed by Ohara et al. (2007) based on the methods described in Streets et al. (2003), which provided historical and future projected emissions from 1980 to 2020 at a $0.5^\circ \times 0.5^\circ$ resolution for East, Southeast and South Asia. REAS contains calculated NO_x emissions for the source sector of energy, industry, transport, domestic, agricultural activities and soil. We use NO_x emission data of REAS v2.1 and an interim version of 2.2 (hereafter REAS v2.2 for convenience) of 2005 to 2010 to expand the time series of the current REAS inventory. REAS v2.1 includes shipping, aviation emissions that are taken from EDGAR v4.2. In REAS v2.2, soil emissions and all emissions over central and Russian Asia are not included.

5.2.1.3. MEIC

Tsinghua University in Beijing has developed the Multi-resolution Emission Inventory for China (MEIC) model to generate an anthropogenic emission inventory for mainland China with a spatial resolution of 0.25°. NO_x emissions are presented in four sectors: energy, industry, transport and residential. The China coal-fired Power plant Emission Database (CPED) is used for the power plant sector. CPED includes the latest detailed information of emission factors, activity, locations, etc. and takes emission regulations into account as well (Liu et al., 2015). In the transportation sector, vehicle population and emission factors at county level are combined with a digital road map, vehicle and road type to derive high-resolution on-road transportation emissions (Zheng et al., 2014). More detailed information of MEIC is described in He (2012) and Li et al. (2017). We use monthly NO_x emissions of MEIC v1.2

from 2007 to 2012.

5.2.1.4. CAPSS

The Clean Air Policy Support System (CAPSS) is a Korean emissions inventory system which provides annual air pollutant emissions with a spatial resolution of 1 km in South Korea as described by Lee et al. (2011). For CAPSS, point source emissions are derived from both emission factors and activity data. The emission source sectors are classified into 12 sectors, which are the same as for EDGAR. The latitude and longitude are given for each point source to indicate their location. Area emissions are downscaled by using city–province-level activity data including a spatial allocation index database. On-road mobile emissions are calculated by using VKT (vehicle kilometres travelled) and spatially allocated by using traffic volume information for each road. In this study, we use CAPSS NO_x emissions from 2001 to 2013 and re-grid the data to a resolution of $0.25^\circ \times 0.25^\circ$.

5.2.1.5. MIX

MIX is a mosaic Asian anthropogenic emission inventory developed by the Model Inter-Comparison Study for Asia (MICS-Asia) and the Task Force on Hemispheric Transport of Air Pollution (TF HTAP) projects (Li et al., 2017). Five emission inventories of different regions are combined in MIX by normalizing source categories, species, and spatial and temporal resolution of each inventory and provides data in a consistent format. The five inventories are REAS v2.1, MEIC v1.0, PK-NH_3 (a high-resolution NH_3 emission inventory developed by Peking University), ANL-India (an Indian emission inventory developed by Argonne National Laboratory) and CAPSS. The spatial resolution of MIX is $0.25^\circ \times 0.25^\circ$. We use NO_x emissions from MIX in 2008 to represent both MEIC and CAPSS for the spatial comparison in this study.

5.2.2. Satellite-derived inventories

5.2.2.1. DECSO

Daily Emission estimates Constrained by Satellite Observations (DECSO) is an inverse modelling method to update daily emissions of NO_x based on an extend Kalman filter (Mijling et al., 2013). NO_x emissions are constrained by combining simulated NO_2 column concentrations of a regional CTM with satellite observations. The essential part in the inverse calculation is deriving the sensitivity of the NO_2 column concentrations on NO_x emissions. A simplified isobaric surface 2-D trajec-

tory analysis is used to take into account the transport of NO_2 from the source for a fast sensitivity calculation. In the Kalman filter, the emissions are assumed to follow a persistent model, which expresses that emissions of tomorrow will be equal to emissions of today. The Eulerian regional offline CTM CHIMERE v2013 (Menut et al., 2013) is used to obtain simulated NO_2 concentrations based on a priori emissions. Note that emissions derived with DECSO become independent from the a priori emissions after a spin-up time of about 3 months. CHIMERE is implemented at a $0.25^\circ \times 0.25^\circ$ horizontal resolution of the region for East Asia (102–120° E, 18–50° N) driven by the European Centre for Medium-Range Weather (ECWMF) operational forecast. The model is set up with eight vertical layers from the surface to 500 hPa. The CHIMERE-simulated columns are extended from 500 hPa to the tropopause with a climatological partial column (2003–2008 average) simulated by the global CTM TM5 for comparison with satellite observed tropospheric columns. The updates of emissions are related to the difference in NO_2 between the CTM simulation and satellite observations. A detailed description of DECSO can be found in Mijling et al. (2013), while the latest improvements are described in Ding et al. (2015, 2017). NO_x emissions detected with DECSO are regarded as total surface emissions. Note that the algorithm is not able to capture the emission with temporary changes less than 1 day.

DECSO v5 has been applied to observations from OMI (Ozone Monitoring Instrument) and GOME-2 (Global Ozone Monitoring Experiment-2). OMI is a Dutch–Finnish instrument aboard NASA's EOS-Aura satellite (Levelt et al., 2006). The pixel size is 24 km × 13 km at nadir and increases to about 150 km × 28 km at the edge of the swath. The overpass time of OMI at the equator is about 13:30 local time. We use the tropospheric NO_2 column data of the Dutch OMI NO_2 retrieval (DOMINO) algorithm version 2 (Boersma et al., 2011). GOME-2 is aboard the Sun-synchronous satellite MetOp-A with a local overpass time of around 09:30. The pixel size of the observation was 80 km × 40 km until 15 July 2013. Afterwards, the scan width of the orbit is halved and the pixel size is changed to 40 km × 40 km. Tropospheric NO_2 columns of GOME-2 are also retrieved with the algorithm DOMINO v2.

Observations are selected with a surface albedo lower than 20 % and a cloud radiance fraction lower than 70 %. The observations with clouds below 800 hPa are excluded. For OMI data, the pixels affected by the so-called row anomaly (KNMI, 2012) and the four pixels at each side of the swath are filtered out as well. The filter criteria are based on the analyses of Ding et al. (2015, 2017) to reduce the number of low-quality retrievals. The monthly DECSO v5 dataset used in this study is based on OMI satellite observations for the period of 2007–2015 (DECSO-OMI) and based on GOME-2 satellite observations for the period of 2008–2015 (DECSO-GOME2a). The data are available at www.globemission.eu.

5.2.2.2. Ensemble Kalman filter (EnKF)

Miyazaki et al. (2012) developed a data assimilation system to estimate global NO_x emissions based on an ensemble Kalman filter technique, which combines satellite observations with a global CTM. In this thesis, we refer to this method as EnKF. In this approach, surface NO_x emissions are included in the state vector together with other variables such as lightning NO_x sources and NO_2 concentrations. The dependence of NO_2 concentrations on NO_x emissions (including complicated chemistry and transport) is taken into account by using a background error covariance estimated from ensemble CTM forecasts. Miyazaki and Eskes (2013) demonstrated improved NO_x emission estimates by assimilating multiple species (including O_3 from TES and MLS, HNO_3 from MLS, CO from MOPITT). In this approach, the assimilation of non-NO_2 measurements (e.g. O_3 and CO) influences largely the concentration and chemical lifetime of NO_x and thus the surface NO_x emission estimates. Miyazaki et al. (2017) updated the EnKF system to combine NO_2 retrievals from OMI, GOME2 and SCIAMACHY together with the non-NO_2 measurements to optimize the diurnal emission variability. SCIAMACHY (aboard ENVISAT) (Bovensmann et al., 1999) operated from 2002 until 2012 with a local overpass time of 10:00 and global coverage every 6 days. The tropospheric NO_2 columns are retrieved with DOMINO v2 (Boersma et al., 2004). Observations with a cloud radiance reflectance lower than 50 % were used. Two emission datasets are derived using this approach with two different global CTMs: CHASER (Sudo et al., 2002) and MIROC-Chem (Watanabe et al., 2011) (referred to as EnKF-CHASER and EnKF-MIROC, respectively) for 2005–2015.

CHASER is coupled with an atmospheric general circulation model, CCSR/NIES/F-RCGC AGCM v5.7b at a horizontal resolution of 2.8° (T42) and 32 vertical levels on the sigma vertical coordinate system from the surface to 4 hPa (Miyazaki and Eskes, 2013). The AGCM fields were nudged toward NCEP/DOE-II reanalysis (Kanamitsu et al., 2002). The MIROC-Chem model (Watanabe et al., 2011) was developed based on CHASER, with many updates on the tropospheric chemistry and including stratospheric chemistry. MIROC-Chem is coupled to the atmospheric general circulation model MIROC-AGCM v4, at 2.8° (T42) horizontal resolution, and it uses the hybrid terrain-following pressure vertical coordinate system with 32 vertical levels from the surface to 4.4 hPa (Miyazaki et al., 2017). The MIROC-AGCM fields were nudged towards the 6-hourly ERA-Interim (Dee et al., 2011) reanalysis.

In both calculations, the a priori NO_x emissions are obtained from EDGAR v4.2 for anthropogenic emissions, GFED v3.2 (van der Werf et al., 2010) for biomass burning emissions and GEIA (Yienger and Levy, 1995) for soil emissions. For the comparison, the monthly emissions at 2.8° resolution from EnKF-CHASER and EnKF-

MIROC are redistributed to a horizontal resolution of $0.25° \times 0.25°$ based on emission distributions of the a priori inventory MIX. Note that the shipping emissions near the coast areas are added to land since they are not included in MIX. This could lead to overestimation of emissions over land near busy shipping lanes.

5.3. Intercomparison of NO_x emissions

5.3.1. Temporal evaluation

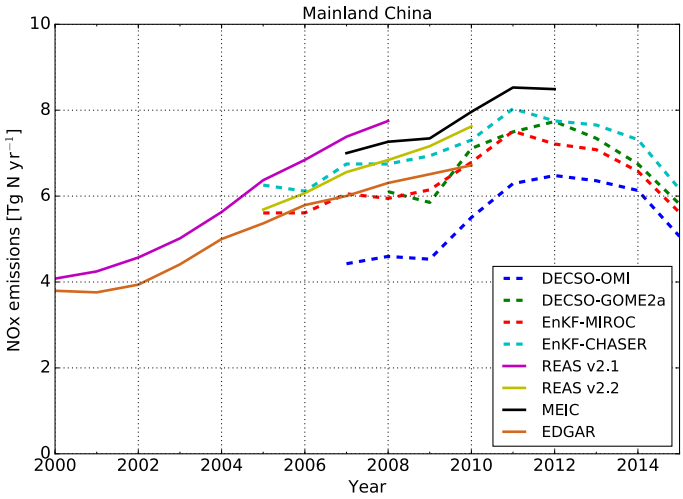

Figure 5.2: Annual NO_x emissions from eight emission inventories over mainland China in the selected domain (Figure 5.1).

5.3.1.1. Time series analysis

Figure 5.2 shows the comparison of all emission inventories as a function of time over mainland China (in this thesis limited to the study domain shown in Figure 5.1) for the period 2000–2015. The time series of the annual total emissions show a large variation among the inventories. The bottom-up inventories use similar approaches, but the statistical data and assumptions on the penetration and specification of the present technologies used for their calculations are different and this explains the diversity among the bottom-up inventories. The differences among the satellite-derived emission inventories are caused by different inversion techniques, satellite observations and CTMs. The emissions derived by DECSO with OMI observations show a large discrepancy with the other inventories. Over mainland China

(Figure 5.2), all inventories follow a similar trend but with large biases. The NO_x emissions dramatically increase since 2000 and start to decrease around 2011. All satellite-derived inventories show a decrease in 2015 of at least 20 % compared to 2014. The average annual total emissions of 2008 (the only year included in all inventories) are about 5 ± 1 Tg N yr^{-1} for mainland China. REAS v2.1 presents the highest value of 7.3 Tg N yr^{-1}, while DECSO-OMI shows the lowest value of 4.3 Tg N yr^{-1}. The standard deviation of the emissions is about 20 %. For comparison, Li et al. (2017) reported typical uncertainties of 31–37 % for bottom-up inventories over China.

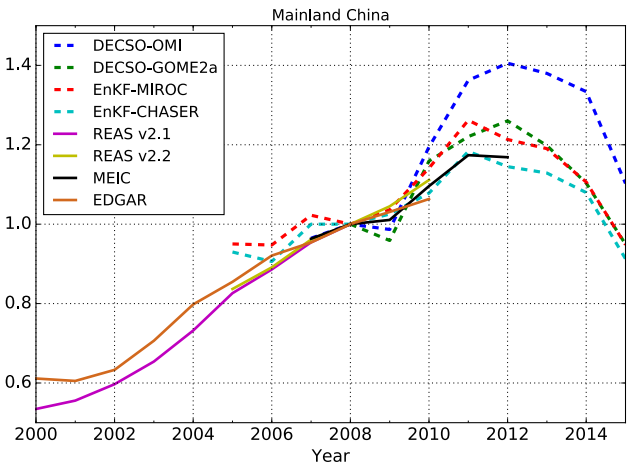

Figure 5.3: Normalized annual NO_x emissions from eight emission inventories over mainland China in the selected domain (see Figure 5.1). The time series are normalized to their value in 2008.

Figure 5.3 shows the comparison of the temporal variation relative to the emissions in 2008. REAS v2.1 and v2.2 and EDGAR v4.3.1 show a continuous increase from 2000 to 2010 with an annual increase rate of about 8 % on average. NO_x emissions of China in 2010 are almost doubled compared to emissions in 2000. The change rates derived with two EnKF emissions are lower than for REAS and EDGAR between 2005 and 2010. MEIC and satellite-derived emissions show a slow change of NO_x emissions from 2007 to 2009 and a large increase in 2010 until 2011, which is consistent with satellite observations (Gu et al., 2013; de Foy et al., 2016; Krotkov et al., 2016), whereas REAS and EDGAR reveal a continuous increase during 2007–2010. The increase rate in 2011 of DECSO-OMI is about 10 % higher than of the other inventories. From 2012 to 2015, the satellite-derived emissions show a decrease in total NO_x emissions over China by about 30 %. Nevertheless, the peak year is different between the satellite-based approaches. The DECSO inventories show a decrease starting in 2012, while the EnKF inventories reach their peak in 2011.

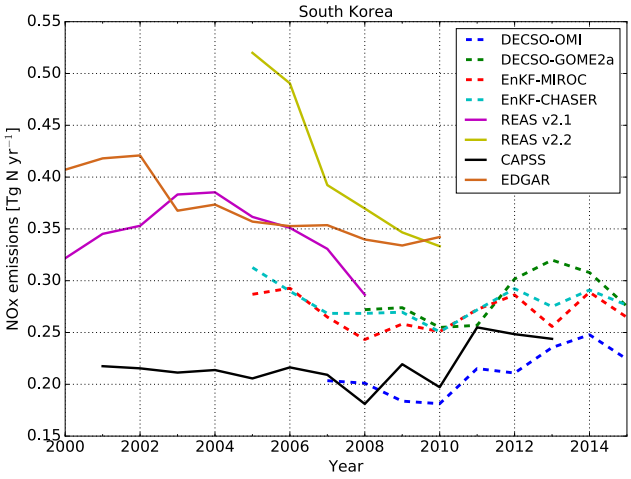

Figure 5.4: Annual NO_x emissions from eight inventories over South Korea.

Over a small domain, the discrepancies among the inventories are larger. As an example, Figure 5.4 shows the comparison of the emission time series from eight inventories in South Korea. We see differences by a factor of up to 2 between the inventories in 2008 (the highest one is REAS v2.2 and the lowest one is CAPSS). The bottom-up inventories EDGAR and REAS show higher emissions than the satellite-derived emissions. The satellite-derived inventories are generally in closer agreement to the South Korean CAPSS than to the other bottom-up inventories. These results highlight the large differences in the emission trends over a small region like South Korea, even derived with a similar approach.

The satellite-based approaches can be used to make near-real-time datasets and to extend the emission record over a longer period until 2015. Figure 5.5a displays the peak year of the averaged NO_x emissions from the four satellite-derived inventories. Beijing and Shanghai reach their peak years as early as 2010 and 2008, respectively. Most of the developed provinces reach maximum emissions in 2011 or 2012. In some less developed provinces, emissions were still growing until 2014. To analyse the correlation of the time series of the four satellite-derived inventories for each province, we calculate the temporal correlation coefficient (R) from each combination of the four emission datasets. Figure 5.5b shows the minimum correlation coefficient of all combinations. The satellite-derived emission inventories are in good agreement for most of the provinces, with a correlation coefficient higher than 0.6. The provinces with smaller areas often have lower R values. This means that the uncertainties of NO_x emissions can be notably high on a small area or provincial level.

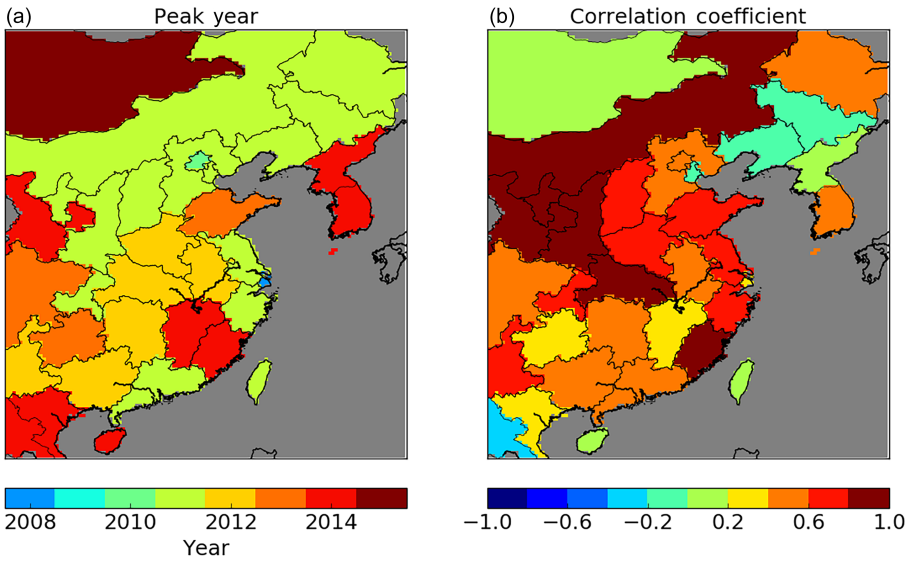

Figure 5.5: The peak year **(a)** of the average annual NO_x emissions from the four satellite-derived inventories (DECSO-OMI, DECSO-GOME2a, EnKF-CHASER and EnKF-MIROC) for various provinces and regions. **(b)** The map image shows the minimum temporal correlation coefficient of all combinations of the four emission datasets.

5.3.1.2. Monthly variability

We calculate the mean monthly emissions of each inventory for its own available time period and normalize them to get the general monthly variability. Figure 5.6 shows the monthly variability in total NO_x emissions for seven inventories over mainland China. MEIC, REAS v2.1 and DECSO-GOME2a show a relatively weak variability, while the other four inventories show a distinct summer peak. The EnKF inventories show a sharp peak in June. REAS v2.1 and DECSO-OMI reveal a peak in July. The summertime peak is probably introduced by enhanced biogenic (e.g. from soils) emissions. The summertime enhancement is considered to be better detected by the OMI afternoon measurements than the GOME2 morning measurements (Boersma et al., 2009) because they are generally maximized in the afternoon. The different representation of the summertime peak between the satellite-derived inventories will be discussed in Section 5.4. It is notable that all inventories show that NO_x emissions are about 10 % lower in February than in the surrounding months, which is due to the Chinese New Year (Ding et al., 2015). All inventories also show a peak in December, when heating and electricity consumption is usually high in China.

To study the temporal correlation of monthly different inventories, we use

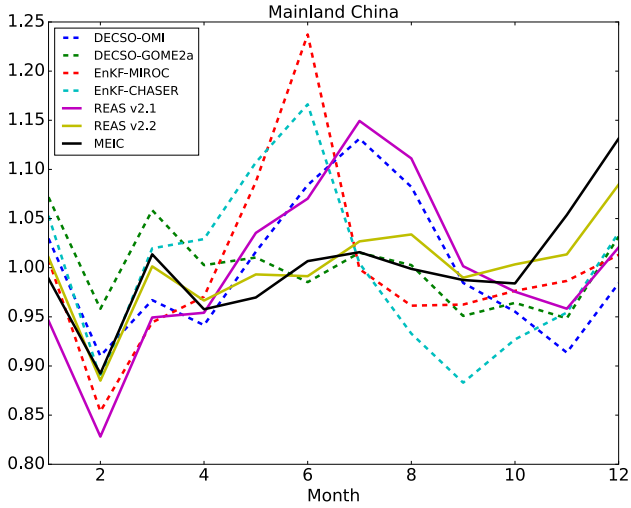

Figure 5.6: Monthly variability in NO_x emissions over mainland China in the selected domain (see Figure 5.1).

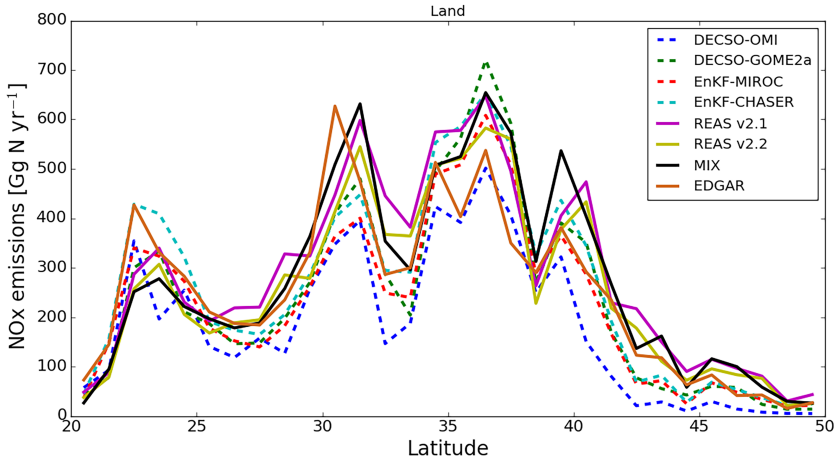

Figure 5.7: Latitudinal distribution of longitudinal total NO_x emissions over land. The emissions are summed over a 1° longitudinal band above land.

monthly emissions over mainland China of the common period (2008–2010, i.e. 36 months) for DECSO, EnKF, MEIC, and REAS v2.2. Table 5.1 shows the correlation coefficient of monthly total emissions from different inventories over mainland China from 2008 to 2010. The two DECSO inventories show a relatively good correlation with MEIC and REAS. The correlation coefficient between the two DECSO inventories is only 0.75 as a result of the different seasonality (see Figure 5.6). This implies that the observed seasonality can be highly affected by

Table 5.1: Temporal correlation coefficient of the 36 pairs of monthly NO_x emissions over mainland China from 2008 to 2010. The bold values indicate the relation between bottom-up and satellite-based inventories.

	REAS v2.2	MEIC	EnKF-MIROC	EnKF-CHASER	DECSO-GOME2a
DECSO-OMI	**0.72**	**0.6**	0.52	0.45	0.75
DECSO-GOME2a	**0.78**	**0.74**	0.46	0.28	1
EnKF-CHASER	**0.43**	**0.43**	0.65	1	–
EnKF-MIROC	**0.46**	**0.43**	1	–	–
MEIC	0.91	1	–	–	–

the choice of satellite observations, reflecting differences in the local overpass time and pixel size. The two EnKF inventories based on the same observations but using different forecast models show a strong correlation. However, for most cases on a provincial or a small regional level, no significant correlation of monthly variability from different approaches can be found (not shown). Due to the coarse resolution of the EnKF emission estimates (i.e. 2.8°), the seasonality can be strongly mixed up between urban and rural areas within a coarse model grid. The uncertainty in temporal variability in NO_x emissions becomes larger with decreasing spatial scale of emissions, especially where surface types are inhomogeneous.

Table 5.2: Spatial correlation coefficients of annual NO_x emissions in 2008 over land on a provincial level in China and other regions outside China. (The total number of provinces and regions is 33, i.e. 29 Chinese provinces, South Korea, North Korea, and parts of Mongolia (83 %) and Vietnam (43 %); see Figure 5.1. The study domain only covers part of the provinces Heilongjiang (74 %), Inner Mongolia (83 %) and Yunnan (36 %).) The bold values indicate the relation between bottom-up and satellite-based inventories

	EDGAR v4.3.1	REAS v2.1	REAS v2.2	MEIC	EnKF-MIROC	EnKF-CHASER	DECSO-GOME2a
DECSO-OMI	**0.84**	**0.90**	**0.91**	**0.92**	0.96	0.95	0.98
DECSO-GOME2a	**0.85**	**0.92**	**0.94**	**0.95**	0.96	0.96	1
EnKF-CHASER	**0.88**	**0.92**	**0.93**	**0.95**	1	1	–
EnKF-MIROC	**0.88**	**0.94**	**0.95**	**0.95**	1	–	–
MEIC	0.89	0.99	0.98	1	–	–	–
REAS v2.2	0.90	0.99	1	–	–	–	–
REAS v2.1	0.88	1	–	–	–	–	–
EDGAR v4.3.1	1	–	–	–	–	–	–

5.3.2. Spatial distribution

In this section, we choose the year 2008 to compare the bias and spatial distribution, since it is the only year that is contained by all inventories. Because DECSO inventories have a grid that is half a grid cell shifted compared to the other inventories, the comparison per grid cell could theoretically result in up to 40 % discrepancy in correlation coefficients due to re-gridding. The calculated discrepancy decreases

to less than 10 % at a resolution of 1° or more. For a fair comparison, we check the correspondence in spatial distribution on a provincial level. We calculate the correlation coefficient (R) of each two inventories on a regional or provincial level (in total 33 regions including 29 Chinese provinces, South Korea, North Korea, and parts of Vietnam (43 %) and Mongolia (53 %), as shown by Figure 5.1. Note that our domain covers only a part of the provinces Heilongjiang (74 %), Inner Mongolia (83 %), Sichuan (51 %) and Yunnan (36 %). The comparison result is summarized in Table 5.2. We use the MIX inventory for 2008 to represent both MEIC and CAPSS depending on the region of interest, since MIX covers the whole domain. All correlation coefficients are above 0.8, which means that the spatial distribution on a regional or provincial level have a good agreement among all inventories. The emission correlations are higher when the emissions are derived with similar methods. Both DECSO inventories have the best correlation with the EnKF inventories, with R values around 0.95. EnKF-CHASER and EnKF-MIROC show a similar spatial distribution. For the two EnKF inventories, the original 2.8° resolution data were subsequently re-gridded to a finer resolution using the same fine-scale distribution. Both REAS inventories have very high correlations (R values are 0.98 and 0.99) with MIX since the same provincial activity data of China are used for calculating emissions in MIX and in REAS v2.1 (Kurokawa et al., 2013). The correlation between EDGAR v4.3.1 and other bottom-up emission inventories is relatively low ($R <$ is about 0.89). EDGAR v4.3.1 uses the emission information from IEA (2014) statistics (before the coal statistics revision of China) and CARMA v3.1 for distribution while MIX and REAS are based on national statistics, which may lead to the discrepancy.

Both the bottom-up and satellite-derived inventories show large biases but their spatial distributions are similar on a provincial scale. To further examine the spatial distribution and biases, we combine the emissions in bins of 1° latitude and compare the longitudinal total emissions over land in the study domain. Figure 5.7 shows that all inventories have similar patterns over latitude but with large biases. The standard deviation averaged over the latitudes (20–50° N) between all the inventories is 27 %. For areas, north of 40° N, the satellite-derived emission inventories are lower than the bottom-up inventories. The relative standard deviation is also large (from 40 to 80 %) at high latitudes.

Note that the satellite-derived emissions are total surface emissions including anthropogenic, biogenic, and shipping emissions. MEIC and REAS v2.2 include only anthropogenic emissions. REAS v2.1 includes all emissions except for lightning by adding the aviation and international shipping emissions from EDGAR v4.2. These differences make the comparison inconsistent. To conduct consistent comparisons, we divide the domain into urban and rural areas based on land-use information and compare the emissions over each area. We use the land-use information at a

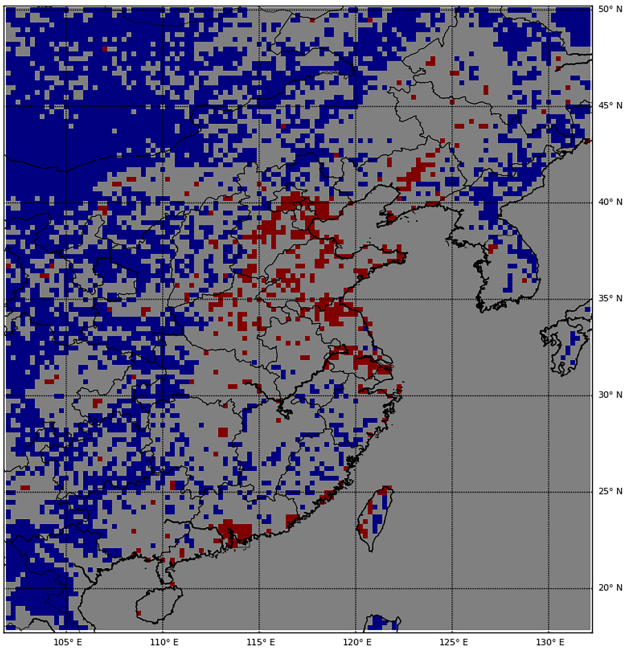

Figure 5.8: The distribution of urban grid cells (red) and rural grid cells (blue). Urban grid cells have an urban area (as defined in the GCLC database) larger than 5 % of the grid cell. Rural grid cells are 100 % covered by vegetation (including agricultural land, grass land, shrubs, forest) or barren land.

resolution of 300 m from the GlobCover Land Cover (GCLC version 2.3) database, which is updated for the year 2009. We assume that an urban grid cell has more than 5 % coverage of urban land. In GCLC, urban areas are defined as artificial surface and associated areas. If the grid cell is 100 % covered by vegetation (including agricultural land, grass land, shrubs, forest) or barren land, it is regarded as a rural grid cell. We note that the anthropogenic emissions can still be the dominant source over the rural grid cells because urban areas (for example highways, small factories) can be smaller than the resolution of the GCLC data (300 m). Figure 5.8 shows the distribution of the urban and rural grid cells. The urban grid cells account for 4.5 % of the total land area, while the rural grid cells cover about 41 %.

Figure 5.9 shows that the meridional distributions of emissions from all inventories over urban grid cells are in good agreement. Even though the urban grid cells are only about 4.5 % of total land cover, they contribute to about 50 % of the total emissions over the whole domain. The range of the total urban emissions is between about 2.0 (REAS v2.2) and 3.4 (MIX) Gg N yr^{-1}. The standard deviation of the total urban emissions is about 19 % of the ensemble mean. The urban emissions from DECSO-OMI is apparently lower than others above 40° N. The ur-

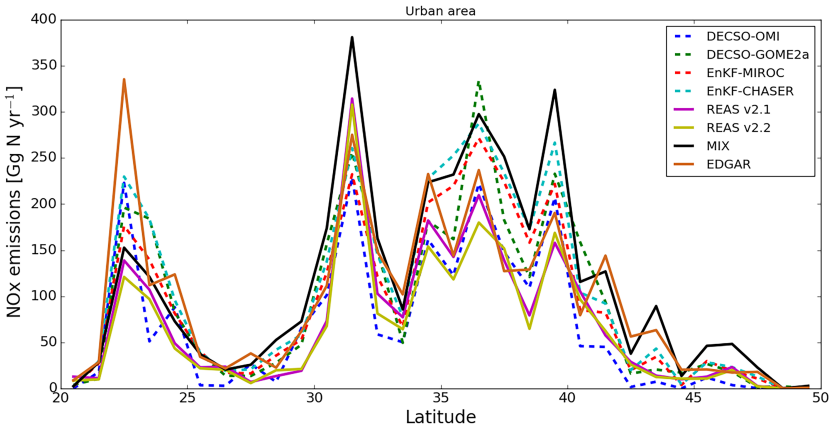

Figure 5.9: Latitudinal distribution of longitudinal total NO_x emissions over urban areas (the red cells in Figure 5.8).

ban emissions over the areas above 40° N contribute to only 6 % to the total urban emissions over the whole domain in DECSO-OMI; the other inventories show larger contributions (about 10–15 %).

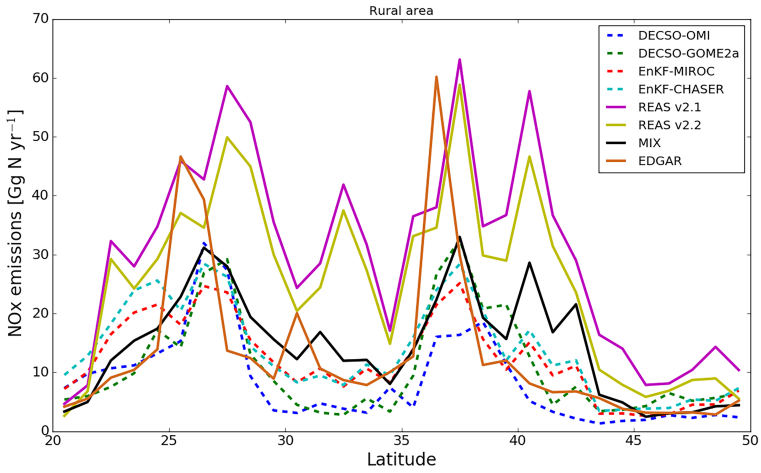

Figure 5.10: Same as Figure 5.9, but for rural grid cells (the blue cells in Figure 5.8).

Figure5.10 shows that the emissions of all inventories over rural grid cells have wide spread along latitudes. The emissions over rural areas contribute to about 8 % of the total emissions (254–900 Gg N yr^{-1}) on average with a relative standard deviation of about 44 % to the total emissions over the domain. EDGAR v4.3.1 emissions, which include biogenic (biofuel and biomass) emissions, are even lower than MIX and REAS v2.2, which include only fossil fuel emissions. The relative differences

in emissions over rural areas are much larger than over urban areas, especially for the bottom-up inventories. These results suggest that large uncertainties over rural areas exist in the current bottom-up inventories. The mean differences are usually smaller for the satellite-derived inventories.

Table 5.3: Temporal correlation coefficient of the 12 pairs of monthly total NO_x emissions over urban areas in the common year 2008. The bold values indicate the relation between bottom-up and satellite-based inventories.

	REAS v2.1	REAS v2.2	MIX	EnKF-MIROC	EnKF-CHASER	DECSO-GOME2a
DECSO-OMI	**0.73**	**0.61**	**0.34**	0.5	0.22	0.69
DECSO-GOME2a	**0.53**	**0.67**	**0.48**	0.72	−0.04	–
EnKF-CHASER	**0.28**	**0.21**	**0.47**	0.21	–	–
EnKF-MIROC	**0.11**	**0.24**	**0.25**	–	–	–
MIX	0.72	0.83	–	–	–	–
REAS v2.2	0.93	–	–	–	–	–

Table 5.4: Same as Table 5.3, but for rural areas in 2008.

	REAS v2.1	REAS v2.2	MIX	EnKF-MIROC	EnKF-CHASER	DECSO-GOME2a
DECSO-OMI	**0.88**	**0.17**	**−0.31**	0.75	0.64	0.69
DECSO-GOME2a	**0.88**	**0.33**	**−0.21**	0.12	0.20	–
EnKF-CHASER	**0.46**	**−0.02**	**−0.12**	0.75	–	–
EnKF-MIROC	**0.47**	**0.20**	**0.04**	–	–	–
MIX	−0.13	0.80	–	–	–	–
REAS v2.2	0.43	–	–	–	–	–

The seasonal cycle of the urban grid cells is quite similar to the one shown in Figure 5.6 for all of mainland China. However, the seasonal cycle for the rural grid cells have a much stronger summer maximum for the inventories that include biogenic emissions. Tables 5.3 and 5.4 show the temporal correlation of monthly emissions among different inventories over urban and rural areas, respectively. The correlation coefficients are similar between the total emissions over land (Table 5.1) and over urban areas (Table 5.3). The two DECSO inventories have a high correlation over rural areas with REAS v2.1. A possible reason is that REAS v2.1 is the only bottom-up inventory in the comparison, which includes biogenic emissions. The EnKF datasets have low correlations with all bottom-up inventories probably due to its coarse horizontal resolution (see Section 5.3.1.2).

5.4. Discussion

5.4.1. Temporal analyses

Our intercomparison shows differences of about 10 % in the time series over of the regional total emissions over mainland China. The peak year of the Chinese country-total emissions was 2011 in the EnKF and MEIC inventories, which is consistent with the results of Liu et al. (2016). Irie et al. (2016) showed that NO_2 column concentrations derived from OMI observations started to decrease in 2011 in China. However, DECSO shows the peak year in 2012, which is consistent with the start of strict air quality regulations (van der A et al., 2017). Over South Korea, the local CAPSS inventory shows unchanging emissions until 2010 and increasing emissions since. REAS and EDGAR inventories show a strong decrease from 2005 to 2010 with large differences in the decrease rate. For bottom-up inventories, it is difficult to assume the correct timing of penetration of a given new technology. For instance, EDGAR assumes an immediate implementation of a new policy, e.g. low-NO_x burners, and so does not represent the real time of penetration of the new technology. All the satellite-based inventories show a decrease in 2015. This is different for concentrations derived from OMI measurements, which show a decrease from 2005 to 2013 and a slight increase in 2015 (Irie et al., 2016). Mijling et al. (2013) calculated that the NO_2 transported from outside the country contributes to about 7 % of the average NO_2 columns over South Korea. Thus, the trend of NO_2 column concentrations cannot always be used as an indication for the local emission because of influences of atmospheric transport. Miyazaki et al. (2017) indicated that an accurate emission trend requires an emission–concentration relationship that explicitly accounts for tropospheric chemistry and transport, which is included in advanced data assimilation techniques. This can cause significant differences between the bottom-up and satellite-derived emissions.

Three satellite-derived inventories (EnKF-CHASER, EnKF-MIROC and DECSO-OMI) and REAS v2.1 show a strong summer peak, which can be attributed to biogenic emissions in summer, such as enhanced soil emissions and emissions from biomass burning. REAS v2.1 includes biogenic emissions, while the other bottom-up inventories shown in Figure 5.6 include only anthropogenic emissions. Zhao and Wang (2009) concluded that soil emissions are enhanced in summer and contribute to at least 14 % of the total emissions in July in China. Soil emissions have a positive exponential relationship with soil temperature (Schindlbacher et al., 2004) and can be enhanced after precipitation over vegetation (Zörner et al., 2016), which could explain the seasonality in satellite-derived emissions in most parts of China. Also, emissions by biomass burning and crop burning are maximized in summer

in China (Li et al., 2016; Zhang et al., 2016). Stavrakou et al. (2016) pointed out that the current biomass burning inventories are underestimating emissions by crop burning in northeast China. This can lead to significant differences in the emission seasonality between the bottom-up and satellite-derived emissions. The OMI satellite instrument with an overpass time in the afternoon will observe more NO_2 from biomass burning than the GOME-2 instrument with its morning overpass time because of stronger biomass burning activities and high soil emissions in the afternoon (Boersma et al., 2008). This can explain why only the satellite-derived emission inventories based on OMI show a clear summer peak. The seasonality shown by DECSO-OMI and EnKF datasets is slightly different. One possible reason is the uncertainty in the NO_x chemical lifetime in the CTM. For instance, in summer, a too short lifetime can result in overestimation of emissions by the inversion method (Stavrakou et al., 2013). In addition, the EnKF data assimilation has frequent updates (every 120 min), which may lead to overcorrection in the estimated emissions due to the persistent underestimation of NO_x concentrations by the CTM.

5.4.2. Spatial analyses

All the inventories are in good agreement on the spatial distribution on a provincial level but with large biases. The differences in total annual emissions can increase to 100 % for small spatial scales, which is in line with recent studies on regional emission inventories. For example, Saikawa et al. (2017) compared five bottom-up inventories on a provincial and national scale in China and concluded that more improvements are needed for provincial emissions. All satellite-derived emissions are lower than that of bottom-up inventories at high latitudes (above 40° N). This is probably due to negative bias of satellite observations at higher latitudes in East Asia (Ding et al., 2017; Lorente et al., 2017). Another reason can be the overestimation of NO_x lifetime in the CTM for high latitudes (Stavrakou et al., 2013), which could cause underestimation of the estimated emissions.

5.4.3. Differences in the bottom-up emissions

The differences in emission activity and emission factors of each emission sector can lead to large discrepancies in the bottom-up emission inventories. Saikawa et al. (2017) and Li et al. (2017) showed that large discrepancies in bottom-up emission estimates over China are mainly related to different statistical data and emission factors for the energy and transport sectors. All three inventories use different provincial statistics. The emission factors of power plants are lower in MEIC as compared to EDGAR and REAS. More power plants are included in MEIC, which

uses the high-resolution database CPED for China. REAS uses two other global databases, CARMA (Carbon Monitor for Action) and WEPP (World Electric Power Plants), while EDGAR uses downscaled IEA (International Energy Agency) statistics and CARMA v3.1 for the distribution. For the transport sector, each inventory has its own sub-categories to calculate the total emissions. MEIC includes only on-road vehicle emissions, while EDGAR and REAS give off-road emissions including emissions from ships and aircrafts. For vehicle emissions, MEIC uses the information from local statistics, but large uncertainties still exist in vehicle emission factors and activities. The selected vehicle emissions factors do not include spatial variability and the emissions activities are based on surveys conducted in only a few cities (Zheng et al., 2014). More details about the difference in bottom-up inventories can be found in Li et al. (2017). For South Korea, the NO_x emissions from CAPSS, using local data of emission factors and activities based on local measurements, are much lower than from other bottom-up inventories.

5.4.4. Differences in the satellite-derived emissions

The differences in the satellite-derived emissions are introduced by differences in inversion techniques, chemical transport models, and observations. For instance, errors in the simulated NO_2 columns are largely influenced by the representation of lightning NO_x sources, especially in summer, and thus affect the quality of surface NO_x emissions estimates (Lin, 2012). In the EnKF analyses, lightning NO_x sources are simultaneously optimized using satellite measurements (Miyazaki et al., 2014), which can improve the surface emission estimation. In the DECSO algorithm, the NO_2 concentrations above 500 hPa were obtained from climatological data, and the lightning emissions are identified as surface emissions. The error in NO_x lifetime due to uncertainties in meteorological input and chemical processes also strongly affect the satellite-derived emission estimates (Lin et al., 2012; Stavrakou et al., 2013), which are differently represented in each model.

The emissions derived with DECSO using OMI are much lower than those from other satellite-derived inventories. The monthly variability is largely affected by changing the satellite observations in DECSO, which is attributed to the differences in the satellite overpass time (see Section 5.4.1) and uncertainty in modelled diurnal variations. NO_2 columns observed by GOME2 are on average 20 % higher than by OMI in the winter period (October–March), while they are up to 40 % in the summer period (April–September) in 2014, reflecting stronger daytime photochemical sinks from oxidation by OH in summer (Boersma et al., 2009). Although the OMI and GOME-2 retrievals were produced using the same retrieval algorithm (Boersma et al., 2011), Wang et al. (2017) concluded that GOME2-A/B has a larger

bias (about 30 %) than OMI satellite observations in Wuxi in China from 2011 to 2014. In addition, GOME-2 observes larger NO_2 columns from the transport sector due to the morning rush hour (Wang et al., 2017), whereas OMI has better capability to detect emissions from biomass burning that is usually at their maximum in the afternoon (Boersma et al., 2008; Miyazaki et al., 2017). To obtain better NO_x emission estimates from the satellite-based approach, it is useful to combine observations from multiple instruments obtained at different overpass time, as implemented in the EnKF inversions. Miyazaki et al. (2017) demonstrated that the application of a correction scheme for diurnal emission variability using multiple measurements (OMI, GOME-2, SCIAMACHY) is an important development in the emission estimates. Different from the DECSO algorithm, the EnKF emissions are obtained by assimilating multiple species, which provide constraints on various aspects of the tropospheric chemistry system to improve the NO_x emission estimates (Miyazaki and Eskes, 2013; Miyazaki et al., 2017). When comparing two NO_x emissions of EnKF-MIROC derived by assimilating multiple species and NO_2 only, the average bias is about 5 % for the annual total emissions over East Asia. This confirms that the emissions are strongly constrained by NO_2 observations but are also modified by non-NO_2 observations through their influences on the vertical profile and chemical lifetime of NO_x.

EnKF-CHASER and EnKF-MIROC use the same data assimilation framework but different CTMs. Our comparisons reveal that the estimated emissions are largely sensitive to the forecast model. The bias between the two EnKF datasets is about 15 % for the annual total emissions over the domain. The estimated emissions are generally higher in EnKF-CHASER than in EnKF-MIROC, which could be attributed to the larger amount of OH and thus shorter NO_x chemical lifetime in EnKF-CHASER.

DECSO inventories show better temporal correlation with other inventories, especially over rural areas. Our analyses suggest that the estimated emissions are strongly influenced by the choice of model resolution (0.25° in DECSO vs. 2.8° in EnKF). Insufficient model resolution could cause artificial dilution and errors in simulating non-linear chemical feedback of O_3–HO_x–NO_x chemical system. Valin et al. (2011) also discussed that a sufficient horizontal resolution of model to accurately simulate the non-linear effect is related to the size of the emission source (4 km for a small source to 48 km for a large city). High-resolution inversion is considered to be essential to improve the emission estimates at small scales and to derive better temporal changes over different types of areas.

5.5. Conclusions and recommendations

To investigate the uncertainties in NO_x emission estimates over East Asia, we compared nine NO_x emission inventories from satellite-derived and bottom-up approaches over East Asia. The bottom-up inventories are obtained from a global inventory (EDGAR v4.3.1), regional inventories over Asia (REAS v2.1 and an interim version of 2.2), and national inventories of China (MEIC) and South Korea (CAPSS). The four satellite-derived inventories were derived with different versions of DECSO and EnKF. DECSO-OMI and DECSO-GOME2a are based on an extended Kalman filter using observations from OMI and GOME-2, respectively. EnKF-CHASER and EnKF-MIROC are based on an ensemble Kalman filter applied to multiple-NO_2 and multiple-species measurements using two different CTMs. The intercomparison of all inventories shows good agreement in NO_x emissions over mainland China with an average bias of about 20 % for yearly emissions. All the inventories reveal common variability such as a typical emission reduction of 10 % during the Chinese New Year and a sharp peak in December. All the inventories show good agreement in spatial distribution on a provincial level ($R > 0.8$). However, biases in NO_x emissions and uncertainties in temporal (both yearly and monthly) variability become quickly higher when the spatial scale decreases. The emissions over urban areas in East Asia and show better agreement in the temporal and spatial variability between the different inventories than over rural areas. The coarse-resolution EnKF inventories show low temporal correlation with other inventories over rural areas, because they are unable to distinguish between urban and rural sources at small scale. All the satellite-derived inventories except for DECSO-GOME2a show a summer peak over mainland China. The summer peak could be related to enhanced emissions from soils and biomass burning in summer, for which OMI better captures the enhanced concentrations than GOME-2 due to their different overpass time. All the satellite-derived inventories, in particular DECSO-OMI, are lower than bottom-up inventories at higher latitudes (at above 40° N).

Based on our findings from the intercomparison of NO_x emission inventories, we come to the following recommendations for the development of NO_x emission inventories in the future:

- To better capture the temporal variability in emissions from the satellite-derived approach, observations from multiple instruments are important. In addition, a high-spatial-resolution model is necessary to distinguish between different emission sources and to better derive the emissions on a small spatial scale.

- Different bottom-up inventories use different definition of emission sector cat-

egories and with different assumption about the shares of the different technologies and high uncertainties in NO_x emission factors and activities. Better measurements of emissions factors and more detailed statistics on the activities not only per fuel but also per (combustion) technology are required.

- To take into account the advantages of bottom-up and satellite-derived approaches and to update near-real-time emissions, sector information from the bottom-up approach can be combined with the satellite-derived inventories. For instance, information on temporal changes of emissions from satellite-based calculations can be used for the temporal evolution of the bottom-up inventories.
- The satellite-derived approach can be further improved following the development of satellite instruments, like TROPOMI on Sentinel 5p and later the GEMS sensor on the geostationary GEO-KOMPSAT-2B. With higher spatial resolution of observations, more accurate emission over different land-use categories can be obtained. GEMS will provide observations with high temporal and spatial resolution, which enables the improvement of diurnal cycles for emission estimates.

Acknowledgements

The research was part of the OMI project funded and supported by the Netherlands Space Office. We acknowledge IPSL/LMD, INERIS and IPSL/LISA in France for providing the CHIMERE model. We acknowledge the use of tropospheric NO_2 column data obtained from www.temis.nl and the ESA GlobCover 2009 Project for the land-use dataset. We thank Henk Eskes and Folkert Boersma for their helpful suggestions.

6

Conclusions and outlook

NO_x and its secondary pollutants (O_3, nitrate aerosols, etc.) are regarded as major air pollutants. All of them are toxic and have a large impact on environment, air quality, human health and climate. Up-to-date emission information is essential for policy makers to provide efficient regulations for improving air quality. In addition, air quality simulations and forecasts need accurate emission data to drive a CTM.

During the last two decades, NO_x emissions have increased dramatically in East Asia due to the rapid economic development. Traditional bottom-up emission inventories are usually slowly updated with a time lag of at least one year. Large uncertainties of bottom-up inventories and of spatial and temporal distributions are caused by the lack of information on emission activities, such as small sources in remote regions. Since NO_2 has strong absorption features in the visible spectrum, satellite instruments such as OMI and GOME2 are able to capture well the tropospheric NO_2 column concentration. Satellite observations have been used to study and explain the temporal variation and spatial distribution of NO_2. NO_x emissions can be constrained by using inversion techniques applied to satellite observations to improve emission estimates.The Kalman filter is an optimization technique combining model forecasts with observations to give the optimal estimates of the state variable including an uncertainties analysis. DECSO is a fast inversion algorithm, which combines simulations from a CTM and satellite observations to derive emissions based on an extended Kalman filter. The algorithm is flexible with the choice of model and satellite observations.

In this dissertation, the research is aimed at the development and verification of NO_x emission estimates by using satellite observations based on the DECSO algorithm. The quality of emissions derived with the algorithm is highly related to three aspects: the quality of the model, the quality of the satellite observations, and the treatment of error covariances in the Kalman filter. We further developed DECSO focusing on these three aspects and verified each improvement via different case studies. The intercomparison of NO_x emissions from both bottom-up and satellite-derived approaches demonstrates the merit of our emission estimates.

6.1. The sensitivity of DECSO on the CTM and satellite observations

In DECSO, the role of a CTM is to convert emissions to concentrations in order to compare the simulated column concentrations with observations. A CTM with good performance is essential for the DECSO results. An outdated model of CHIMERE 2006 was used in the first version of DECSO, which had problems in simulating surface NO_2 concentrations especially during nighttime due to the extremely low boundary layer height in the model. To achieve a better model performance, we replaced CHIMERE 2006 by the newer version CHIMERE v2013b in DECSO. As a result, the surface NO_x concentrations simulated by the new version are in better agreement with in situ and satellite observations than by the old one.

The results of DECSO are also highly affected by the quality of satellite observations. The observations can suffer from biases in scenes with high aerosol concentrations (Lin et al., 2014; Kuhlmann et al., 2015; Chimot et al., 2016). High aerosol concentrations affect the NO_2 retrieval non-linearly and leads to either under- or over- estimation in NO_2 columns. In the DECSO results, some suspicious fluctuations in NO_x emissions appear on particular days when the aerosol concentrations are high in China. The DOMINO retrieval does not account for scenes with high aerosol loads. Therefore, large differences between the model simulations and the retrievals occur under these conditions of high aerosol concentrations. The differences lead to wrong updates of NO_x emissions. To solve this issue, we set up an OmF (observation minus forecast) criterion with a limitation to the range -5×10^{15} to 10×10^{15} molecules cm^{-2}. After filtering out erroneous observations with this criterion, unrealistic updates of NO_x emissions are mostly prevented in DECSO.

With the implementation of the two above improvements, we refer to the new DECSO algorithm as DECSO v3b. We selected the 2014 Youth Olympic Games (YOG) held in Nanjing as a case study to verify the improvements. NO_x emissions

were expected to be reduced during the YOG since the local government implemented strict air quality regulations to ensure good air quality during the Games. Satellite observations from OMI showed a decrease of 32 % of the NO_2 column concentrations during the YOG period compared to the averaged value for the last ten years. During the YOG, we see that NO_x emissions of DECSO v3b decreased by at least 25 % compared with emissions of the previous year and compared with the neighbouring months. This confirmed that the reduction of NO_2 concentrations is not only due to the rainy weather during the Olympic month but also due to emission control. Meanwhile, we also see a reduction of NO_x emissions of about 10 % during the Chinese New Year (also known as the Spring Festival). This reduction is consistent with other studies for China (Q. Zhang et al., 2009; McElroy, 2011; Wang et al. 2011). The NO_x emissions derived by DECSO have an opposite seasonal cycle compared to the NO_2 columns in Nanjing. The seasonal cycle in Nanjing derived with DECSO is quite different compared to those of bottom-up inventories such as INTEX-B. Cities like Nanjing, located in the southern part of China, have a high electricity consumption in summer time due to the increasing usage of air conditioning while having no central heating systems in winter. This situation is normally not considered in older bottom-up inventories due to the lack of detailed information on city level. With this case study, we demonstrate that DECSO v3b is able to estimate NO_x emissions on a spatial resolution of about 50 ×90 km^2 and has the capability to capture changes on a monthly scale. We showed that emission changes derived by DECSO can be used to quantify the effect of air quality regulations.

6.2. Improvements in the application of the extended Kalman filter in DECSO

From the results of DECSO v3b, we still see relatively high emissions with an artificial seasonal cycle over remote ocean areas where emissions are supposed to be close to zero. These erroneous emissions are referred to as background noise. Because the CTM cannot deal with negative emissions, the random negative emissions derived from the measurements were set to zero. To compensate the negative biases, we subtracted them from nearby positive emissions to keep the mass balance. This leads to background noise especially over low-emission areas. Weak sources like shipping or biogenic emissions are difficult to distinguish from the high background noise. The main objective in Chapter 4 was to reduce the background noise and detect emission sources over remote areas.

To solve the negative emission estimates, using logarithmic values is a valid approach, which has been used by Brunner et al. (2012). However, we find that

the results of this logarithmic method are not ideal for NO_x emission estimates with DECSO because it causes a positive bias over low emission areas as low emissions decrease slower than they are increasing in this method. Alternatively, we have improved the sensitivity matrix (**H**) and its covariance to solve the problem. The key part in DECSO is the calculation of the Jacobian matrix **H** of the observation operator, which translates gridded emissions to column concentrations in a satellite pixel. A minimum threshold is used for values of the **H** matrix elements to reduce the uncertainty caused by the edge of the plume. We increase the threshold from 0.05 h to 0.1 h based on several tests using different threshold values. The error covariances of the operator together with the covariances of the emission estimates propagated into the simulated column concentrations are essential to determine the update of the emission. The study of the OmF statistics for monthly and yearly periods showed a direct linear relation between the diagonal elements of error covariances and the NO_2 columns.

With the improvement of the error covariances, the background noise is significantly reduced by 90 % and the artificial seasonal cycle disappeared. The shipping emissions became clearly visible against the lower background values. An emission update constraint of 3σ is applied to replace the OmF filter criterion. With this constraint, emission updates become faster since 10 % more satellite observations are used. We verified that the emission update constraint is better than the original OmF filter by checking the flat seasonality of NO_x emissions in Hongkong, where the dominant emissions are from vehicles. Additionally, we switched off the biogenic emissions in the CHIMERE model to estimate total surface emissions instead of only anthropogenic emissions. Over half the study domain is covered by vegetation. Soil emissions are one of the main sources. The biogenic emissions generated with the MEGAN model have high uncertainties of about 300 % (Guenther et al., 2006, 2012). This leads to large uncertainties in anthropogenic emissions derived with DECSO, especially over remote areas.

The latest version of DECSO is version 5 (DECSO v5) were all improvements mentioned above are implemented. The precision of the derived emissions by DECSO v5 is about 20 % for each grid cell. The provincial monthly emissions have a much better precision of less than 2 %. Model simulations with DECSO v5 show a better agreement with OMI observations in wintertime. This indicates a better seasonal cycle of emission estimates. The comparison of DECSO v5 emissions with the MIX inventory (Li et al., 2017) shows a good agreement on spatial distribution and seasonality in the by anthropogenic emissions dominated provinces. In the provinces with high biomass burning emissions in summer, DECSO v5 is able to detect a summer peak, while those emissions were usually underestimated in China (Stavrakou et al., 2016). The ship tracks near Chinese coasts are also revealed in

the DECSO v5 results. It is the first time that shipping emissions for this region are derived using satellite observations. The magnitude of the shipping emissions is in agreement with studies over other shipping lanes with similar ship density.

6.3. Application of improved DECSO: long record of maritime emissions

Shipping emissions along the coast of China are difficult to see by satellite observations since they are hidden under the outflow of NO_2 plumes from the mainland. Our model simulations show that shipping emissions have a significant impact on local NO_2 concentrations at the densely populated coast, with contributions of 5-20 %. However, shipping emission data over China are usually not available. This leads to large uncertainties in air quality simulations and forecasts especially near coast areas. Earlier methods using satellite observations to derive shipping emissions either do not account for transport or have a coarse resolution. In DECSO, the influence of transport has been taken into account. By using a regional CTM with a relatively high resolution of $0.25^\circ \times 0.25^\circ$ combined with high-resolution satellite observations from OMI, shipping emissions near the coasts are visible in the DECSO results after applying the improvements conducted in this thesis.

We are able to present the first long-term record (from 2007 to 2016) of satellite-derived NO_x emissions over Chinese seas. The maritime emissions, which are from offshore platforms and ships, have a continuous increase rate of about 20 % per year until 2012 and slow down to about 3 % afterwards. This trend is consistent with the trend of cargo throughput in the Chinese main harbours. The trend of NO_x emissions over sea is quite different from that over the mainland, which is decreasing since 2012 (van der A et al., 2017). The continuous trend of NO_x emissions over sea indicates that no effective NO_x control has been implemented for ships in China. The seasonal cycle of shipping emissions has regional variations but all regions show lower emissions during winter. The regional variations can have several reasons: gradually northward movement of the summer monsoon, increase of tourism activities, and different moratorium periods of fishing over the regions. The maritime NO_x emissions derived with DECSO are comparable with shipping inventories from Fan et al. (2016), Liu et al. (2016) and Johansson et al. (2017) based on AIS data.

6.4. Validation of emission estimates from satellite observations

The validation of emissions over a large domain is a great challenge. Direct validation is not possible due to the lack of independent emission measurements on the ground. To investigate the uncertainties in NO_x emission estimates over East Asia, we have compared 4 satellite-derived NO_x emission inventories with a comprehensive collection of regional bottom-up inventories for East Asia: REAS v2.1 and an interim version of 2.2, MEIC, CAPSS and EDGAR v4.3.1. The intercomparison shows good agreement in yearly NO_x emissions among all emission inventories over mainland China with an average bias of about 20 %, which is below the range of the typical uncertainty of 31-37 % for bottom-up inventories (Li et al., 2017). The spatial distribution of each inventory is also in good agreement on a provincial level. However, discrepancies in NO_x emissions and uncertainties in temporal (both yearly and monthly) variability become quickly higher when the spatial scale decreases.

The reasons for the differences among the nine inventories have been discussed in Chapter 5.4. In the bottom-up inventories, the differences in emission activity and emission factors of each emission sector can lead to large discrepancies. In the satellite-derived inventories, the deviations are introduced by differences in inversion techniques, chemical transport models, and observations.

A detailed analysis for satellite-derived emissions has been done for the 3 following aspects on both temporal and spatial scales:

1. Evaluation of two different inversion techniques, namely DECSO (extended Kalman filter) and EnKF (ensemble Kalman filter)

2. The dependence on model performance in the satellite-derived approach. The emission datasets from EnKF have been derived using the CTM CHASER or MIROC.

3. The effect of different satellite instruments in the satellite-derived approach. DECSO has been applied to both GOME-2 and OMI observations.

In DECSO, emissions are only constrained by NO_2 observations from one instrument, while in EnKF the emissions are obtained by assimilating multiple species, which provide constraints on various aspects of the tropospheric chemistry system and improve the NO_x emission estimates. However, DECSO inventories show higher temporal correlations with other inventories especially over rural areas. This

can be explained by the usage of a CTM with a higher spatial resolution. The seasonality of NO_x emissions is highly affected by biogenic emissions. The inventories including biogenic emissions all show a summer peak except the DECSO-GOME2 dataset. This indicates that the seasonality derived with DECSO is affected by the use of different satellite observations. This can be explained by the differences in the satellite overpass time and uncertainty in modelled diurnal variations. Because of stronger biomass burning activities and high soil emissions in the afternoon, more NO_2 from biomass burning is observed by the OMI satellite instrument with an afternoon overpass time than the GOME-2 instrument with its morning overpass time (Boersma et al., 2008). The dependency of the satellite-derived emissions on model performance is also very important. Not only in DECSO (shown in Chapter 2), but also in EnKF (shown in Chapter 5). By using different CTMs, the two EnKF datasets result in a bias of about 15 % for the annual total emissions over East Asia.

6.5. Outlook

Satellite-derived emissions reveal more specific information on the location and strength of sources than concentration observations. Our recent satellite-derived emissions are able to show small sources, which are otherwise hidden under the outflow of NO_2 plumes from more polluted regions. For example, maritime emissions along the Chinese coast can be clearly seen in our satellite-derived emission map. Due to the high temporal and spatial resolution of satellite observations, the monthly and yearly variability are well captured in satellite-derived emissions. DECSO is a very fast algorithm, which enables daily emission estimates as soon as the satellite observations are available, which is demonstrated by our monitoring of the effect of air quality regulations on emissions during events like the 2014 Youth Olympic Games. The results of our intercomparison between bottom-up and satellite-derived inventories have demonstrated the quality of the emissions estimated with DECSO.

In the future, the inversion techniques can be further improved. One known issue is that the different seasonal cycles from DECSO applied to OMI and GOME2 indicate a high dependency on the choice of satellite observations and uncertainties in the diurnal cycle simulated by the CTM. We can combine observations from multiple instruments obtained at different overpass times to better capture NO_x emissions. In addition, the typical slow response time of the extended Kalman filter in DECSO can be improved by switching to a smoothing Kalman filter, although this will slow down the processing of DECSO.

Another option is to increase the resolution of DECSO, but we noticed during our

research that this requires high-resolution observations on either spatial or temporal scale. With the development of new satellite instruments, a possible resolution increase for DECSO will become effective and feasible. For example, observations from TROPOMI may help us to better detect small sources like low-density ship tracks since it has a high spatial resolution of 7 km ×3.5 km at nadir. Observations from geostationary satellite instruments (e.g. GEMS over Asia, Sentinel-4 over Europe, and TEMPO over America) enables the improvement of the diurnal cycle in emission estimates since these new geostationary satellites will observe NO_2 concentrations with time steps of at least one hour during daytime.

In this thesis, we analysed only the NO_x emission results of DECSO applied to East Asia. However, DECSO can easily be applied to other regions as well, for example Europe, which we have done for the GlobEmission project. In this project, we also studied the inversion of SO2. Short-lived species, not only SO_2 but also NH_3 and HCHO, can be derived by further development of DECSO. In addition, emission inventories can be further improved by combining information of bottom-up inventories with up-to-date total emissions derived from satellite observations. For instance, information on new emission sources and temporal changes of satellite-derived emissions can be used for improving the spatial distribution and the temporal evolution of the bottom-up inventories. We can also directly contribute to climate studies by deriving CO_2 emission maps for shipping by applying the ratio between CO_2 and NO_x obtained from bottom-up studies to our NO_x emissions.

Appendix

Calculation of the NO_2 concentration from the Air Quality Index

The formula to calculate the NO_2 concentration from the Air Quality Index (AQI) is according the piecewise linear function:

$$C = \frac{I - I_{low}}{I_{high} - I_{low}} \left(C_{high} - C_{low}\right) + C_{low}$$

where C is the NO_2 concentration; I is the AQI; C_{low} is the concentration breakpoint, which is lower than C; C_{high} is the concentration breakpoint, which is higher than C; I is the index breakpoint corresponding to C_{low}; I_{high} is the index breakpoint corresponding to C_{high}.

The Air Quality Index (AQI) with the corresponding NO_2 concentration breakpoints.

Air Quality Index (I)	NO_2 hourly mean (C) (μm^{-3})
0	0
50	100
100	200
150	700
200	1200
300	2340
400	3090
500	3840

References

Abbey, D. E., Nishino, N., McDonnell, W. F., Burchette, R. J., Knutsen, S. F., Beeson, W. L., and Wang, J. X.: Long-Term Inhalable Particles and Other Air Pollutants Related to Mortality in Nonsmokers, American Journal of Respiratory and Critical Care Medicine, 159, 373-382,http://doi.org/10.1164/ajrccm.159.2.9806020, 1999.

Acarreta, J. R., De Haan, J. F., and Stammes, P.: Cloud pressure retrieval using the O_2-O_2 absorption band at 477 nm, J. Geophys. Res., 109, D05204, http://dx.doi.org/10.1029/2003JD003915, 2004.

Akimoto, H. and Narita, H.: Distribution of SO_2, NO_x and CO_2 emissions from fuel combustion and industrial activities in Asia with $1^\circ \times 1^\circ$ resolution, Atmos. Environ., 28, 213–225, https://doi.org/10.1016/1352-2310(94)90096-5, 1994.

Akiyama, H., Tsuruta, H., and Watanabe, T.: N_2O and NO emissions from soils after the application of different chemical fertilizers, Chemosphere - Global Change Science, 2, 313-320,http://dx.doi.org/10.1016/S1465-9972(00)00010-6, 2000.

Beirle, S., Platt, U., von Glasow, R., Wenig, M., and Wagner, T.: Estimate of nitrogen oxide emissions from shipping by satellite remote sensing, Geophys. Res. Lett., 31, L18102, http://dx.doi.org/10.1029/2004GL020312, 2004.

Bessagnet, B., Hodzic, A., Vautard, R., Beekmann, M., Cheinet, S.,Honoré, C., Liousse, C., and Rouil, L.: Aerosol modeling with CHIMERE – preliminary evaluation at the continental scale, Atmos. Environ., 38, 2803–2817, http://dx.doi.org/10.1016/j.atmosenv.2004.02.034, 2004.

Blond, N., Boersma, K. F., Eskes, H. J., van der A, R. J., Van Roozendael, M., De Smedt, I., Bergametti, G., and Vautard, R.: Intercomparison of SCIAMACHY nitrogen dioxide observations, in situ measurements and air quality modeling results over Western Europe, J. Geophys. Res., 112, 1–20, http://dx.doi.org/10.1029/2006JD007277, 2007.

Boersma, K. F., Eskes, H. J., and Brinksma, E. J.: Error analysis for tropospheric NO_2 retrieval from space, J. Geophys. Res., 109, D04311, http://dx.doi.org/10.1029/2003JD003962, 2004.

Boersma, K. F., Eskes, H. J., Veefkind, J. P., Brinksma, E. J., van der A, R. J., Sneep, M., van den Oord, G. H. J., Levelt, P. F., Stammes, P., Gleason, J. F., and Bucsela, E. J.: Near-real time retrieval of tropospheric NO_2 from OMI, Atmos. Chem. Phys., 7, 2103–2118, http://dx.doi.org/10.5194/acp-7-2103-2007, 2007.

Boersma, K. F., Jacob, D. J., Eskes, H. J., Pinder, R. W., Wang, J., and van der A, R. J.: Intercomparison of SCIAMACHY and OMI tropospheric NO_2 columns: Observing the diurnal evolution of chemistry and emissions from space, J. Geophys. Res., 113, D16S26, http://dx.doi.org/10.1029/2007JD008816, 2008.

Boersma, K. F., Jacob, D. J., Trainic, M., Rudich, Y., DeSmedt, I., Dirksen, R., and Eskes, H. J.: Validation of urban NO_2 concentrations and their diurnal and seasonal variations observed from the SCIAMACHY and OMI sensors using in situ surface measurements in Israeli cities, Atmos. Chem. Phys., 9, 3867–3879, http://dx.doi.org/10.5194/acp-9-3867-2009, 2009.

Boersma, K. F., Eskes, H. J., Dirksen, R. J., van der A, R. J., Veefkind, J. P., Stammes, P., Huijnen, V., Kleipool, Q. L., Sneep, M., Claas, J., Leitão, J., Richter, A., Zhou, Y., and Brunner, D.: An improved tropospheric NO_2 column retrieval algorithm for the Ozone Monitoring Instrument, Atmos. Meas. Tech., 4, 1905-1928, http://dx.doi.org/10.5194/amt-4-1905-2011, 2011.

Bovensmann, H., Burrows, J. P., Buchwitz, M., Frerick, J., Noël, S., Rozanov, V. V., Chance, K. V., and Goede, A. P. H.: SCIAMACHY: Mission Objectives and Measurement Modes, J. Atmos. Sci., 56, 127–150, http://dx.doi.org/10.1175/1520-0469(1999)0560127:SMOAMM2.0.CO;2, 1999.

Bouarar, I., X. Wang, and G. P. Brasseur.: Chapter 3 in Air Pollution in Eastern Asia: An Integrated Perspective, XI, 504 pp., Springer International Publishing, http://dx.doi.org/10.1007/978-3-319-59489-7, 2017

Bouwman, A. F., Boumans, L. J. M., and Batjes, N. H.: Modeling global annual N_2O and NO emissions from fertilized fields, Global Biogeochem. Cy., 16, 1080, http://dx.doi.org/10.1029/2001GB001812, 2002.

Brunner, D., Henne, S., Keller, C. A., Reimann, S., Vollmer, M. K., O'Doherty, S., and Maione, M.: An extended Kalman-filter for regional scale inverse emission estimation, Atmos. Chem. Phys., 12, 3455–3478, http://dx.doi.org/10.5194/acp-12-3455-2012, 2012.

Burke, C. and Stott, P.: Impact of Anthropogenic Climate Change on the East Asian Summer Monsoon, Journal of Climate, 30, http://dx.doi.org/10.1175/jcli-d-16-0892.15205-5220, 2017.

Castellanos, P., Boersma, K. F., and van der Werf, G. R.: Satellite observations indicate substantial spatiotemporal variability in biomass burning NO_x emission factors for South America, Atmos. Chem. Phys., 14, 3929–3943, http://dx.doi.org/10.5194/acp-14-3929-2014, 2014.

Chan, C. and Yao, X.: Air pollution in mega cities in China, Atmos. Environ., 42, 1–42, http://dx.doi.org/10.1016/j.atmosenv.2007.09.003, 2008.

Chimot, J., Vlemmix, T., Veefkind, J. P., de Haan, J. F., and Levelt, P. F.: Impact of aerosols on the OMI tropospheric NO_2 retrievals over industrialized regions: how accurate is

the aerosol correction of cloud-free scenes via a simple cloud model?, Atmos. Meas. Tech., 9, 359–382, http://dx.doi.org/10.5194/amt-9-359-2016, 2016.

Corbett, J. J., Fischbeck, P. S., and Pandis, S. N.: Global nitrogen and sulfur inventories for oceangoing ships, Journal of Geophysical Research: Atmospheres, 104, 3457-3470, http://dx.doi.org/10.1029/1998JD100040, 1999.

Corbett, J. J., and H. W. Koehler, Updated emissions from ocean shipping, Journal of Geophysical Research: Atmospheres, 108(D20), http://dx.doi.org/10.1029/2003JD003751, 2003

Crippa, M., Janssens-Maenhout, G., Dentener, F., Guizzardi, D., Sindelarova, K., Muntean, M., Van Dingenen, R., and Granier, C.: Forty years of improvements in European air quality: regional policy-industry interactions with global impacts, Atmos. Chem. Phys., 16, 3825-3841, http://dx.doi.org/10.5194/acp-16-3825-2016, 2016.

Cui, F., Yan, G., Zhou, Z., Zheng, X., and Deng, J.: Annual emissions of nitrous oxide and nitric oxide from a wheat–maize cropping system on a silt loam calcareous soil in the North China Plain, Soil Biol. Biochem., 48, 10–19, 2012.

Dee, D. P., Uppala, S. M., Simmons, A. J., Berrisford, P., Poli, P., Kobayashi, S., Andrae, U., Balmaseda, M. A., Balsamo, G., Bauer, P., Bechtold, P., Beljaars, A. C. M., van de Berg, L., Bidlot, J., Bormann, N., Delsol, C., Dragani, R., Fuentes, M., Geer, A. J., Haimberger, L., Healy, S. B., Hersbach, H., Hólm, E. V., Isaksen, L., Kållberg, P., Köhler, M., Matricardi, M., McNally, A. P., Monge-Sanz, B. M., Morcrette, J. J., Park, B. K., Peubey, C., de Rosnay, P., Tavolato, C., Thépaut, J. N., and Vitart, F.: The ERA-Interim reanalysis: configuration and performance of the data assimilation system, Q. J. Roy. Meteor. Soc., 137, 553–597, http://dx.doi.org/10.1002/qj.828, 2011.

De Foy, B., Lu, Z., and Streets, D. G.: Satellite NO_2 retrievals suggest China has exceeded its NO_x reduction goals from the twelfth Five-Year Plan, Scientific Reports, 6, 35912, http://dx.doi.org/10.1038/srep35912, 2016.

De Ruyter de Wildt, M., Eskes, H., and Boersma, K. F.: The global economic cycle and satellite-derived NO_2 trends over shipping lanes, Geophysical Research Letters, 39, L01802, http://doi.org/10.1029/2011GL049541, 2012.

Ding, J., van der A, R. J., Mijling, B., Levelt, P. F., and Hao, N.: NO_x emission estimates during the 2014 Youth Olympic Games in Nanjing, Atmos. Chem. Phys., 15, 9399-9412, http://doi.org/10.5194/amt-10-925-2017, 2015.

Ding, J., van der A, R. J., Mijling, B., and Levelt, P. F.: Space-based NO_x emission estimates over remote regions improved in DECSO, Atmos. Meas. Tech., 10, 925-938, http://doi.org/10.5194/amt-10-925-2017, 2017.

Ebenstein, A., Fan, M., Greenstone, M., He, G., and Zhou, M.: New evidence on the impact of sustained exposure to air pollution on life expectancy from China's Huai River Policy, Proceedings of the National Academy of Sciences, http://doi.org/10.1073/pnas.1616784114, 2017.

Eder, B., Kang, D., Mathur, R., Pleim, J., Yu, S., Otte, T., and Pouliot, G.: A performance evaluation of the National Air Quality Forecast Capability for the summer of 2007, Atmospheric Environment, 43, 2312-2320, http://dx.doi.org/10.1016/j.atmosenv.2009.01.033, 2009.

Evensen, G.: The Ensemble Kalman Filter: theoretical formulation and practical implementation, Ocean Dynam., 53, 343–367, http://dx.doi.org/10.1007/s10236-003-0036-9, 2003.

Eyring, V., Isaksen, I. S. A., Berntsen, T., Collins, W. J., Corbett, J. J., Endresen, O., Grainger, R. G., Moldanova, J., Schlager, H., and Stevenson, D. S.: Transport impacts on atmosphere and climate: Shipping, Atmospheric Environment, 44, 4735-4771, http://doi.org/10.1016/j.atmosenv.2009.04.059, 2010.

FAO: Food and Agricultural Organization of the United Nations: Statistics Division, Livestock, Crop and Fertilizer data, available at: http://www.fao.org/docrep/015/i2490e/i2490e00.htm (last access: October 2016), 2012.

Fan, Q., Zhang, Y., Ma, W., Ma, H., Feng, J., Yu, Q., Yang, X., Ng, S. K. W., Fu, Q., and Chen, L.: Spatial and Seasonal Dynamics of Ship Emissions over the Yangtze River Delta and East China Sea and Their Potential Environmental Influence, Environ. Sci. Technol., 50, 1322–1329, http://doi.org/10.1021/acs.est.5b03965, 2016.

Finney, D. L., Doherty, R. M., Wild, O., Young, P. J., and Butler, A.: Response of lightning NO_x emissions and ozone production to climate change: Insights from the Atmospheric Chemistry and Climate Model Intercomparison Project, Geophysical Research Letters, 43, 5492-5500, http://doi.org/10.1002/2016GL068825, 2016.

Franke, K., Richter, A., Bovensmann, H., Eyring, V., Jöckel, P., Hoor, P., and Burrows, J. P.: Ship emitted NO_2 in the Indian Ocean: comparison of model results with satellite data, Atmos. Chem. Phys., 9, 7289–7301, http://dx.doi.org/10.5194/acp-9-7289-2009, 2009.

Ghude, S. D., Lal, D. M., Beig, G., van der A, R., and Sable, D.: Rain-Induced Soil NO_x Emission From India During the Onset of the Summer Monsoon: A Satellite Perspective, J. Geophys. Res.-Atmos., 115, D16304, http://dx.doi.org/10.1029/2009JD013367, 2010.

Giglio, L., Randerson, J. T., and van der Werf, G. R.: Analysis of daily, monthly, and annual burned area using the fourth-generation global fire emissions database (GFED4), J. Geophys. Res.-Biogeo., 118, 317–328, http://dx.doi.org/10.1002/jgrg.20042, 2013.

Granier, C., Bessagnet, B., Bond, T., D' Angiola, A., Denier van der Gon, H., Frost, G. J., Heil, A., Kaiser, J. W., Kinne, S., Klimont, Z., Kloster, S., Lamarque, J.-F., Liousse, C., Masui, T., Meleux, F., Mieville, A., Ohara, T., Raut, J.-C., Riahi, K., Schultz, M. G., Smith, S. J., Thompson, A., van Aardenne, J., van der Werf, G. R., and van Vuuren, D. P.: Evolution of anthropogenic and biomass burning emissions of air pollutants at global and regional scales during the 1980–2010 period, Climatic Change, 109, 163, http://dx.doi.org/10.1007/s10584-011-0154-1, 2011.

Guenther, A., Karl, T., Harley, P., Wiedinmyer, C., Palmer, P. I., and Geron, C.: Estimates of global terrestrial isoprene emissions using MEGAN (Model of Emissions of Gases and Aerosols from Nature), Atmos. Chem. Phys., 6, 3181–3210, http://dx.doi.org/10.5194/acp-6-3181-2006, 2006.

Guenther, A. B., Jiang, X., Heald, C. L., Sakulyanontvittaya, T., Duhl, T., Emmons, L. K., and Wang, X.: The Model of Emissions of Gases and Aerosols from Nature version 2.1 (MEGAN2.1): an extended and updated framework for modeling biogenic emissions, Geosci. Model Dev., 5, 1471–1492, http://dx.doi.org/10.5194/gmd-5-1471-2012, 2012.

Gu, D., Wang, Y., Smeltzer, C., and Liu, Z.: Reduction in NO_x Emission Trendsover China: Regional and Seasonal Variations, Environ. Sci. Technol., 47, 12912–12919, http://dx.doi.org/10.1021/es401727e, 2013.

Hao, N., Valks, P., Loyola, D., Cheng, Y. F., and Zimmer, W.: Space-based measurements of air quality during the World Expo 2010 in Shanghai, Environ. Res. Lett., 6, 044004, http://dx.doi.org/10.1088/1748-9326/6/4/044004, 2011.

He, M., Zheng, J., Yin, S., and Zhang, Y.: Trends, temporal and spatial characteristics, and uncertainties in biomass burning emissions in the Pearl River Delta, China, Atmos. Environ., 45, 4051–4059, http://dx.doi.org/10.1016/j.atmosenv.2011.04.016, 2011.

He, K.: Multi-resolution Emission Inventory for China (MEIC): model framework and 1990–2010 anthropogenic emissions, in: International Global Atmospheric Chemistry Conference, 17–21 September, Beijing, China, available at: http://adsabs.harvard.edu/abs/2012AGUFM.A32B..05H (last access: 4 February 2015), 2012.

Heckel, A., Kim, S.-W., Frost, G. J., Richter, A., Trainer, M., and Burrows, J. P.: Influence of low spatial resolution a priori data on tropospheric NO_2 satellite retrievals, Atmos. Meas. Tech., 4, 1805–1820, http://dx.doi.org/10.5194/amt-4-1805-2011, 2011.

Hong, C., Zhang, Q., He, K., Guan, D., Li, M., Liu, F., and Zheng, B.: Variations of China's emission estimates: response to uncertainties in energy statistics, Atmos. Chem. Phys., 17, 1227-1239, http://dx.doi.org/10.5194/acp-17-1227-2017, 2017.

Huang, X., Li, M., Li, J., and Song, Y.: A high-resolution emission inventory of crop burning in fields in China based on MODIS Thermal Anomalies/Fire products, Atmos. Environ., 50, 9–15, http://dx.doi.org/10.1016/j.atmosenv.2012.01.017, 2012.

Huijnen, V., Williams, J., van Weele, M., van Noije, T., Krol, M., Dentener, F., Segers, A., Houweling, S., Peters, W., de Laat, J., Boersma, F., Bergamaschi, P., van Velthoven, P., Le Sager, P., Eskes, H., Alkemade, F., Scheele, R., Nédélec, P., and Pätz, H.-W.: The global chemistry transport model TM5: description and evaluation of the tropospheric chemistry version 3.0, Geosci. Model Dev., 3, 445–473, http://dx.doi.org/10.5194/gmd-3-445-2010, 2010.

IMO: Third IMO Greenhouse Gas Study 2014, Micropress Printers, 2015 http://www.imo.org/en/OurWork/Environment/PollutionPrevention/AirPollution/Documents/ThirdGreenhouseGasStudy/GHG3ExecutiveSummaryandReport.pdf

Ingmann, P., Veihelmann, B., Langen, J., Lamarre, D., Stark, H., and Courrèges-Lacoste, G. B.: Requirements for the GMES Atmosphere Service and ESA's implementation concept: Sentinels-4/-5 and -5p, Remote Sensing of Environment, 120, 58-69,http://dx.doi.org/10.1016/j.rse.2012.01.023, 2012.

IPCC: Climate Change 2014: Impacts, Adaptation, and Vulnerability, Summaries, Frequently Asked Questions, and Cross-Chapter Boxes, A Contribution of Working Group II to the Fifth Assessment Report of the Intergovernmental Panel on Climate Change, edited by: Field, C. B., Barros, V. R., Dokken, D. J., Mach, K. J., Mastrandrea, M. D., Bilir, T. E., Chatterjee, M., Ebi, K. L., Estrada, Y. O., Genova, R. C., Girma, B., Kissel, E. S., Levy, A. N., MacCracken, S., Mastrandrea, P. R., and White, L. L., World Meteorological Organization, Geneva, Switzerland, 2014.

IEA: Energy Statistics of OECD Countries 2014, IEA, Paris, available at: http://dx.doi.org/10.1787/energy_stats_oecd-2014-en (last access: 23 August 2017), 2014a.

IEA: Energy Statistics of Non-OECD Countries 2014, IEA, Paris, available at: http://dx.doi.org/10.1787/energy_non-oecd-2014-en (last access: 23 August 2017), 2014b.

Irie, H., Sudo, K., Akimoto, H., Richter, A., Burrows, J. P., Wagner, T., Wenig, M., Beirle, S., Kondo, Y., Sinyakov, V. P., and Goutail, F.: Evaluation of long-term tropospheric NO_2 data obtained by GOME over East Asia in 1996–2002, Geophysical Research Letters, 32, http://dx.doi.org/10.1029/2005GL022770, 2005.

Irie, H., Boersma, K. F., Kanaya, Y., Takashima, H., Pan, X., and Wang, Z. F.: Quantitative bias estimates for tropospheric NO_2 columns retrieved from SCIAMACHY, OMI, and GOME-2 using a common standard for East Asia, Atmos. Meas. Tech., 5, 2403–2411, http://dx.doi.org/10.5194/amt-5-2403-2012, 2012.

Irie, H., Muto, T., Itahashi, S., Kurokawa, J.-i., and Uno, I.: Turnaround of Tropospheric Nitrogen Dioxide Pollution Trends in China, Japan, and South Korea, SOLA, 12, 170–174, http://dx.doi.org/10.2151/sola.2016-035, 2016.

Itahashi, S., Uno, I., Irie, H., Kurokawa, J.-I., and Ohara, T.: Regional modeling of tropospheric NO_2 vertical column density over East Asia during the period 2000–2010: comparison with multisatellite observations, Atmos. Chem. Phys., 14, 3623–3635, http://dx.doi.org/10.5194/acp-14-3623-2014, 2014.

Jacob, D. J., Heikes, E. G., Fan, S. M., Logan, J. A., Mauzerall, D. L., Bradshaw, J. D., Singh, H. B., Gregory, G. L., Talbot, R. W., Blake, D. R., and Sachse, G. W.: Origin of ozone and NO_x in the tropical troposphere: A photochemical analysis of aircraft observations over the South Atlantic basin, J. Geophys. Res., 101, 24235–24250, http://dx.doi.org/10.1029/96JD00336, 1996.

Jaeglé, L., Martin, R. V., Chance, K., Steinberger, L., Kurosu, T. P., Jacob, D. J., Modi, A. I., Yoboué, V., Sigha-Nkamdjou, L., and Galy-Lacaux, C.: Satellite mapping of rain-induced nitric oxide emissions from soils, J. Geophys. Res.-Atmos., 109, D21310, http://dx.doi.org/10.1029/2004JD004787, 2004.

Jaeglé, L., Steinberger, L., Martin, R. V., and Chance, K.: Global partitioning of NO_x sources using satellite observations: Relative roles of fossil fuel combustion, biomass burning and soil emissions, Faraday Discuss., 130, http://dx.doi.org/407--423,10.1039/B502128F, 2005.

Jain, A. K., Tao, Z., Yang, X., and Gillespie, C.: Estimates of global biomass burning emissions for reactive greenhouse gases (CO, NMHCs, and NO_x) and CO_2, Journal of Geophysical Research: Atmospheres, 111, http://doi.org/10.1029/2005JD006237, 2006.

Jalkanen, J. P., Brink, A., Kalli, J., Pettersson, H., Kukkonen, J., and Stipa, T.: A modelling system for the exhaust emissions of marine traffic and its application in the Baltic Sea area, Atmos. Chem. Phys., 9, 9209-9223, http://doi.org/10.5194/acp-9-9209-2009, 2009.

Jalkanen, J. P., Johansson, L., and Kukkonen, J.: A comprehensive inventory of ship traffic exhaust emissions in the European sea areas in 2011, Atmos. Chem. Phys., 16, 71-84, http://doi.org/10.5194/acp-16-71-2016, 2016.

Janssens-Maenhout, G., Crippa, M., Guizzardi, D., Dentener, F., Muntean, M., Pouliot, G., Keating, T., Zhang, Q., Kurokawa, J., Wankmüller, R., Denier van der Gon, H., Kuenen, J. J. P., Klimont, Z., Frost, G., Darras, S., Koffi, B., and Li, M.: HTAP _ v2.2: a mosaic of regional and global emission grid maps for 2008 and 2010 to study hemispheric transport of air pollution, Atmos. Chem. Phys., 15, 11411-11432, http://doi.org/10.5194/acp-15-11411-2015, 2015.

Janssens-Maenhout, G., Pagliari, V., Guizzardi, D., and Muntean, M.: Global emission inventories in the Emission Database for Global Atmospheric Research (EDGAR) – Manual (I): Gridding: EDGAR emissions distribution on global gridmaps, JRC Technical Reports, 33 pp., http://dx.doi.org/10.2788/81454, 2013.

Kampa, M., and Castanas, E.: Human health effects of air pollution, Environmental Pollution, 151, 362-367,http://dx.doi.org/10.1016/j.envpol.2007.06.012, 2008.

Kan, H., Chen, B., and Hong, C.: Health Impact of Outdoor Air Pollution in China: Current Knowledge and Future Research Needs, Environmental Health Perspectives, 117, A187-A187, http://doi.org/10.1289/ehp.12737, 2009.

Kan, H., Chen, R., and Tong, S.: Ambient air pollution, climate change, and population health in China, Environment International, 42, 10-19, http://dx.doi.org/10.1016/j.envint.2011.03.003, 2012.

Kanamitsu, M., Ebisuzaki, W., Woollen, J., Yang, S.-K., Hnilo, J. J., Fiorino, M., and Potter, G. L.: NCEP–DOE AMIP-II Reanalysis (R-2), B. Am. Meteorol. Soc., 83, 1631–1643, http://dx.doi.org/10.1175/bams-83-11-1631, 2002.

Kim, J.: GEMS(Geostationary Environment Monitoring Spectrometer) onboard the GeoKOMPSAT to Monitor Air Quality in high Temporal and Spatial Resolution over Asia-Pacific Region, paper presented at EGU, Vienna, Austria, 22-27 April, 2012.

KNMI: Background information about the Row Anomaly in OMI, available at: http://projects.knmi.nl/omi/research/product/rowanomaly-background (last access: 7 September 2016), 2012.

Konovalov, I. B., Beekmann, M., Richter, A., and Burrows, J. P.: Inverse modelling of the spatial distribution of NO_x emissions on a continental scale using satellite data, Atmos. Chem. Phys., 6, 1747-1770, http://doi.org/10.5194/acp-6-1747-2006, 2006.

Kroon, M., de Haan, J. F., Veefkind, J. P., Froidevaux, L., Wang, R., Kivi, R., and Hakkarainen, J. J.: Validation of operational ozone profiles from the Ozone Monitoring Instrument, J. Geophys. Res., 116, D18305, http://dx.doi.org/10.1029/2010JD015100, 2011.

Krotkov, N. A., McLinden, C. A., Li, C., Lamsal, L. N., Celarier, E. A., Marchenko, S. V., Swartz, W. H., Bucsela, E. J., Joiner, J., Duncan, B. N., Boersma, K. F., Veefkind, J. P., Levelt, P. F., Fioletov, V. E., Dickerson, R. R., He, H., Lu, Z., and Streets, D. G.: Aura OMI observations of regional SO_2 and NO_2 pollution changes from 2005 to 2015, Atmos. Chem. Phys., 16, 4605–4629, http://dx.doi.org/10.5194/acp-16-4605-2016, 2016.

Kuhlmann, G., Lam, Y. F., Cheung, H. M., Hartl, A., Fung, J. C. H., Chan, P. W., and Wenig, M. O.: Development of a custom OMI NO_2 data product for evaluating biases in a regional chemistry transport model, Atmos. Chem. Phys., 15, 5627–5644, http://dx.doi.org/10.5194/acp-15-5627-2015, 2015.

Kurokawa, J.., Yumimoto, K., Uno, I., and Ohara, T.: Adjoint inverse modeling of NO_x emissions over eastern China using satellite observations of NO_2 vertical column densities, Atmospheric Environment, 43, 1878-1887, http://dx.doi.org/10.1016/j.atmosenv.2008.12.030, 2009.

Kurokawa, J., Ohara, T., Morikawa, T., Hanayama, S., Janssens-Maenhout, G., Fukui, T., Kawashima, K., and Akimoto, H.: Emissions of air pollutants and greenhouse gases over Asian regions during 2000 – 2008: Regional Emission inventory in ASia (REAS) version 2, Atmos. Chem. Phys., 13, 11019-11058, http://doi.org/10.5194/acp-13-11019-2013, 2013.

Kwok, R. H. F., Fung, J. C. H., Lau, A. K. H., and Fu, J. S.: Numerical study on seasonal variations of gaseous pollutants and particulate matters in Hong Kong and Pearl River Delta Region, J. Geophys. Res.-Atmos., 115, D21310, http://dx.doi.org/10.1029/2004JD004787, 2010.

Lamarque, J. F., Bond, T. C., Eyring, V., Granier, C., Heil, A., Klimont, Z., Lee, D., Liousse, C., Mieville, A., Owen, B., Schultz, M. G., Shindell, D., Smith, S. J., Stehfest, E., Van Aardenne, J., Cooper, O. R., Kainuma, M., Mahowald, N., McConnell, J. R., Naik, V., Riahi, K., and van Vuuren, D. P.: Historical (1850–2000) gridded anthropogenic and biomass burning emissions of reactive gases and aerosols: methodology and application, Atmos. Chem. Phys., 10, 7017-7039, http://doi.org/10.5194/acp-10-7017-2010, 2010.

Lamsal, L. N., Martin, R. V., Padmanabhan, A., van Donkelaar, A., Zhang, Q., Sioris, C. E., Chance, K., Kurosu, T. P., and Newchurch, M. J.: Application of satellite observations for timely updates to global anthropogenic NO_x emission inventories, Geophys. Res. Lett., 38, L05810, http://dx.doi.org/10.1029/2010GL046476, 2011.

Lawrence, M. G. and Crutzen, P. J.: Influence of NO_x emissions from ships on tropospheric photochemistry and climate, Nature, 402, 167-170, http://dx.doi.org/10.1038/46013 1999.

Laughner, J. L., Zare, A., and Cohen, R. C.: Effects of daily meteorology on the interpretation of space-based remote sensing of NO_2, Atmos. Chem. Phys., 16, 15247-15264, http://dx.doi.org/10.5194/acp-16-15247-2016, 2016.

Lee, D., Lee, Y.-M., Jang, K.-W., Yoo, C., Kang, K.-H., Lee, J.-H., Jung, S.-W., Park, J.-M., Lee, S.-B., Han, J.-S., Hong, J.-H., and Lee, S.-J.: Korean National Emissions Inventory System and 2007 Air Pollutant Emissions, Asian Journal of Atmospheric Environment, 5, 278–291, http://dx.doi.org/10.5572/ajae.2011.5.4.278, 2011.

Leitão, J., Richter, A., Vrekoussis, M., Kokhanovsky, A., Zhang, Q. J., Beekmann, M., and Burrows, J. P.: On the improvement of NO_2 satellite retrievals – aerosol impact on the airmass factors, Atmos. Meas. Tech., 3, 475–493, http://dx.doi.org/10.5194/amt-3-475-2010, 2010.

Leue, C., Wenig, M., Wagner, T., Klimm, O., Platt, U., and Jähne, B.: Quantitative analysis of NO x emissions from Global Ozone Monitoring Experiment satellite image sequences, Journal of Geophysical Research: Atmospheres, 106, 5493-5505, http://dx.doi.org/10.1029/2000JD900572, 2001.

Levelt, P. F., van den Oord, G. H. J., Dobber, M. R., Malkki, A., Stammes, P., Lundell, J. O. V., and Saari, H.: The ozone monitoring instrument, IEEE T. Geosci. Remote Sens., 44, 1093–1101, http://dx.doi.org/10.1109/TGRS.2006.872333, 2006.

Li, D., Wang, X., Mo, J., Sheng, G., and Fu, J.: Soil nitric oxide emissions from two subtropical humid forests in south China, J. Geophys. Res.-Atmos., 112, D23302, http://dx.doi.org/10.1029/2007JD008680, 2007.

Li, J., Li, Y., Bo, Y., and Xie, S.: High-resolution historical emission inventories of crop residue burning in fields in China for the period 1990–2013, Atmos. Environ., 138, 152–161, http://dx.doi.org/10.1016/j.atmosenv.2016.05.002, 2016.

Li, L., Chen, C. H., Fu, J. S., Huang, C., Streets, D. G., Huang, H. Y., Zhang, G. F., Wang, Y. J., Jang, C. J., Wang, H. L., Chen, Y. R., and Fu, J. M.: Air quality and emissions in the Yangtze River Delta, China, Atmos. Chem. Phys., 11, 1621–1639, http://dx.doi.org/10.5194/acp-11-1621-2011, 2011.

Li, M., Zhang, Q., Kurokawa, J. I., Woo, J. H., He, K., Lu, Z., Ohara, T., Song, Y., Streets, D. G., Carmichael, G. R., Cheng, Y., Hong, C., Huo, H., Jiang, X., Kang, S., Liu, F., Su, H., and Zheng, B.: MIX: a mosaic Asian anthropogenic emission inventory under the international collaboration framework of the MICS-Asia and HTAP, Atmos. Chem. Phys., 17, 935-963, http://dx.doi.org/10.5194/acp-17-935-2017, 2017.

Lin, J.-T. and McElroy, M. B.: Detection from space of a reduction in anthropogenic emissions of nitrogen oxides during the Chinese economic downturn, Atmos. Chem. Phys., 11, 8171–8188, http://dx.doi.org/10.5194/acp-11-8171-2011, 2011.

Lin, J.-T., Liu, Z., Zhang, Q., Liu, H., Mao, J., and Zhuang, G.: Modeling uncertainties for tropospheric nitrogen dioxide columns affecting satellite-based inverse modeling of nitrogen oxides emissions, Atmos. Chem. Phys., 12, 12255–12275, http://dx.doi.org/10.5194/acp-12-12255-2012, 2012.

Lin, J.-T.: Satellite constraint for emissions of nitrogen oxides from anthropogenic, lightning and soil sources over East China on a high-resolution grid, Atmos. Chem. Phys., 12, 2881–2898, http://dx.doi.org/10.5194/acp-12-2881-2012, 2012.

Lin, J.-T., Martin, R. V., Boersma, K. F., Sneep, M., Stammes, P., Spurr, R., Wang, P., Van Roozendael, M., Clémer, K., and Irie, H.: Retrieving tropospheric nitrogen dioxide from the Ozone Monitoring Instrument: effects of aerosols, surface reflectance anisotropy, and vertical profile of nitrogen dioxide, Atmos. Chem. Phys., 14, 1441–1461, http://dx.doi.org/10.5194/acp-14-1441-2014, 2014.

Lin, W., Xu, X., Ge, B., and Liu, X.: Gaseous pollutants in Beijing urban area during the heating period 2007–2008: variability, sources, meteorological, and chemical impacts, Atmos. Chem. Phys., 11, 8157–8170, http://dx.doi.org/10.5194/acp-11-8157-2011, 2011.

Liu, H., Wang, X., Zhang, J., He, K., Wu, Y., and Xu, J.: Emission controls and changes in air quality in Guangzhou during the Asian Games, Atmos. Environ., 76, 81–93, http://dx.doi.org/10.1016/j.atmosenv.2012.08.004, 2013.

Liu, H., Fu, M., Jin, X., Shang, Y., Shindell, D., Faluvegi, G., Shindell, C., and He, K.: Health and climate impacts of ocean-going vessels in East Asia, Nature Climate Change, 6, 1037–1041, http://dx.doi.org/10.1038/nclimate3083, 2016.

Liu, F., Zhang, Q., Tong, D., Zheng, B., Li, M., Huo, H., and He, K. B.: High-resolution inventory of technologies, activities, and emissions of coal-fired power plants in China from 1990 to 2010, Atmos. Chem. Phys., 15, 13299-13317, http://dx.doi.org/10.5194/acp-15-13299-2015, 2015.

Liu, F., Zhang, Q., van der A, R. J., Zheng, B., Tong, D., Yan, L., Zheng, Y., and He, K.: Recent reduction in NO x emissions over China: synthesis of satellite observations and emission inventories, Environmental Research Letters, 11, 114002, https://doi.org/10.1088/1748-9326/11/11/114002, 2016.

Lorente, A., Folkert Boersma, K., Yu, H., Dörner, S., Hilboll, A., Richter, A., Liu, M., Lamsal, L. N., Barkley, M., De Smedt, I., Van Roozendael, M., Wang, Y., Wagner, T., Beirle, S., Lin, J.-T., Krotkov, N., Stammes, P., Wang, P., Eskes, H. J., and Krol, M.: Structural uncertainty in air mass factor calculation for NO_2 and HCHO satellite retrievals, Atmos. Meas. Tech., 10, 759–782, http://dx.doi.org/10.5194/amt-10-759-2017, 2017.

Ma, J., and van Aardenne, J. A.: Impact of different emission inventories on simulated tropospheric ozone over China: a regional chemical transport model evaluation, Atmos. Chem. Phys., 4, 877-887, http://dx.doi.org/10.5194/acp-4-877-2004, 2004.

Ma, J. Z., Beirle, S., Jin, J. L., Shaiganfar, R., Yan, P., and Wagner, T.: Tropospheric NO_2 vertical column densities over Beijing: results of the first three years of ground-based MAX-DOAS measurements (2008–2011) and satellite validation, Atmos. Chem. Phys., 13, 1547–1567, http://dx.doi.org/10.5194/acp-13-1547-2013, 2013.

Martin, R. V., Jacob, D. J., Chance, K., Kurosu, T. P., Palmer, P. I., and Evans, M. J.: Global inventory of nitrogen oxide emissions constrained by space-based observations of NO_2 columns, Journal of Geophysical Research: Atmospheres, 108, http://dx.doi.org/10.1029/2003JD003453, 2003.

Menut, L., Bessagnet, B., Khvorostyanov, D., Beekmann, M., Blond, N., Colette, A., Coll, I., Curci, G., Foret, G., Hodzic, A., Mailler, S., Meleux, F., Monge, J.-L., Pison, I., Siour, G., Turquety, S., Valari, M., Vautard, R., and Vivanco, M. G.: CHIMERE 2013: a model for regional atmosphericcomposition modelling, Geosci. Model Dev., 6, 981–1028, http://dx.doi.org/10.5194/gmd-6-981-2013, 2013.

Mijling, B., van der A, R. J., Boersma, K. F., Van Roozendael, M., De Smedt, I., and Kelder, H. M.: Reductions of NO_2 detected from space during the 2008 Beijing Olympic Games, Geophys. Res. Lett., 36, L13801, http://dx.doi.org/10.1029/2009GL038943, 2009.

Mijling, B., and van der A, R. J.: Using daily satellite observations to estimate emissions of short-lived air pollutants on a mesoscopic scale, Journal of Geophysical Research: Atmospheres, 117, http://dx.doi.org/10.1029/2012JD017817, 2012.

Mijling, B., van der A, R. J., and Zhang, Q.: Regional nitrogen oxides emission trends in East Asia observed from space, Atmos. Chem. Phys., 13, 12003–12012, http://dx.doi.org/10.5194/acp-13-12003-2013, 2013.

Miyazaki, K., Eskes, H. J., and Sudo, K.: Global NO_x emission estimates derived from an assimilation of OMI tropospheric NO_2 columns, Atmospheric Chemistry and Physics, 12, 2263-2288, http://dx.doi.org/10.5194/acp-12-2263-2012, 2012.

Miyazaki, K. and Eskes, H.: Constraints on surface NO_x emissions by assimilating satellite observations of multiple species, Geophys. Res. Lett., 40, 4745–4750, http://dx.doi.org/10.1002/grl.50894, 2013.

Miyazaki, K., Eskes, H. J., Sudo, K., and Zhang, C.: Global lightning NO_x production estimated by an assimilation of multiple satellite data sets, Atmos. Chem. Phys., 14, 3277-3305, http://dx.doi.org/10.5194/acp-14-3277-2014, 2014.

Miyazaki, K., Eskes, H., Sudo, K., Boersma, K. F., Bowman, K., and Kanaya, Y.: Decadal changes in global surface NO_x emissions from multi-constituent satellite data assimilation, Atmos. Chem. Phys., 17, 807-837, http://dx.doi.org/10.5194/acp-17-807-2017, 2017.

Müller, J. F., and Stavrakou, T.: Inversion of CO and NO_x emissions using the adjoint of the IMAGES model, Atmos. Chem. Phys., 5, 1157-1186, http://dx.doi.org/10.5194/acp-5-1157-2005, 2005.

Nanjing Statistical Bureau: Statistic Yearbook of Nanjing, China Statistics Press, Beijing, 2013 (in Chinese).

Napelenok, S. L., Pinder, R. W., Gilliland, A. B., and Martin, R. V.: A method for evaluating spatially-resolved NO_x emissions using Kalman filter inversion, direct sensitivities, and space-based NO_2 observations, Atmos. Chem. Phys., 8, 5603–5614, http://dx.doi.org/10.5194/acp-8-5603-2008, 2008.

Niemeier, D. A., Zheng, Y., and Kear, T.: UCDrive: a new gridded mobile source emission inventory model, Atmospheric Environment, 38, 305-319, http://dx.doi.org/10.1016/j.atmosenv.2003.09.040, 2004.

Ohara, T., Akimoto, H., Kurokawa, J., Horii, N., Yamaji, K., Yan, X., and Hayasaka, T.: An Asian emission inventory of anthropogenic emission sources for the period 1980 – 2020, Atmos. Chem. Phys., 7, 4419-4444, http://dx.doi.org/10.5194/acp-7-4419-2007, 2007.

Ramanathan, V., Cicerone, R. J., Singh, H. B., and Kiehl, J. T.: Trace gas trends and their potential role in climate change, Journal of Geophysical Research: Atmospheres, 90, 5547-5566, http://dx.doi.org/10.1029/JD090iD03p05547, 1985.

Ran, L., Zhao, C., Geng, F., Tie, X., Tang, X., Peng, L., Zhou, G., Yu, Q.,Xu, J., and Guenther, A.: Ozone photochemical production in urban Shanghai, China: Analysis based on ground level observations, J. Geophys. Res., 114, D15301, http://dx.doi.org/10.1029/2008JD010752, 2009

Ren, K. and Jin, Y.: Chinese offshore platforms take responsibility in Air Quality Control, http://zhaobiao.cnooc.com.cn/data/html/news/2014-01-09/english/350399.html, in Chinese, 2014 last access: 07 August 2017.

Richter, A., Eyring, V., Burrows, J. P., Bovensmann, H., Lauer, A., Sierk, B., and Crutzen, P. J.: Satellite measurements of NO_2 from international shipping emissions, Geophys. Res. Lett., 31, L23110, http://dx.doi.org/10.1029/2004GL020822, 2004.

Richter, A., Burrows, J. P., Nüss, H., Granier, C., and Niemeier, U.: Increase in tropospheric nitrogen dioxide over China observed from space, Nature, 437, 129–32, http://dx.doi.org/10.1038/nature04092, 2005

Russell, A. R., Perring, A. E., Valin, L. C., Bucsela, E. J., Browne, E. C., Wooldridge, P. J., and Cohen, R. C.: A high spatial resolution retrieval of NO_2 column densities from OMI: method and evaluation, Atmos. Chem. Phys., 11, 8543–8554, http://dx.doi.org/10.5194/acp-11-8543-2011, 2011.

Saikawa, E., Kim, H., Zhong, M., Avramov, A., Zhao, Y., Janssens-Maenhout, G., Kurokawa, J. I., Klimont, Z., Wagner, F., Naik, V., Horowitz, L. W., and Zhang, Q.: Comparison of emissions inventories of anthropogenic air pollutants and greenhouse gases in China, Atmos. Chem. Phys., 17, 6393-6421, http://dx.doi.org/10.5194/acp-17-6393-2017, 2017.

Schindlbacher, A., Zechmeister-Boltenstern, S., and Butterbach-Bahl, K.: Effects of soil moisture and temperature on NO, NO_2, and N_2O emissions from European forest soils, J. Geophys. Res., 109, D17302, http://dx.doi.org/10.1029/2004JD004590, 2004.

Schmidt, H.: A comparison of simulated and observed ozone mixing ratios for the summer of 1998 in Western Europe, Atmos. Environ., 35, 6277–6297, http://dx.doi.org/10.1016/S1352-2310(01)00451-4, 2001.

Schneider, P., and van der A, R. J.: A global single-sensor analysis of 2002–2011 tropospheric nitrogen dioxide trends observed from space, Journal of Geophysical Research: Atmospheres, 117, http://dx.doi.org/10.1029/2012JD017571, 2012.

Schultz, M. G., Heil, A., Hoelzemann, J. J., Spessa, A., Thonicke, K., Goldammer, J. G., Held, A. C., Pereira, J. M. C., and van het Bolscher, M.: Global wildland fire emissions from 1960 to 2000, Global Biogeochem. Cy., 22, GB2002, http://dx.doi.org/10.1029/2007GB003031, 2008.

Shao, M., Tang, X., Zhang, Y., and Li, W.: City clusters in China: air and surface water pollution, Frontiers in Ecology and the Environment, 4, 353-361, http://dx.doi.org/10.1890/1540-9295(2006)004[0353:CCICAA]2.0.CO;2, 2006.

Shen, G. and Heino, M.: An overview of marine fisheries management in China, Marine Policy, 44, 265-272, http://dx.doi.org/10.1016/j.marpol.2013.09.012, 2014.

Shindell, D. T., Faluvegi, G., Koch, D. M., Schmidt, G. A., Unger, N., and Bauer, S. E.: Improved Attribution of Climate Forcing to Emissions, Science, 326, 716-718, http://dx.doi.org/10.1016/10.1126/science.1174760, 2009.

Sitch, S., Cox, P. M., Collins, W. J., and Huntingford, C.: Indirect radiative forcing of climate change through ozone effects on the land-carbon sink, Nature, 448, 791-794, http://www.nature.com/nature/journal/v448/n7155/suppinfo/nature06059_S1.html, 2007.

Sofiev, M., Vankevich, R., Lotjonen, M., Prank, M., Petukhov, V., Ermakova, T., Koskinen, J., and Kukkonen, J.: An operational system for the assimilation of the satellite information on wild-land fires for the needs of air quality modelling and forecasting, Atmos. Chem. Phys., 9, 6833–6847, http://dx.doi.org/10.5194/acp-9-6833-2009, 2009.

Stammes, P., Sneep, M., de Haan, J. F., Veefkind, J. P., Wang, P., and Levelt, P. F.: Effective cloud fractions from the Ozone Monitoring Instrument: Theoretical framework and validation, J. Geophys. Res., 113, D16S38, http://dx.doi.org/10.1029/2007JD008820, 2008.

Stavrakou, T., Müller„ J. F., Boersma, K. F., De Smedt, I., and van der A, R. J.: Assessing the distribution and growth rates of NO_x emission sources by inverting a 10-year record of NO_2 satellite columns, Geophysical Research Letters, 35, http://dx.doi.org/10.1016/10.1029/2008GL033521, 2008.

Stavrakou, T., Müller, J.-F., Boersma, K. F., van der A, R. J., Kurokawa, J., Ohara, T., and Zhang, Q.: Key chemical NO_x sink uncertainties and how they influence top-down emissions of nitrogen oxides, Atmos. Chem. Phys., 13, 9057–9082, http://dx.doi.org/10.5194/acp-13-9057-2013, 2013.

Stavrakou, T., Müller, J. F., Bauwens, M., De Smedt, I., Lerot, C., Van Roozendael, M., Coheur, P. F., Clerbaux, C., Boersma, K. F., van der A, R., and Song, Y.: Substantial Underestimation of Post-Harvest Burning Emissions in the North China Plain Revealed by Multi-Species Space Observations, Scientific Reports, 6, 32307, http://dx.doi.org/10.1016/j.atmosres.2016.06.012, 2016.

Streets, D. G., Carmichael, G. R., and Arndt, R. L.: Sulfur dioxide emissions and sulfur deposition from international shipping in Asian waters, Atmospheric Environment, 31, 1573-1582, http://dx.doi.org/10.1016/S1352-2310(96)00204-X, 1997.

Streets, D. G., Bond, T. C., Carmichael, G. R., Fernandes, S. D., Fu, Q., He, D., Klimont, Z., Nelson, S. M., Tsai, N. Y., Wang, M. Q., Woo, J. H., and Yarber, K. F.: An inventory of gaseous and primary aerosol emissions in Asia in the year 2000, Journal of Geophysical Research: Atmospheres, 108, http://dx.doi.org/10.1029/2002JD003093, 2003.

Streets, D. G., Canty, T., Carmichael, G. R., de Foy, B., Dickerson, R. R., Duncan, B. N., Edwards, D. P., Haynes, J. A., Henze, D. K., Houyoux, M. R., Jacob, D. J., Krotkov, N. A., Lamsal, L. N., Liu, Y., Lu, Z., Martin, R. V., Pfister, G. G., Pinder, R. W., Salawitch, R. J., and Wecht, K. J.: Emissions estimation from satellite retrievals: A review of current capability, Atmospheric Environment, 77, 1011-1042, http://dx.doi.org/10.1016/j.atmosenv.2013.05.051, 2013.

Struzewska, J., Kaminski, J. W., and Jefimow, M.: Application of model output statistics to the GEM-AQ high resolution air quality forecast, Atmos. Res., 181, 186–199, http://dx.doi.org/10.1016/j.atmosres.2016.06.012, 2016.

Sudo, K., Takahashi, M., Kurokawa, J.-i., and Akimoto, H.: CHASER: A global chemical model of the troposphere, 1. Model description, J. Geophys. Res., 107, 4339, http://dx.doi.org/10.1029/2001JD001113, 2002.

Tang, W., Cohan, D. S., Lamsal, L. N., Xiao, X., and Zhou, W.: Inverse modeling of Texas NO_x emissions using space-based and ground-based NO_2 observations, Atmos. Chem. Phys., 13, 11005–11018, http://dx.doi.org/10.5194/acp-13-11005-2013, 2013.

Tie, X., Li, G., Ying, Z., Guenther, A., and Madronich, S.: Biogenic emissions of isoprenoids and NO in China and comparison to anthropogenic emissions, Sci. Total Environ., 371, 238–251, http://dx.doi.org/10.1016/j.scitotenv.2006.06.025, 2006.

Thornton, J. A., Virts, K. S.,Holzworth, R. H., and Mitchell, T. P.: Lightning enhancement over major oceanic shipping lanes, Geophysical Research Letters, 44(17), 9102-9111, doi:10.1002/2017GL074982, 2017.

Tu, J., Xia, Z.-G., Wang, H., and Li, W.: Temporal variations in surface ozone and its precursors and meteorological effects at an urban site in China, Atmos. Res., 85, 310–337, http://dx.doi.org/10.1016/j.atmosres.2007.02.003, 2007.

Valin, L. C., Russell, A. R., Hudman, R. C., and Cohen, R. C.: Effects of model resolution on the interpretation of satellite NO¬2 observations, Atmos. Chem. Phys., 11, 11647-11655, http://dx.doi.org/10.5194/acp-11-11647-2011, 2011.

Van Aardenne, J. A., Carmichael, G. R., Levy, H., Streets, D., and Hordijk, L.: Anthropogenic NO_x emissions in Asia in the period 1990‐2020, Atmospheric Environment, 33, 633-646, http://dx.doi.org/10.1016/S1352-2310(98)00110-1, 1999.

Van der A, R. J., Peters, D. H. M. U., Eskes, H., Boersma, K. F., Van Roozendael, M., De Smedt, I., and Kelder, H. M.: Detection of the trend and seasonal variation in tropospheric NO_2 over China, Journal of Geophysical Research: Atmospheres, 111, D12317, http://dx.doi.org/10.1029/2005JD006594, 2006.

Van der A, R. J., Mijling, B., Ding, J., Koukouli, M. E., Liu, F., Li, Q., Mao, H., and Theys, N.: Cleaning up the air: effectiveness of air quality policy for SO_2 and NO_x emissions in China, Atmos. Chem. Phys., 17, 1775-1789, http://dx.doi.org/10.5194/acp-17-1775-2017, 2017.

van der Werf, G. R., Randerson, J. T., Giglio, L., Collatz, G. J., Mu, M., Kasibhatla, P. S., Morton, D. C., DeFries, R. S., Jin, Y., and van Leeuwen, T. T.: Global fire emissions and the contribution of deforestation, savanna, forest, agricultural, and peat fires (1997–2009), Atmos. Chem. Phys., 10, 11707–11735, http://dx.doi.org/10.5194/acp-10-11707-2010, 2010.

Veefkind, J. P., Aben, I., McMullan, K., Förster, H., de Vries, J., Otter, G., Claas, J., Eskes, H. J., de Haan, J. F., Kleipool, Q., van Weele, M., Hasekamp, O., Hoogeveen, R., Landgraf, J., Snel, R., Tol, P., Ingmann, P., Voors, R., Kruizinga, B., Vink, R., Visser, H., and Levelt, P. F.: TROPOMI on the ESA Sentinel-5 Precursor: A GMES mission for global observations of the atmospheric composition for climate, air quality and ozone layer applications, Remote Sensing of Environment, 120, 70-83, http://dx.doi.org/10.1016/j.rse.2011.09.027, 2012.

Vinken, G. C. M., Boersma, K. F., Maasakkers, J. D., Adon, M., and Martin, R. V.: Worldwide biogenic soil NO_x emissions inferred from OMI NO_2 observations, Atmos. Chem. Phys., 14, 10363-10381, http://dx.doi.org/10.5194/acp-14-10363-2014, 2014a.

Vinken, G. C. M., Boersma, K. F., van Donkelaar, A., and Zhang, L.: Constraints on ship NO_x emissions in Europe using GEOS-Chem and OMI satellite NO_2 observations, Atmos. Chem. Phys., 14, 1353-1369, http://dx.doi.org/10.5194/10.5194/acp-14-1353-2014, 2014b.

Wang, C., Corbett, J. J., and Firestone, J.: Improving Spatial Representation of Global Ship Emissions Inventories, Environmental Science & Technology, 42, 193-199, http://dx.doi.org/10.1021/es0700799, 2008.

Wang, J., Li, M., Liu, Y., Zhang, H., Zou, W., and Cheng, L.: Safety assessment of shipping routes in the South China Sea based on the fuzzy analytic hierarchy process, Safety Science, 62, 46-57, http://dx.doi.org/10.1016/j.ssci.2013.08.002, 2014.

Wang, L., Qi, J. H., Shi, J. H., Chen, X. J., and Gao, H. W.: Source apportionment of particulate pollutants in the atmosphere over the Northern Yellow Sea, Atmospheric Environment, 70, 425-434, https://doi.org/10.1016/j.atmosenv.2012.12.041, 2013.

Wang, S., Zhao, M., Xing, J., Wu, Y., Zhou, Y., Lei, Y., He, K., Fu, L., and Hao, J.: Quantifying the air pollutants emission reduction during the 2008 olympic games in Beijing, Environ. Sci. Technol., 44, 2490–2496, http://dx.doi.org/10.1021/es9028167, 2010.

Wang, S., Xing, J., Chatani, S., Hao, J., Klimont, Z., Cofala, J., and Amann, M.: Verification of anthropogenic emissions of China by satellite and ground observations, Atmos. Environ., 45, 6347–6358, http://dx.doi.org/10.1016/j.atmosenv.2011.08.054, 2011.

Wang, S. W., Zhang, Q., Streets, D. G., He, K. B., Martin, R. V., Lamsal, L. N., Chen, D., Lei, Y., and Lu, Z.: Growth in NO_x emissions from power plants in China: bottom-up estimates and satellite observations, Atmos. Chem. Phys., 12, 4429–4447, http://dx.doi.org/10.5194/acp-12-4429-2012, 2012.

Wang, Y. X., McElroy, M. B., Wang, T., and Palmer, P. I.: Asian emissions of CO and NO_x: Constraints from aircraft and Chinese station data, J. Geophys. Res., 109, D24304, http://dx.doi.org/10.1029/2004JD005250, 2004.

Wang, Y., McElroy, M. B., Martin, R. V., Streets, D. G., Zhang, Q., and Fu, T. M.: Seasonal variability of NO_x emissions over east China constrained by satellite observations: Implications for combustion and microbial sources, J. Geophys. Res.-Atmos., 112, 1–19, http://dx.doi.org/10.1029/2006JD007538, 2007.

Wang, Y., Beirle, S., Lampel, J., Koukouli, M., De Smedt, I., Theys, N., Li, A., Wu, D., Xie, P., Liu, C., Van Roozendael, M., Stavrakou, T., Müller, J.-F., and Wagner, T.: Validation of OMI, GOME-2A and GOME-2B tropospheric NO_2, SO_2 and HCHO products using MAX-DOAS observations from 2011 to 2014 in Wuxi, China: investigation of the effects of priori profiles and aerosols on the satellite products, Atmos. Chem. Phys., 17, 5007–5033, http://dx.doi.org/10.5194/acp-17-5007-2017, 2017.

Watanabe, S., Hajima, T., Sudo, K., Nagashima, T., Takemura, T., Okajima, H., Nozawa, T., Kawase, H., Abe, M., Yokohata, T., Ise, T., Sato, H., Kato, E., Takata, K., Emori, S., and Kawamiya, M.: MIROC-ESM 2010: model description and basic results of CMIP5-20c3m experiments, Geosci. Model Dev., 4, 845–872, http://dx.doi.org/10.5194/gmd-4-845-2011, 2011.

Witte, J. C., Schoeberl, M. R., Douglass, A. R., Gleason, J. F., Krotkov, N. A., Gille, J. C., Pickering, K. E., and Livesey, N.: Satellite observations of changes in air quality during the 2008 Beijing Olympics and Paralympics, Geophys. Res. Lett., 36, L17803, http://dx.doi.org/10.1029/2009GL039236, 2009.

Wu, F. C., Xie, P. H., Li, A., Chan, K. L., Hartl, A., Wang, Y., Si, F. Q., Zeng, Y., Qin, M., Xu, J., Liu, J. G., Liu, W. Q., and Wenig, M.: Observations of $SO_2$2 by mobile DOAS in the Guangzhou eastern area during the Asian Games 2010, Atmos. Meas. Tech., 6, 2277–2292, http://dx.doi.org/10.5194/amt-6-2277-2013, 2013.

Xing, Q., Meng, R., Lou, M., Bing, L., and Liu, X.: Remote Sensing of Ships and Offshore Oil Platforms and Mapping the Marine Oil Spill Risk Source in the Bohai Sea, Aquatic Procedia, 3, 127-132,http://dx.doi.org/10.1016/j.aqpro.2015.02.236, 2015.

Yienger, J. J. and Levy, H.: Empirical model of global soil-biogenic NO_x emissions, J. Geophys. Res., 100, 11447–11464, http://dx.doi.org/10.1029/95JD00370, 1995.

Zhang, F., Chen, Y., Tian, C., Wang, X., Huang, G., Fang, Y., and Zong, Z.: Identification and quantification of shipping emissions in Bohai Rim, China, Science of The Total Environment, 497–498, 570-577, https://doi.org/10.1016/j.scitotenv.2014.08.016, 2014.

Zhang, H., Sun, Z., Zhen, Y., Zhang, X., and Yu, B.: Impact of Temperature Change on Urban Electric Power Load in Nanjing, Transations Atmos. Sci., 32, 536–542, 2009. (in Chinese)

Zhang, L., Liu, Y., and Hao, L.: Contributions of open crop straw burning emissions to $PM_{2.5}$ concentrations in China, Environ. Res. Lett., 11, 014014, http://dx.doi.org/10.1088/1748-9326/11/1/014014, 2016.

Zhang, Q., Streets, D. G., He, K., Wang, Y., Richter, A., Burrows, J. P., Uno, I., Jang, C. J., Chen, D., Yao, Z., and Lei, Y.: NO_x emission trends for China, 1995–2004: The view from the ground and the view from space, J. Geophys. Res., 112, D22306, http://dx.doi.org/10.1029/2007JD008684, 2007.

Zhang, Q., Streets, D. G., Carmichael, G. R., He, K. B., Huo, H., Kannari, A., Klimont, Z., Park, I. S., Reddy, S., Fu, J. S., Chen, D., Duan, L., Lei, Y., Wang, L. T., and Yao, Z. L.: Asian emissions in 2006 for the NASA INTEX-B mission, Atmos. Chem. Phys., 9, 5131-5153, http://dx.doi.org/10.5194/acp-9-5131-2009, 2009.

Zhang, Y., Yang, X., Brown, R., Yang, L., Morawska, L., Ristovski, Z., Fu, Q., and Huang, C.: Shipping emissions and their impacts on air quality in China, Science of The Total Environment, 581–582, 186-198, http://dx.doi.org/10.1016/j.scitotenv.2016.12.098, 2017.

Zhang, Y., Bocquet, M., Mallet, V., Seigneur, C., and Baklanov, A.: Real-time air quality forecasting, part II: State of the science, current research needs, and future prospects, Atmos. Environ., 60, 656–676, http://dx.doi.org/10.1016/j.atmosenv.2012.02.041, 2012.

Zhao, C., and Wang, Y.: Assimilated inversion of NO_x emissions over east Asia using OMI NO_2 column measurements, Geophysical Research Letters, 36, http://dx.doi.org/10.1029/2008GL037123, 2009.

Zhao, Y., Wang, S., Duan, L., Lei, Y., Cao, P., and Hao, J.: Primary air pollutant emissions of coal-fired power plants in China: Current status and future prediction, Atmospheric Environment, 42, 8442-8452, http://dx.doi.org/10.1016/j.atmosenv.2008.08.021, 2008.

Zhao, Y., Nielsen, C. P., Lei, Y., McElroy, M. B., and Hao, J.: Quantifying the uncertainties of a bottom-up emission inventory of anthropogenic atmospheric pollutants in China, Atmos. Chem. Phys., 11, 2295-2308, http://dx.doi.org/10.5194/acp-11-2295-2011, 2011.

Zheng, B., Huo, H., Zhang, Q., Yao, Z. L., Wang, X. T., Yang, X. F., Liu, H., and He, K. B.: High-resolution mapping of vehicle emissions in China in 2008, Atmos. Chem. Phys., 14, 9787-9805, http://dx.doi.org/10.5194/acp-14-9787-2014, 2014.

Zoogman, P., Liu, X., Suleiman, R. M., Pennington, W. F., Flittner, D. E., Al-Saadi, J. A., Hilton, B. B., Nicks, D. K., Newchurch, M. J., Carr, J. L., Janz, S. J., Andraschko, M. R., Arola, A., Baker, B. D., Canova, B. P., Chan Miller, C., Cohen, R. C., Davis, J. E., Dussault, M. E., Edwards, D. P., Fishman, J., Ghulam, A., González Abad, G., Grutter, M., Herman, J. R., Houck, J., Jacob, D. J., Joiner, J., Kerridge, B. J., Kim, J., Krotkov, N. A., Lamsal, L., Li, C., Lindfors, A., Martin, R. V., McElroy, C. T., McLinden, C., Natraj, V., Neil, D. O., Nowlan, C. R., O'Sullivan, E. J., Palmer, P. I., Pierce, R. B., Pippin, M. R., Saiz-Lopez, A., Spurr, R. J. D., Szykman, J. J., Torres, O., Veefkind, J. P., Veihelmann, B., Wang, H., Wang, J., and Chance, K.: Tropospheric emissions: Monitoring of pollution (TEMPO), Journal of Quantitative Spectroscopy and Radiative Transfer, 186, 17-39, urlhttp://dx.doi.org/10.1016/j.jqsrt.2016.05.008, 2017.

Zörner, J., Penning de Vries, M., Beirle, S., Sihler, H., Veres, P. R., Williams, J., and Wagner, T.: Multi-satellite sensor study on precipitation-induced emission pulses of NO_x from soils in semi-arid ecosystems, Atmos. Chem. Phys., 16, 9457–9487, http://dx.doi.org/10.5194/acp-16-9457-2016, 2016.

Acknowledgements

Firstly, I would like to express my sincere appreciation to my daily supervisor Ronald van der A for the continuous support of my Ph.D. study, for his patience, motivation, and knowledge. His guidance helped me in research and writing articles. He let me participate in projects associated with my home country China and gave me many opportunities to travel and present my work there. Apart from work, he also helped me a lot in my life. As a foreigner living in the Netherlands, I had many problems in living in this country, such as finding an apartment, moving and other problems in life. He was always willing to help. I could not have imagined having a better supervisor for my Ph.D. study.

Besides my supervisor, I would like to thank my promotor Pieternel Levelt for her support and encouragement during my Ph.D. study. She encouraged me to be confident in my research. Not like other Ph.D. students in the university, I stayed at KNMI and had to follow the Ph.D. program of TUD. Even though she was very busy, when I needed to check some information and rules of TUD, she always gave me help.

I would like to acknowledge all the evaluation committee members: Prof. Ramon Hanssen, Prof. Greet Janssens-Maenhout, Prof. Gerrit de Leeuw, Dr. Jenny Stavrakou and Prof. Herman Russchenberg. It is a great honour to have all of you as my thesis examiners.

I would like to thank Bas Mijling. Since my research is a follow-up study of his Ph.D. work, I had many questions about models and satellite observations, especially at the beginning of my Ph.D. study. He was always very patient to answer all my questions and helped me with the research.

Special thanks to Henk Eskes, because of him, I had my internship at KNMI. His encouragement and great supervision made me willing to go further on the way of science and apply for the Ph.D. position here.

I would like to express my gratitude to my co-authors: Miyazaki Kazuyuki, Junichi Kurokawa, Qiang Zhang, Fei Liu, Nan Hao, Greet Janssens-Maenhout, Jukka-Pekka Jalkanen and Lasse Johansson. I could not have my papers published without their great contributions.

I would also like to thank all my friends and colleagues at KNMI, TUD and Wageningen University. To Lidwien de Jong and Debbie Rietdijk, secretaries at TUD, thank you for helping me all kind of issues in Delft. Many thanks to Jacqueline Baas, management assistant at KNMI, even though I was not an official employee

of KNMI, she always regarded me as a member of the department and helped me or gave me advice when I had problems. To my KNMI colleagues: Piet Stammes, Folkert Boersma, Jos de Laat, Jos van Geffen, Ping Wang, Jacob van Peet, Pepijn Veefkind, Ankie Piters, Maarten Sneep; and to my Delft colleagues: Julien Chimot and Tim Vlemmix, thank you for providing support either in work or in life. To my supervisors of my master study at Wageningen: Wouter Peters, Jordi Vila and Maarten Krol, thank you for leading me to atmospheric research. I also would like to thank my previous office-mate Bram Sander and my current one Nikos Benas for sharing stories and having nice conversations every working day. Thanks to all my friends, talking and hanging out with them helped me release much stress from both work and life.

在此，我还要感谢颜旻昊，感谢你在我博士最后一年，作为我坚强的后盾，在我写论文最焦虑的时候，安慰我，照顾我。感谢好朋友王璐，相识 6 年，一起国外求学，一路相互鼓励，相互帮助。

最后，我要特别感谢我的爸爸妈妈，是你们的支持和帮助，让我出国留学，开阔眼界，我也因此了解领略了其他国家的文化，感受到了国与国之间的不同。感谢你们一直以来对我的理解，包容和鼓励，让我在异国他乡，无论遇到什么困难，都可以微笑的面对。

Curriculum Vitæ

Jieying DING

19-05-1989 Born in Nanjing, China.

Education

2007 – 2011 Graduates in Atmospheric Sciences,
Nanjing University of Information Sciences & Technology, China

2011 – 2013 Undergraduate in Earth & Environment
Major in Meteorology & Air Quality
Wageningen University, the Netherlands

2013 PhD. Atmospheric Remote Sensing, Faculty of Civil Engineering & Geosciences
Delft University of Technology
Thesis: Satellite-derived NO_x emissions over East Asia
Promotor: Prof. dr. P. F. Levelt
Co-promotor: Prof. dr. R. J. van der A

Training

27–31 Oct. 2014 2nd ESA Advanced Atmospheric Training Course
Forschungszentrum Jülich, Germany

23-29 Aug. 2015 *Remote sensing of the Atmosphere, Emissions and Modeling*
PANDA European Summer School, University of Bermen, Germany

Conference & Workshop

2014.05	Poster in the ESA-MOST cooperation Dragon 3 Mid-Term Symposium, Chengdu, China
2015.05	Poster in the EGU (European Geosciences Union) Conference, Vienna, Austria
2015.11	Poster in the 17th GEIA (Global Emissions InitiAtive) Conference, Beijing, China
2017.06	Poster in the ESA-MOST cooperation Dragon 4 Symposium, Copenhagen, Denmark
2015.01	Oral presentation in the Panda-MarcoPolo project meeting, Hamburg, Germany
2015.05	Oral presentation in the GlobEmission project meeting, Brussels, Belgium
2015.06	Poster in the ESA-MOST cooperation Dragon 3 Symposium, Interlaken, Switzerland
2015.09	Oral presentation in the OMI Science Team Meeting, De Bilt, the Netherlands
2015,11	Oral presentation in the GlobEmission User workshop, Doha, Qatar
2016.02	Oral presentation in the Panda-MarcoPolo annual project meeting, Guangzhou, China
2016.05	Oral presentation in the Living Planet Symposium, Prague, Czech Republic
2016.09	Oral presentation in the Aura Science Team Meeting, Rotterdam, the Netherlands
2016.12	Oral presentation in the AGU (American Geosciences Union) conference, San Francisco, USA
2017.02	Oral presentation in the Urban Air Quality Symposium, Delft, the Netherlands
2017.02	Oral presentation in the MarcoPolo final project and user workshop, Beijing, China
2017.09	Oral Presentation in 18th GEIA conference, Hamburg, Germany

Award

- Best Poster award in Atmosphere & Climate session at Dragon 3 Symposium (2015)

- Best Poster award in Atmosphere & Climate session at Dragon 3 Mid-Term Results International Symposium (2014)
- Award of Excellence in Mathematics Competition of Nanjing University of Information Science & Technology (2008)
- Merit Student (2008-2011) in Nanjing University of Information Science & Technology
- Outstanding class cadre (2008-2011) in Nanjing University of Information Science & Technology
- Outstanding Graduates Awards (2011) in Nanjing University of Information Science & Technology

List of Publications

1. **Ding, J.**, van der A, R. J., Mijling, B., Levelt, P. F., and Hao, N.: *NO_x emission estimates during the 2014 Youth Olympic Games in Nanjing*, Atmos. Chem. Phys., 15, 9399-9412, https://doi.org/10.5194/acp-15-9399-2015, 2015

2. **Ding, J.**, van der A, R. J., Mijling, B., and Levelt, P. F.: *Space-based NO_x emission estimates over remote regions improved in DECSO*, Atmos. Meas. Tech., 10, https://doi.org/10.5194/amt-10-925-2017 925-938, 2017a

3. **Ding, J.**,Miyazaki, K., van der A, R. J., Mijling, B., Kurokawa, J.-I., Cho, S., Janssens-Maenhout, G., Zhang, Q., Liu, F., and Levelt, P. F.:*Intercomparison of NOx emission inventories over East Asia*, Atmos. Chem. Phys., 17, 10125-10141, https://doi.org/10.5194/acp-17-10125-2017, 2017b

4. Van der A, R. J., Mijling, B., **Ding, J.**, Koukouli, M. E., Liu, F., Li, Q., Mao, H., and Theys, N.: *Cleaning up the air: effectiveness of air quality policy for SO_2 and NO_x emissions in China*, Atmos. Chem. Phys., 17, 1775-1789, https://doi.org/10.5194/acp-17-1775-2017, 2017

5. Kourtidis, K., Georgoulias, A. K., Mijling, B., van der A, R., Zhang, Q., and **Ding, J.**: *A new method for deriving trace gas emission inventories from satellite observations: The case of SO_2 over China*, Science of The Total Environment, 612, 923-930, http://dx.doi.org/dx.doi.org/10.1016/j.scitotenv.2017.08.313, 2018.

6. Koukouli M.E., Theys N., Ding J., Zyrichidou I., Balis D., van der A R. Top-Down SO2 Emissions Over China; A Satellite Approach. In: Karacostas T., Bais A., Nastos P. (eds) Perspectives on Atmospheric Sciences. Springer Atmospheric Sciences. Springer, Cham, https://doi.org/10.1007/978-3-319-35095-0_145, 2017

7. **Ding, J.**, van der A, R. J., Mijling, B., Jalkanen, J.-P., Johansson, L., and Levelt, P. F.: *Maritime NO_x emissions over Chinese seas derived from satellite observations*, Geophysical Research Letters, under review, 2018.

8. Liu, F., van der A, R. J., Eskes, H., **Ding, J.**, and Mijling, B.: *Evaluation of modelling NO_2 concentrations driven by satellite-derived and bottom-up emission inventories using in-situ measurements over China*, Atmos. Chem. Phys. Discuss., https://doi.org/10.5194/acp-2017-475, in review, 2017

9. Koukouli, M.-E., Theys, N., **Ding, J.**, Zyrichidou, I., Mijling, B., Balis, D., and van der A, R. J.: *Updated SO_2 emission estimates over China using OMI/Aura observations*, Atmos. Meas. Tech. Discuss., https://doi.org/10.5194/amt-2017-256, in review, 2017.

10. Van der A, R., **Ding, J.**, Mijling, B., Bai, J.: *Monitoring and Assessment of Regional Air Quality in China Using Space Observations (MarcoPolo)*,Dragon 3Mid Term Results, Proceedings of the conference held 26-29 May, 2015 at Chengdu, China. Edited by L. Ouwehand. ESA SP Vol. 724. ISBN: 978-92-9092-288-9, id.32

11. Koukouli, M. E., Balis, D. S., Zyrichidou, I., van der A, R., **Ding, J.**, Hedelt, P., Valks, P., Fioletov, V.: *Area Sulphur Dioxide Emissions over China Extracted from GOME2/MetopA Observations*, Living Planet Symposium, Proceedings of the conference held 9-13 May 2016 in Prague, Czech Republic. Edited by L. Ouwehand. ESA-SP Volume 740, ISBN: 978-92-9221-305-3, p.359